学位論文

Radiation Microscopy of Chemical Vapor Deposition Growth of Graphene

(放射顕微鏡を用いたグラフェン化学気相成長の研究)

平成 26 年 12 月 博士 (理学) 申請

東京大学大学院理学系研究科
化学専攻
寺澤 知潮

Abstract

Graphene, a monolayer sp^2 C sheet with a honeycomb structure, has attracted much attention of researchers to utilize its superior properties from the fundamental physics to industrial applications. Chemical vapor deposition (CVD) growth on Cu is considered the most feasible way to produce a large area and high quality monolayer graphene. Many growth parameters of CVD were optimized on the basis of the characterization mostly after the synthesis while the intermediate processes were imagined. Real-time observation enables us to understand the growth mechanism and control the growth more easily. However, the CVD growth of graphene on Cu requires high temperature and pressure, in which a conventional electron microscope cannot work.

Here, I report the development of the optical microscopy for the CVD growth of graphene on Cu in real-time, which is one of the key topics of the present study. The real-time optical microscopy observing the radiation light from high temperature materials, which I call "Radiation Microscopy", can distinguish the graphene grains from the Cu substrate reflecting the difference in their emissivities. Planck's law and the gray body model explain the principle of the observation and suggest the applicability of the present method to other film-substrate combinations.

Another topic is the analysis of the growth and shrinkage of graphene during CVD. The nucleation, growth, and shrinkage of graphene are observed to respond the change of the growth condition in real-time. The analysis of the growth features indicates that the rate-limiting steps of the growth and shrinkage are the attachment and detachment of the growth precursors at the graphene edges on the Cu substrates. The competition of the production and consumption of the growth precursors is found to determine whether the graphene growth or shrinkage occurs and their rates. Finally, I suggest a possible way to optimize the complicated parameters in the CVD growth of graphene on the Cu substrates.

Contents

Part I
Introduction

1 Background

Graphene, a monolayer sp^2 C sheet with a honeycomb structure, has attracted much attention of researchers since its first isolation reported by K. S. Novoselov *et al.* in 2004[1]. The superior properties of graphene are now investigated from the basic science to the industrial application. The discovery of graphene opened a new field of science in which atomically thin structures other than graphene also have been studied very recently[2–4]. A number of laboratories and companies are devoted to supply graphene devices in many methods. Particularly, the hottest topic is the improvement of the quality of graphene in a cost-effective way. In this part, I explain the history of the research about graphene and the current problem in the production of high quality graphene.

1.1 Structure and Property of Graphene

The extraordinary properties of graphene is directly related to its structure. Graphene is defined as a one-atom-thick sheet in which sp^2 C atoms construct a honeycomb lattice as shown in Fig. I. 1. 1. The primitive cell of a honeycomb structure consists of a couple of equivalent atoms. As a result, the reciprocal lattice possesses equivalent *K* and *K'* points at which the valence and conduction bands touch each other as shown in Fig. I. 1. 2. This is not a characteristic only of graphene but also of the hexagonal honeycomb structure[6]. The honeycomb lattice composed of two types of atoms such as MoS_2, on the other hand, has non-equivalent *K* and *K'* points and loses the spatial reverse symmetry, giving rise to the new electronics so-called "Valleytronics"[7, 8]. In hexagonal honeycomb structures, the motion of electrons are described by Dirac Hamiltonian[5, 9]. Since the electrons behave as a mass-less Dirac-fermion, graphene exhibits extraordinary properties: ultra high carrier mobility (more than 500,000 cm^2/Vs at low temperatures and 100,000 cm^2/Vs at room temperatures[8, 10–13]), high thermal conductivity[14], high transparency[15, 16], half-integer quantum Hall

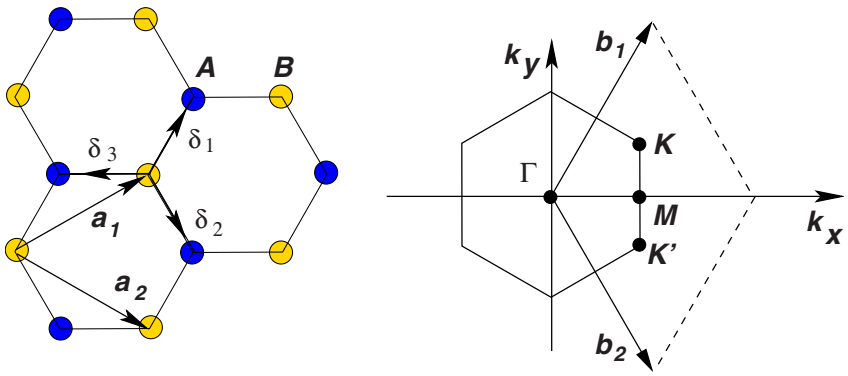

Figure I. 1. 1 Schematic illustrations of (left) lattice and (right) reciprocal lattice of graphene[5]. A primitive cell contains A and B atoms which can be non-equivalent. The Brillouin zone in the reciprocal lattice also contains *K* and *K'* points. Reprinted figure with permission from Castro Neto, A. H., Guinea, F., Peres, N. M. R., Novoselov, K. S. & Geim, A. K., Reviews of Modern Physics **81**, 109-162 (2009). Copyright 2009 by the American Physical Society. DOI: http://dx.doi.org/10.1103/RevModPhys.81.109

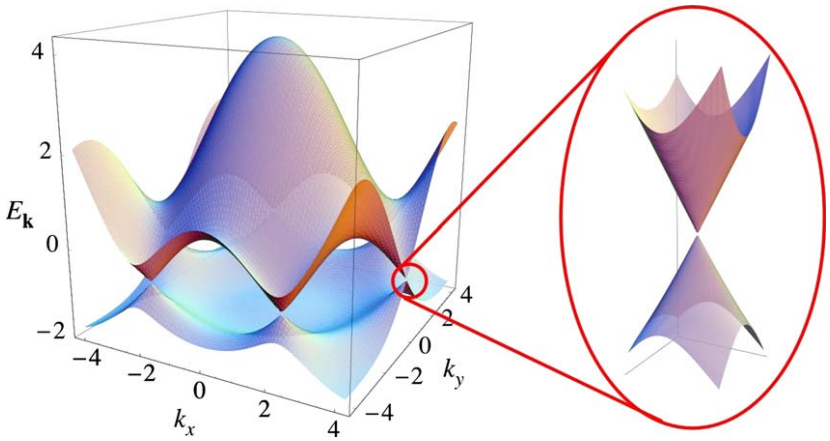

Figure I. 1. 2 Schematic illustration of band structure of graphene[5]. The conduction and valence bands with linear dispersion (so-called “Dirac cone”) touch each other at the *K* and *K'* points in the reciprocal lattice. Reprinted figure with permission from Castro Neto, A. H., Guinea, F., Peres, N. M. R., Novoselov, K. S. & Geim, A. K., Reviews of Modern Physics **81**, 109-162 (2009). Copyright 2009 by the American Physical Society. DOI: http://dx.doi.org/10.1103/RevModPhys.81.109

effect[17–19], and so on. The lattice of graphene consists of strong sp^2 bonds resulting in the mechanical strength with flexibility[20] while keeping a wide surface area due to the atomically thin structure.

In spite of the excellent properties, graphene does not possess a band gap between the conduction and valence bands as shown in Fig. I. 1. 2. This gap-less feature of graphene is one of the problems for the application of graphene. Graphene nano-ribbon (GNR), which is a graphene sheet with the width of nanometers, shows the finite band gap[21–26]. The properties of GNR are also studied to broaden the applicability of graphene as the future materials.

1.2 Fabrication of Graphene Devices

The fabrication of devices is indispensable to utilize the properties of graphene. The ultra high carrier mobility is considered useful for the field effect transistor (FET), for example[8, 11–13, 27]. The large surface area is suitable for the energy storage [28, 29] or sensors[30, 31] while the photo-electronic property is applicable[32]. The competition of quality and productivity is always the problem among the methods to fabricate graphene and graphene devices.

1.2.1 Quality

Most of the properties of graphene are sensitive to the quality of that: the number of graphene layers, defects, grain boundaries, impurities, and ripples. For example, unlike the mass-less Dirac fermion in monolayer graphene, electrons in bilayer graphene behave as *massive* Dirac fermion and lose a part of the superior properties of graphene[5, 9, 33, 34]. The description “bilayer graphene” is seemingly controversy to the definition of graphene. However, I use such terms to clarify the number of stacked graphene layers of monolayer, bilayer, and multilayer graphene. As graphene layers stack more than 10 layers, the properties of “multilayer graphene” are recognized almost the same as those of graphite, bulk graphene, which have been investigated before 1950s[35]. Therefore, it is extensively studied to obtain monolayer graphene selectively.

Even monolayer graphene is successfully obtained by the various methods, the remaining

defects and grain boundaries in graphene lattice are still problematic. Generally, numbers of defects in graphene lattice are evaluated by Raman spectroscopy (the intensity ratios of peaks are sensitive to the number of graphene layers and defects as discussed in section II. 2.2.2[36–38]). Carrier mobilities in the transport measurement are the important indicator for the application for electronics[8, 11–13, 27] while the presence of half-integer quantum Hall effect is used for the basic physics[8, 17, 18]. The improvement of the quality of graphene is thus achieved by the brushing up of the fabrication techniques.

1.2.2 Productivity

The productivity of graphene is important especially for the industrial applications. For example, the method which requires the specialists is not feasible for that purpose. High temperature and vacuum can also increase the cost of the production. Mass and fast productivity is also required.

In addition to the cost of the graphene production itself, the device fabrication requires the additional process and costs. Graphene should be patterned to fabricate the desired devices on the insulating substrate, which requires the established method to control the etching of graphene. Moreover, the fabrication of GNR devices also requires the etching method of graphene such as photo-lithography[39–41]. In addition to that, the etching of graphene in H_2 gas has been studied recently[42, 43]. For the etching of graphene in H_2 atmosphere, the chemical reaction of

$$2H_2 + C \longrightarrow CH_4 \tag{I. 1. 1}$$

seems to be the reasonable mechanism as the reversed reaction of graphene growth from CH_4 on the Cu substrates as discussed later. However, the dissociative adsorption of H_2 is negligible on the Cu substrates[44]. Furthermore, H_2 does not contribute to etch graphene after the sufficient purification[45]. The sufficient understanding of the mechanism in the etching of graphene can improve the method in that.

1.3 Fabrication Methods of Graphene

Here, I introduce the methods to obtain high-quality graphene based on the Fig. I. 1. 3 which shows the quality and productivity of the methods: mechanical exfoliation, chemical

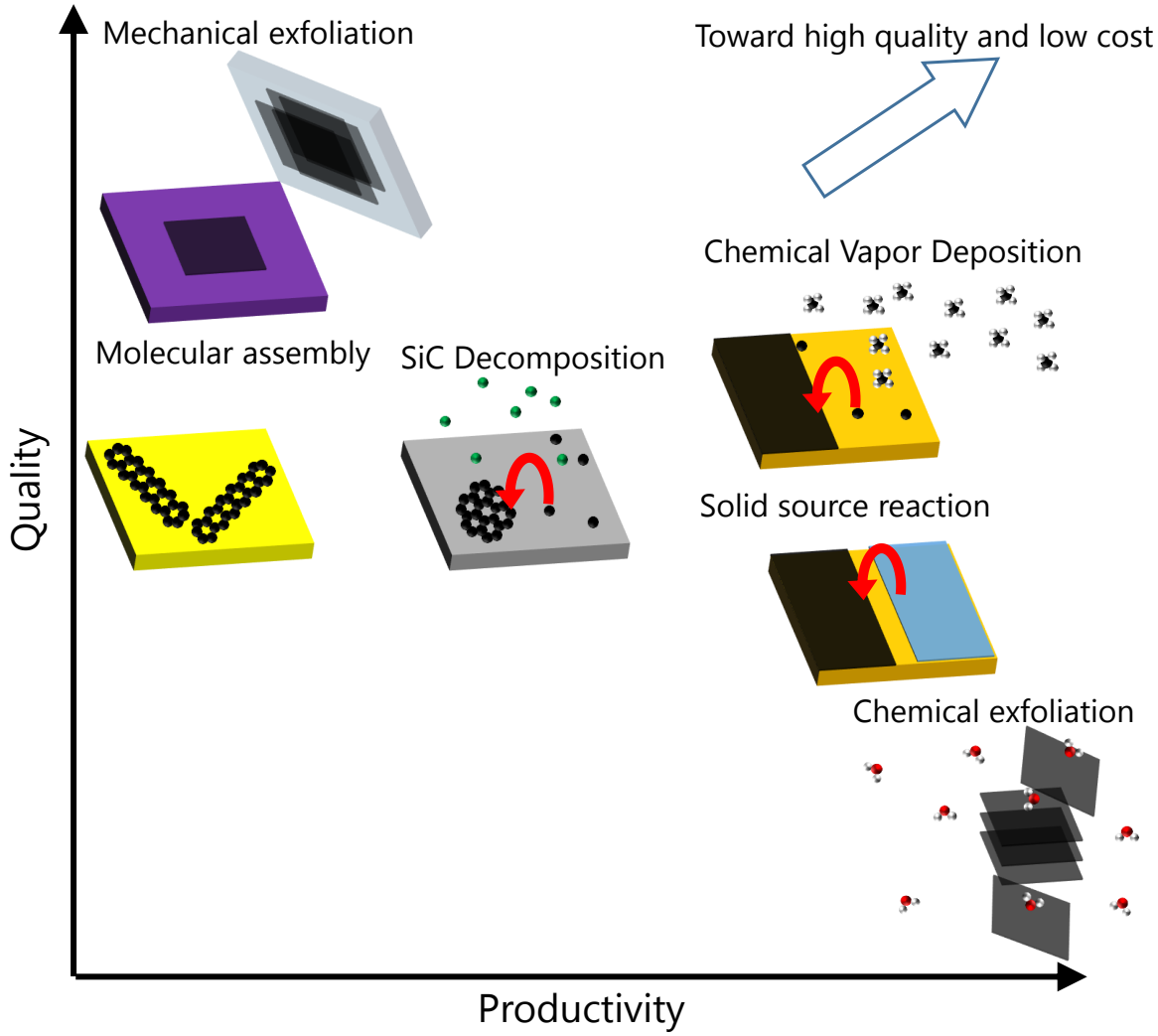

Figure I. 1. 3 Schematic illustrations of fabrication methods of graphene. Black sheets and balls correspond to graphene and C atoms, respectively. Mechanical exfoliation produces the highest quality graphene. Molecular assembly produces GNR despite the high cost. During the SiC decomposition, Si atoms (green balls) sublime faster than C atoms. In CVD, source gas decomposes to C precursors to create graphene lattice. Solid source materials (blue sheet) are converted on the metal catalyst. Oxidized graphene sheet is chemically exfoliated in the dispersion.

exfoliation, SiC decomposition, chemical vapor deposition (CVD), molecular assembly, and solid source reaction.

Since graphites contain graphene sheets, the exfoliation is the easiest way to obtain monolayer graphene. The mechanical and chemical exfoliations of graphene are known as so-called top down methods. Graphene was firstly isolated by the mechanical exfoliation in

which the adhesive tapes were used to peel off monolayer graphene from bulk graphite, as shown in Fig. I. 1. 3[1]. As a result, the monolayer graphene film is obtained on the arbitrary substrates such as SiO_2 (300nm)/Si. The quality of obtained graphene is still the highest among the methods with respect to the carrier mobility. However, the productivity of this method is awfully low. Not only the peeling off but also finding monolayer graphene on the substrate requires a specialist to obtain graphene. In addition, the size of graphene crystal are limited to the starting materials wits sub-centimeters.

The chemical exfoliation of graphite is known as the cheap way of the mass production of graphene[46–48]. Bulk graphite is strongly oxidized by $KMnO_4$ to the hydroxyl, epoxy, carbonyl, and carboxyl groups in the first step of this method. The hydrophilic groups make the graphene sheets dispersible to water, resulting in the monolayer and few layer graphene oxide (GO) dispersion. Subsequently, the chemically exfoliated GO is reduced to graphene in solution phase and is formed on an arbitrary substrate. The GO sheets could also be reduced on the metal substrates[49, 50]. The monolayer graphene sheets are obtained on the substrates. However, the part of graphene lattice is broken during the oxidation and reduction processes. Moreover, the top-down process results in the limited size of graphene sheet which cannot be more than the starting graphite crystal.

In addition to the top-down process, the bottom-up processes are researched to improve the quality and size of graphene. In these methods, the carbon atoms gather and construct the graphene lattice from a simple source material. As the interesting preparation method of monolayer graphene, the thermal decomposition of SiC substrate was developed[51–55]. The faster sublimation of Si atoms leaves C atoms on the SiC substrate to grow the graphene lattice, resulting in the high-quality and monolayer graphene. However, the evaporation of Si atoms requires the high substrate temperature approximately at 1250-1450 °C, and the SiC substrate is expensive, which are not feasible for the industrial fabrications. Moreover, the grown graphene is strongly bound to the substrates, and thus it is difficult to transfer graphene to other substrates.

Chemical vapor deposition is considered the most feasible “bottom-up” method to produce high-quality and large area graphene. The C source gas (typically CH_4 is used) is decomposed

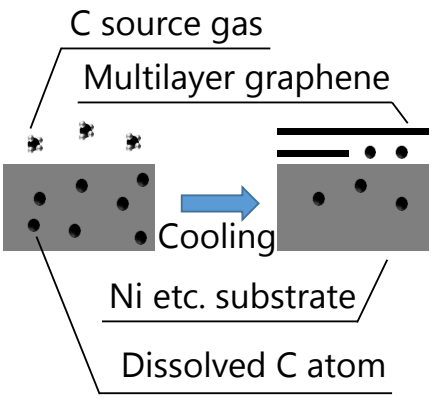

Figure I. 1. 4 Schematic illustration of CVD growth of graphene on Ni and other metal substrates with high C solubilities. Carbon source gas is decomposed to dissolve into Ni at high temperature, and C atoms segregate from Ni to create graphene lattice during the cooling.

on the substrates at high temperature to create the C precursor molecules to form the graphene lattice. Many types of substrates have been attempted for the growth of graphene. The oxide substrates such as sapphire are considered to crack the gases to produce graphene. However, the growth temperature is higher than 1000 °C[56, 57]. The metal substrates can catalyze the decomposition of the source gases at lower temperature. Generally speaking, there are two types of catalytic activities of metal substrates: the segregation and surface-reaction mechanism as shown in Figs. I. 1. 4 and I. 1. 5, respectively. The multilayered graphene is preferentially synthesized by the segregation while the monolayer graphene is uniformly grown by the surface reaction[58, 59]. The size of graphene film can be as large as that of the substrate. For example, the growth of 30 inch graphene film was reported on the Cu foil substrate[60].

In spite of the large area graphene grown by CVD, the productivity of graphene in CVD shows some problems. Graphene is fabricated on the metal substrate by CVD while the most of devices are constructed on the insulating substrates. The graphene grown on metals is thus transferred onto other kinds of arbitrary substrates, SiO_2/Si, for example[61–63]. However, the transfer is one of the detrimental processes for the device fabrication of graphene. The transfer method and the growth of graphene on insulating substrates have been thus investigated[56, 57, 61–63]. In addition to the transfer, the processes of CVD require the

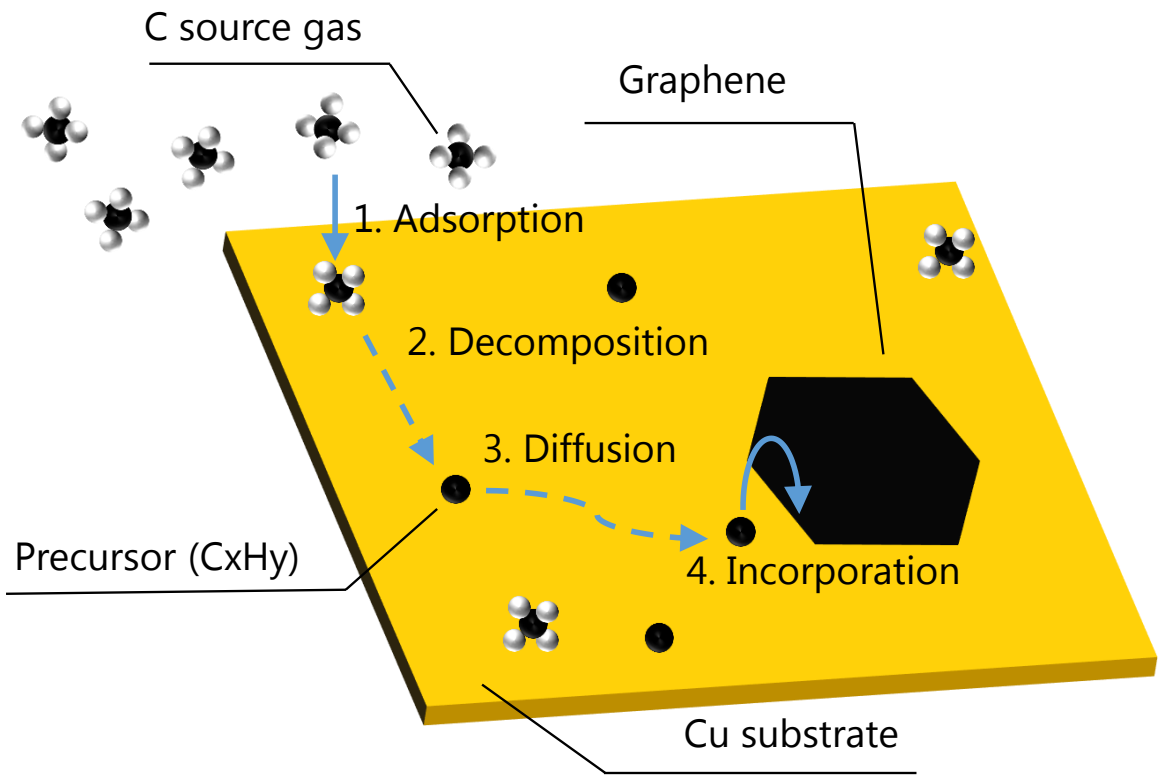

Figure I. 1. 5 Schematic illustration of CVD growth of graphene on Cu substrate and other substrates with low C solubilities. Carbon source gas adsorbs on Cu and decomposes to the precursors, and the precursors diffuse on Cu and are incorporated into graphene lattice.

vacuum and high temperature, which is disadvantageous for industrial fabrications.

The growth of graphene on the metal substrate from other source materials is studied additionally to CVD. The catalytic activity of Au, Ag, and Cu substrates can cause the cycrodehydrogeneration of the poly-aromatic molecules to produce GNR[64–67]. The productivity of this method, so-called molecular assembly, is worse than that in other methods in spite of the atomically controlled structure of graphene edge. The growth from the solid source materials on metal in macroscopic scale is also studied. For example, PMMA polymer, shit of dogs, and cockroach legs are converted to graphene[68, 69]. Although the actual mechanism of these results is not revealed, it might resemble to that of CVD which uses the catalytic activities of the metal substrates.

1.4 Chemical Vapor Deposition of Graphene

Considering the quality and productivity of graphene, CVD is recognized the most suitable way to grow a large-area, single-crystalline, and monolayer graphene. Particularly, the CVD growth of graphene on the Cu substrates is superior to that on other substrates with respect to the selectivity of the number of graphene layers. The carrier mobility of the graphene grown by CVD is inferior to that of the mechanically exfoliated graphene although the defect density is lower than that synthesized by the most of other methods. This is because the graphene grown by CVD is generally polycrystalline while the single crystal graphite is used for the exfoliation. The grain boundaries in graphene films are known to scatter the electrons[70–72]. While the growth of wafer-scale single-crystal graphene is required ideally, most of the investigations report that the grain size of single crystal graphene on the Cu substrates is limited to mm-size[73–84]. The understanding of the growth mechanism of graphene in CVD is indispensable to optimize the growth condition to produce the single crystal graphene. Before the discussion of the optimization of the condition, I explain the two-types of the growth mechanism of graphene catalyzed by Ni and Cu, for example, during CVD in Figs. I. 1. 4 and I. 1. 5, respectively.

The growth mechanism of the segregation process was studied and revealed by the isotope labeling by X Li *et al*. in 2010[59] and other *in-situ* observation methods[85–92]. Nickel and some of other transition metals can create the interstitial compounds with C atoms. The temperature determines the solubility of C atoms inserted between Ni atoms as so-called solid solution. After C atoms dissolved in the solid solution with the solubility amounting 0.9 % at 900 °C[59], the decrease in the temperature causes the segregation of C atoms to form the graphene lattice on the substrate. In this segregation mechanism, the numbers of graphene layers depend on the cooling rate of the substrates. The slow and fast cooling segregates and quenches the dissolved C atoms, thus resulting in the thick and thin layer graphene, respectively[93]. As a consequence, Ni[93, 94] and other transition metals[87, 95–100] produce the large area of graphene while it is difficult to fabricate the uniformly controlled numbers of graphene layers[62, 63, 93].

The CVD growth of graphene on the Cu substrate has been investigated the most intensively because the uniform growth of monolayer graphene is achieved[58]. The weaker interaction of C with Cu than with Ni may suppress the solubility of C in Cu (5 ppm at 1143 K[101, 102]) lower than that in Ni (0.9 % at 900 °C[59]), while both Cu and Ni can create the interstitial compounds in the phase diagrams of those systems. The isotope labeling also indicated that the C precursors decomposed from CH_4 did not dissolve into Cu, unlike into Ni substrates[59]. Instead, the C precursors diffuse, gather to nucleate, and attach to the graphene lattice on the Cu surfaces, as shown in Fig. I. 1. 5. The growth of graphene on Cu is thus slow down after the growth of 1st layer graphene, which gives rise to the growth of uniformly single layer graphene[58, 59]. Other substrates with the low C solubility also produce monolayer graphene, for example on Ge[103], Au[104], Pt[105], and Ir[106–108].

Since the monolayer uniform graphene film was prepared on the Cu substrates, the optimization of the growth conditions is now being investigated. A number of growth parameters such as the total pressure, the partial pressure and flow rate of source gases, and the substrate temperature have been changed for the optimization. Practically, the growth of the single crystal graphene is examined by the suppression of nucleation density to grow a large-area and single-crystal graphene. For example, the growth of graphene on melted Cu, exfoliated Cu, Cu evaporated film, and on the single crystal Cu were studied[80, 82, 83, 109]. In addition to the substrates, the various source gases are tried to optimize the growth process of graphene CVD by changing the precursor structure[110–112]. With respect to the precursor structure on Cu substrate, the C dimer was suggested preferred to C monomer in the theoretical research as shown in Fig. I. 1. 6[113]. In this dissertation, I focus on the growth of graphene from CH_4 because the Cu-CH_4 system has been widely studied since its first report[58].

The CVD growth of graphene on the Cu substrates is usually performed with the supply of H_2 gas in addition to the hydrocarbon gas (mainly CH_4). However, the dissociative adsorption of H_2 and CH_4 on Cu does not occur [44, 114]. The first-principles calculations showed that the formation of graphene from CH_4 on Cu was exothermic[115]. In addition to the effects of H_2, those of O atoms on the Cu substrate were reported to play another role for the growth

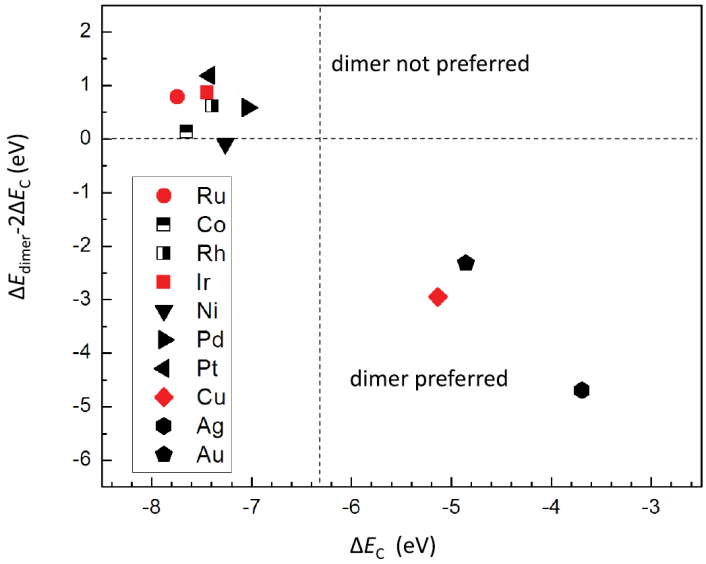

Figure I. 1. 6 Stability of monomer (C_1) or dimer (C_2) on metal substrates [113]. Reprinted figure with permission from Chen, H., Zhu, W. & Zhang, Z., Physical Review Letters **104**, 186101 (2010). Copyright 2010 by the American Physical Society. DOI: http://dx.doi.org/10.1103/PhysRevLett.104.186101

of graphene recently[81, 112, 116, 117]. First, the decomposition of CH_4 is enhanced on the Cu substrate at which O atoms are pre-adsorbed[114]. Second, the nucleation of graphene is suppressed by the surface O atoms, resulting in the large area of graphene grains. Finally, the surface O atoms enhance the detachment of H atoms from the edges of graphene. In this case, the rate-limiting step of the CVD growth of graphene is changed from the edge-attachment to the surface diffusion of the precursors.

Graphene was also reported to be etched by O atoms on the Ru substrates[88, 118, 119]. Graphene was directly etched by O_2 which was intercalated between graphene and Ru. In addition, the growth precursors of graphene were also etched by O atoms, and the depletion of the precursors could etch graphene on Ru. In both cases, the reaction between C and O probably forms volatile CO and CO_2 molecules, and C atoms are removed from the surfaces. However, the effect of the vapor phase O atoms has not been investigated intensively although the density of O atoms can be controlled by the O_2 partial pressure.

In addition to the growth parameters, the optimized condition depends on the method in each research group[81], which makes the issue more complicated. Under these situations,

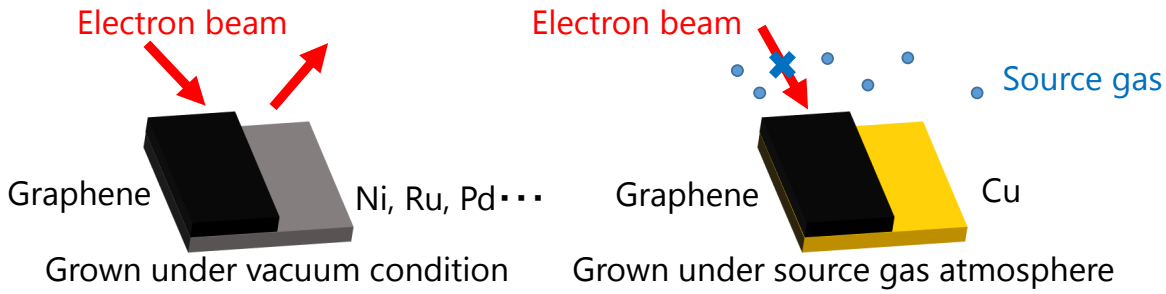

Figure I. 1. 7 Schematic illustrations of electron microscopy during CVD growth of graphene on Ni and Cu. Electron microscopy can work under vacuum conditions while electron beams are scattered by the source gas for the CVD growth of graphene on the Cu substrate.

the feasible ways to understand the growth mechanism completely and to optimize the growth parameters efficiently are required for the growth of single crystal graphene.

1.5 Real-time Observation of Chemical Vapor Deposition Growth of Graphene

Real-time observation during the CVD growth of graphene is essential to understand the mechanism and to optimize the growth parameters. Particularly, the evolutions during the growth and shrinkage features of graphene are taken more easily. Moreover, the real-time observation of graphene growth will open a path to the real-time control of graphene growth.

Actually, the segregation of graphene was observed by low energy electron microscopy or other methods on Ni and other substrates[85–92]. However, the growth of graphene during the surface reaction on the Cu substrates has not been studied by microscopy in real-time sufficiently until very recently. This is because the electron microscope cannot work under the growth condition of graphene with ambient pressure as shown in Fig. I. 1. 7 without using specific techniques such as environmental-SEM[112, 120–122]. Therefore, the growth mechanism in CVD on the Cu substrates was discussed mostly based on the “post-synthesis” observation using Raman-mapping technique and scanning electron microscopy (SEM). Moreover, the lack of the real-time observation has prevent from the control of graphene growth in efficient way and real-time. The optimized growth parameter possibly depends on the growth stage of graphene. However, only a few of researchers achieved such the parameter

changes during the growth[79, 84]. Also the etching mechanism of graphene is not revealed sufficiently in spite of its importance. The etching of graphene is seemingly related to the growth although the relation between the growth and etching has not been investigated so intensively especially in gas-phase conditions. Under these situations, the development of the real-time observation technique in gas-phase conditions is strongly required to understand the growth and etching mechanism more precisely to produce high-quality and large-area of single crystal graphene.

2 Aim of This Study

In this dissertation, I report the development of Radiation Microscopy (RM) for the real-time observation of the CVD growth of graphene on the Cu substrates. The real-time observation is required to optimize the growth parameters efficiently especially on the Cu substrates, on which the large-area, single-crystal, and monolayer graphene can be grown. However, conventional electron microscopes cannot detect the growth of graphene on Cu directly. The previous report of *in-situ* optical measurement provided the advantages of the optical methods[123]. In addition, the optical methods are non-destructive while the electron microscopy can damage the observed materials. Therefore, the optical microscopy is considered suitable for the purpose. Graphene is a thin material with the transparency of 97.7 %[16], which is calculated by the equation,

$$1 - \frac{e^2}{4\epsilon_0 \hbar c^2} = 1 - \pi\alpha_{\text{fine}} \tag{I. 2. 1}$$

where ϵ_0, $\hbar$, and α_{fine} is the vacuum permittivity, Dirac constant, and fine structure constant, respectively. Graphene is invisible in ordinary reflection-mode optical microscopies. The situation in this case is schematically and experimentally described in Fig. I. 2. 1(a, c).

I developed the optical microscopic technique to observe the radiation (thermal emission) from the material at high temperatures. The radiation spectrum mainly depends on the temperature and emissivities of materials. There is a large difference in the emissivity between graphene and Cu, as discussed later in section III. 1.1. On the other hand, the temperature is regarded constant on the most of positions on the Cu surface because of the high thermal

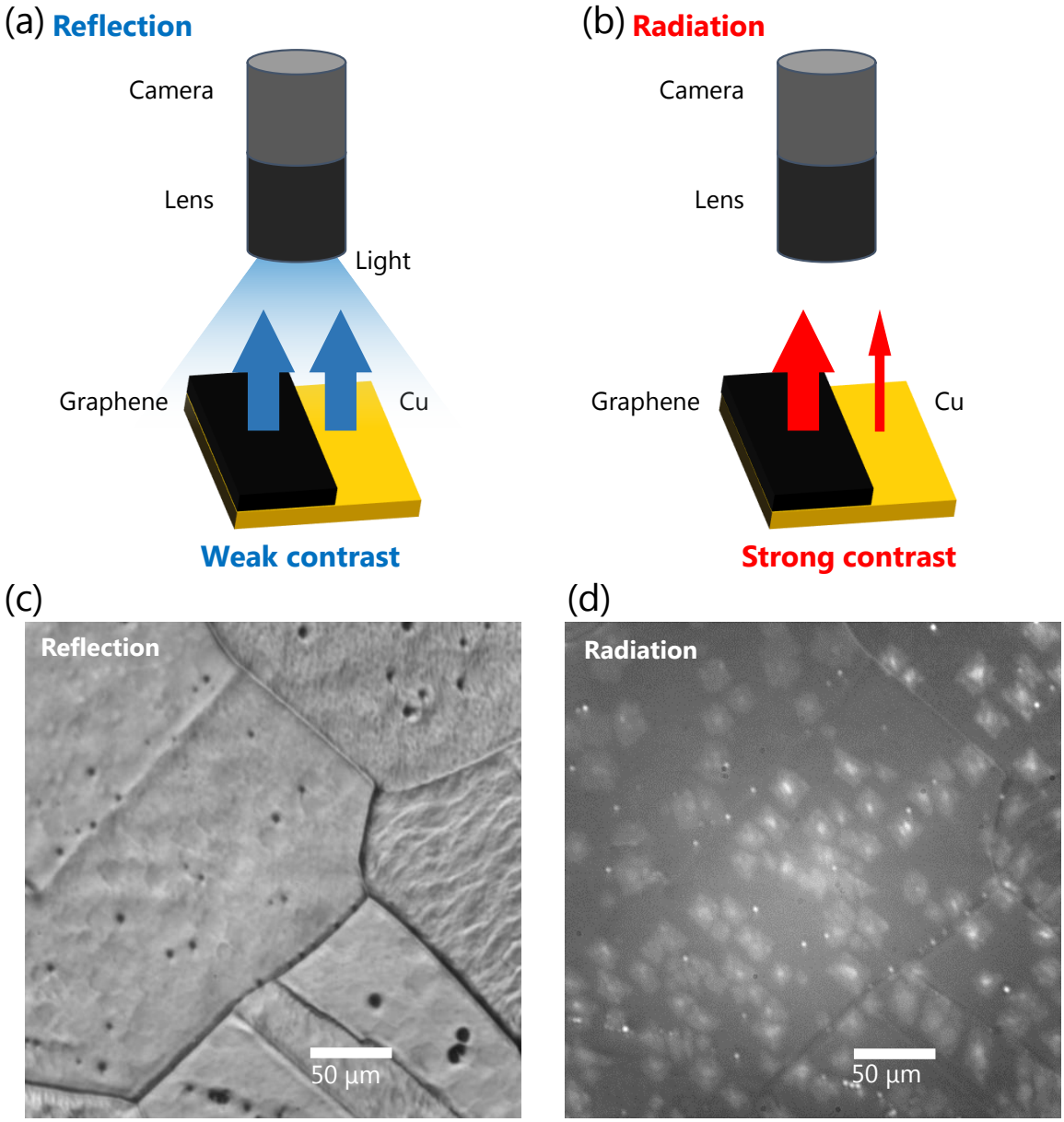

Figure I. 2. 1 Schematic illustrations for (a) reflection-mode optical microscopy and (b) radiation microscope and (c,d) actual image of these methods on identical area. In reflection-mode, the contrast between graphene and the Cu substrate is weak since graphene is transparent. On the contrary, the contrast of radiation lights between graphene and Cu is strong enough due to the large difference in the emissivities of these materials.

conductivity of Cu. For the isothermal sample, the radiation intensity mapping provides the distribution of the emissivities, which gives rise to the distribution of the materials.

I also discuss the mechanism of graphene growth and shrinkage during the CVD growth based on the real-time observation. The nucleation, growth rate, and shrinkage rate of graphene can be extracted from the observed RM images. The dependence on the growth parameters such as the substrate temperature (T_s), CH_4 flow rate, and the O_2 partial pressure is analyzed. Finally, I discuss a possible way to optimize the growth parameters to grown the large area of single-crystal monolayer graphene efficiently.

Part II
Experimental Methods

In this part, I explain the experimental methods used in the present study. The CVD growth of graphene is performed in a vacuum chamber while the growth is observed in real-time by RM. I show the detail of the sample preparation and growth chamber here and describe the development of RM in Part III. In order to compare the RM observation to other methods as shown in Part III, the grown graphene was characterized by SEM and Raman spectroscopy. I also explain these characterization methods including the instruments and their principle to interpret the results.

1 Fabrication Methods

The real-time RM observation requires the suppressing of background radiation from the wall of instruments which is at high temperature in a conventional furnace. The observation of the growth of graphene is thus conducted with the "cold-wall" set-up as shown in Fig. II. 1. 1 in a schematic. The optical microscope consists of the camera and lens system to observe

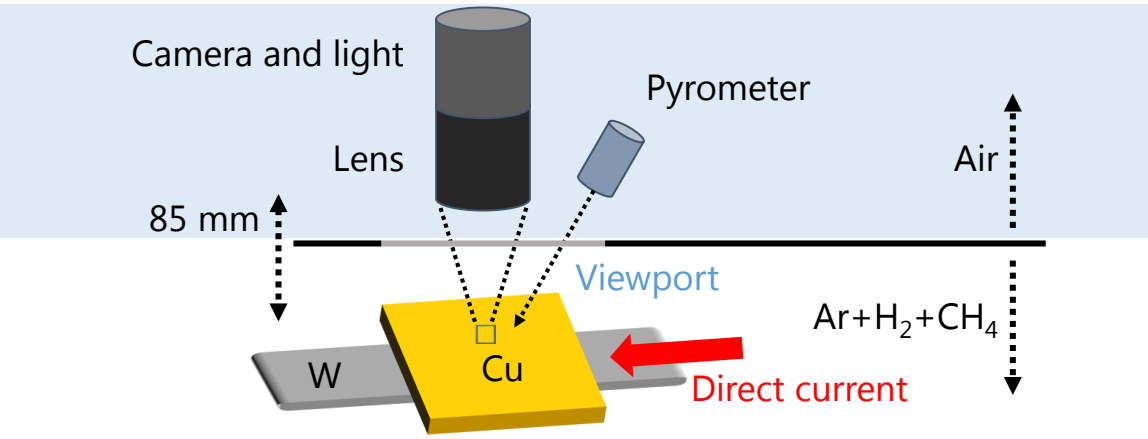

Figure II. 1. 1 Schematic illustration of set-up. The microscope and the pyrometer observe the sample surface through the viewport from the outside of the chamber. The chamber is filled with Ar (1000 sccm), H_2 (100 sccm) and CH_4 (5 sccm) at 2700 Pa. Direct current in the W ribbon heats the Cu foil.

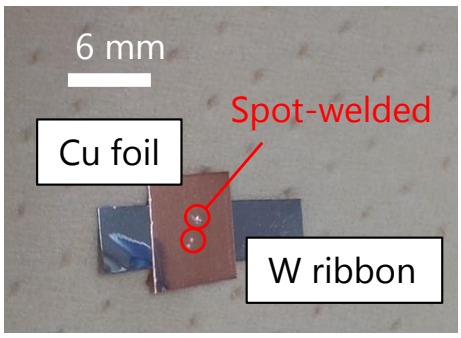

Figure II. 1. 2 Picture of sample composed of welded Cu foil and W ribbon. The welding spots align perpendicular to the long axis of the W ribbon.

the sample surface from the outside of the chamber. It is important for the stable observation to eliminate the vibration of the chamber and microscope and to focus on the sample surface precisely. Here, I explain the set-up in the present study to grow graphene and observe the growth in real-time.

1.1 Sample Preparation

A direct current heating was carried out in the present study to localize the temperature increase only on the sample. A Cu foil (6×6 mm^2, t = 50 μm, 99.99 %, CU-88-83-230, RARE METALLIC, CO., LTD.) was used as a growth substrate. The supplier of a foil was selected taking account of the grain size, the purity, and the polishing scratch of the Cu foils which were the most suitable in the present study as long as I tested. A W ribbon (4×25 mm^2, t =35 μm, W-463242, Nilaco) was welded to the Cu foil using a spot welder (SOLDER MAN DS600). The direct current flew through the W ribbon to increase the substrate temperature T_s by Joule-heating. I call the welded foils as “sample” in the present study. The positions of the welding spots were aligned perpendicularly to the current flow as shown in Fig. II. 1. 2. If parallel, the direct current flew in the Cu foil rather than the W ribbon, preventing the heating of sample due to the higher conductivity of Cu than W. The sample was settled onto the Cu electrode as shown in Fig. II. 1. 3. Other Cu foils were additionally welded to the W ribbon between the W ribbon and Cu electrode to reduce the contact resistance. Without this procedure, the contact resistance values become different at the two terminals, which makes the temperature gradient in the W ribbon.

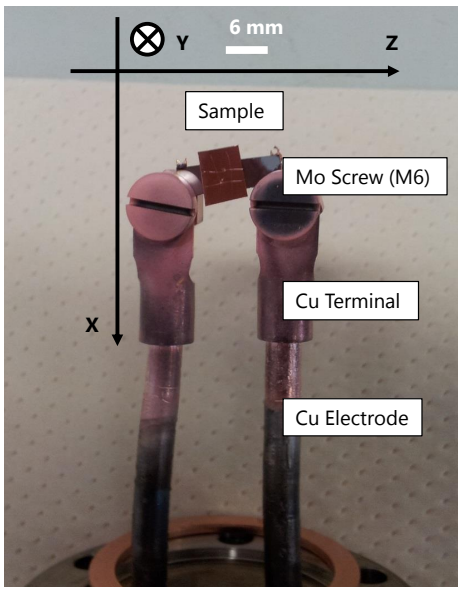

Figure II. 1. 3 Picture of sample settled on Cu electrode. The X, Y, and Z axes are same as in Fig. II. 1. 4.

1.2 Growth and Observation Chamber

Graphene was grown in a vacuum chamber equipped with gas introduction valve, view port, variable leak valve for the introduction of O_2, O_2 analyzer (LD-450, Toray Engineering Co., Ltd.), Cu electrodes, and the crystal/cold cathode gauge (CC-10, Tokyo Electronics Co. LTD.). Figure II. 1. 4 is the photograph of the chamber for the real-time RM observation of graphene grown by CVD. The precise control of the temperature, CH_4 flow rate, and O_2 partial pressure achieved the qualitative analysis on how the growth of graphene depends on such the parameters as described in section IV. 2.

I explain the details of the chamber in the followings. The system can be evacuated to 2.0×10^{-5} Pa by a rotary pump (RP) and a turbo molecular pump (TMP). The combination of a passive damper and a heavy anchor reduces the vibration from RP. Graphene was grown by the mixture of source gases of $Ar/H_2/CH_4$ which was supplied through the gas introduction valve. Oxygen was introduced through the variable leak valve which could control the flow of gas precisely. The O_2 partial pressure was evaluated by the vacuum gauge and the O_2 analyzer. The view port of ICF-70 flange with a quartz glass was used for the optical microscopy

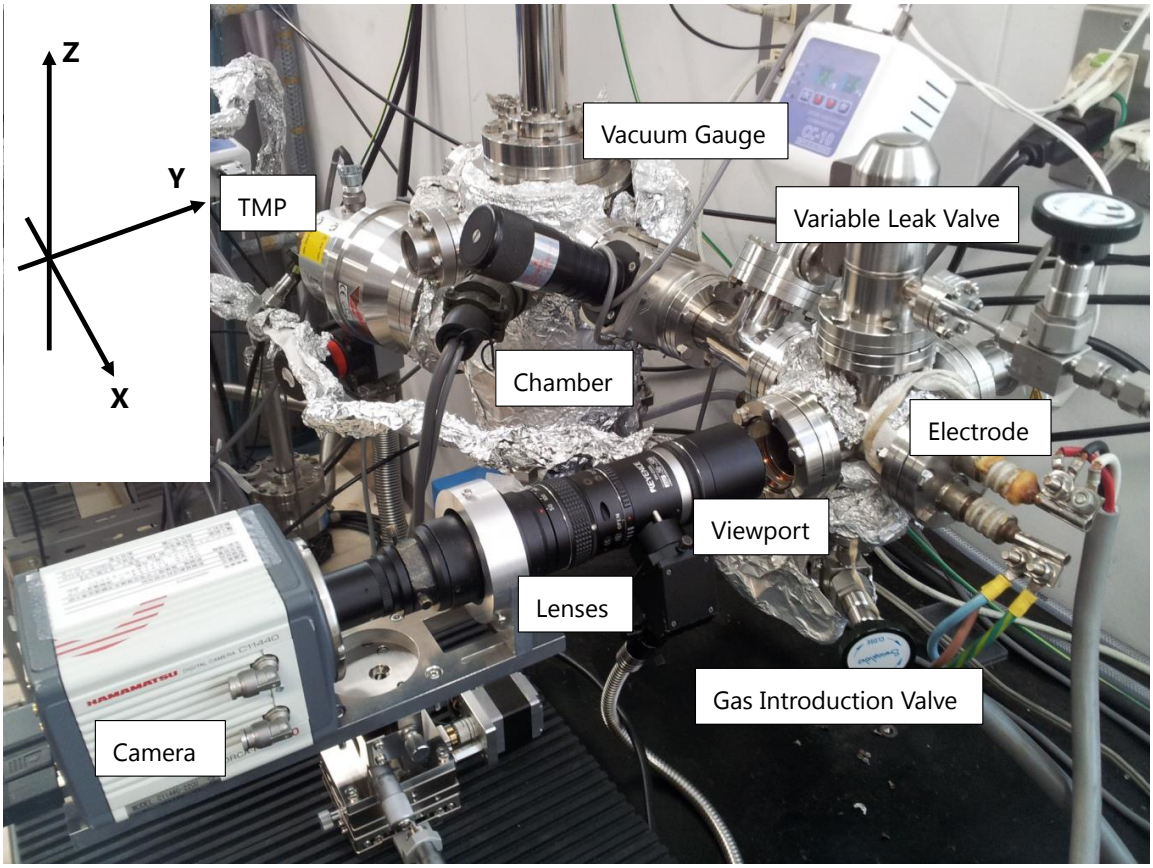

Figure II. 1. 4 Photograph of growth chamber and optical microscope. The inset shows the definition of X, Y, and Z axes in the main text. The sample is vertically set inside the chamber and is supported by the electrode.

by a camera and lens system and for a pyrometer to observe the temperature of the sample.

The set-up of the microscope is written as follows. The optical microscope consists of the camera (ORCA-Flash4.0 V2 C11440-22CU, Hamamatsu Photonics K. K.) and the zoom-lens (VH-Z50L, Keyence Co.) are settled to aim the sample surface through the view port. Judging from the experience to test various cameras, the dynamic range of the camera is quite important to distinguish the emissivities of materials. The lens with the working distance of 85 mm was suitable for the observation from the outside of the chamber. The magnification of lens and the eyepiece was ×500 and ×4, respectively, and they are made of glass and partially CaF_2 although the detailed information of the lenses is confidential in Keyence. Ltd. The camera records the whole experiments by using “HCImage” software bundled with

the camera. The typical RM image was taken with the exposure time and colour depth of 500 ms and 16 bits, respectively. The observed area was 326×326 μm^2 corresponding to 1024×1024 pixels, so that the size of pixels is 316×316 nm^2. The camera and lens system is horizontally based on manual micro-stages for X and Z axes and a motorized micro-stage for Y axis. The X, Y, and Z axes are defined as shown in Fig. II. 1. 4. If, unlike the set-up shown in Fig. II. 1.4, the microscope and sample is set vertically and horizontally, respectively, the observation is prevented by the vibration in the present set-up. The Y micro-stage adjusts the focus of the microscope on the sample surface while the X and Z micro stages position the microscope to aim a certain area on the sample surfaces. The X, Y, and Z micro-stages are settled on a passive damper to reduce the vibration. The set-up of the microscope is important to eliminate the vibration to achieve the real-time RM observation during the CVD growth of graphene.

1.3 Procedure for Growth and Shrinkage of Graphene

Graphene is grown under $Ar/H_2/CH_4$ atmosphere which has been developed for the CVD growth on the Cu substrates[58]. The procedure of the experiment is schematically shown in Fig. II. 1. 5. At first, the sample was loaded into a vacuum chamber. The sample was fixed by

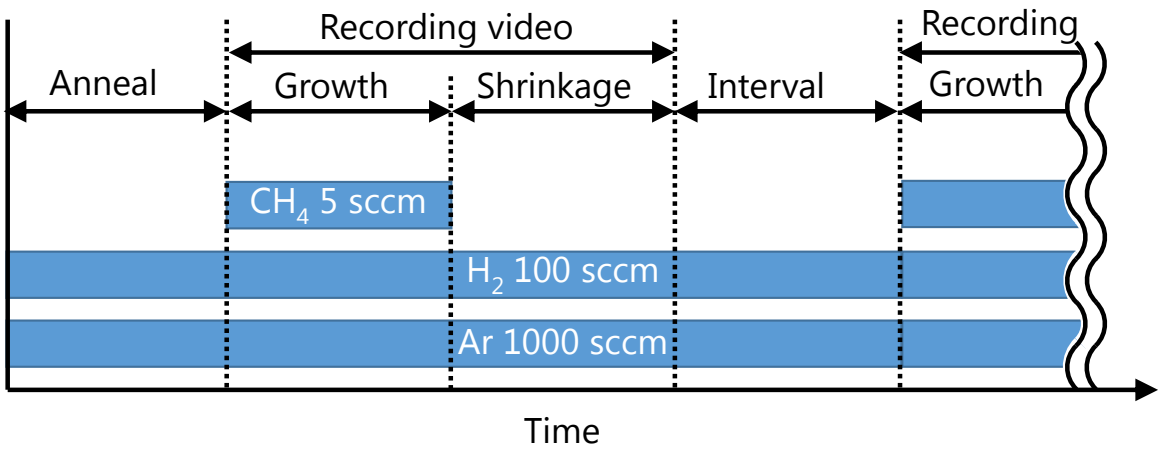

Figure II. 1. 5 Schematic illustration of sequence for repeated growth and shrinkage of graphene. After the supply of CH_4 was shut-off, graphene stopped the growth and started the shrinkage. The complete disappearance of graphene was followed by waiting for 10 min until the restart of the next experiment.

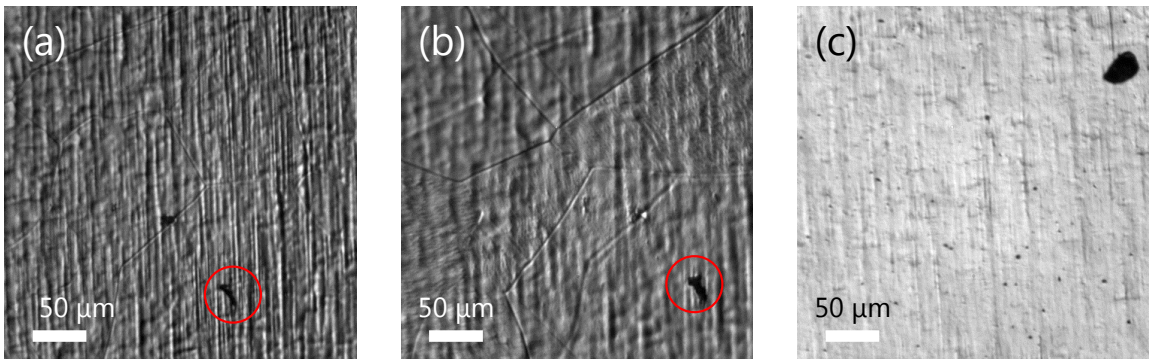

Figure II. 1. 6 Reflection-mode optical microscopy confirmed surface of Cu flattened. (a) Before and (b) after the anneal for 10 min. The red circles correspond the same particle on the surface. (c) Flatten surface of same sample as (a) and (b) after the anneal twice more.

Cu electrodes of the chamber taking account of the tilt angle. The Joule-heating sometimes distorted the W ribbon to tilt the sample surface from the perpendicular. After the settlement of the sample, the chamber was evacuated below 3×10^{-5} Pa after one night. The TMP was stopped while RP kept roughing pumping to the O_2 partial pressure to be 0.04 Pa. The O_2 gas was introduced to the desired O_2 partial pressure through the variable leak valve. The mixture of Ar/H_2 gases at 1000/100 sccm was introduced until the total pressure reached 2700 Pa. All the experiments were conducted under these flow rates and total pressure. The direct current of 40 A, which was accompanied with the electric potential of 1 V in the present set-up, was applied to the sample to increase the temperature at approximately 1000 °C confirmed by a pyrometer. The temperature of the chamber wall increased only slightly during the experiments. This "cold wall" set-up probably reduces the radiation and the particle which could be a background noise and the nucleation center of graphene, respectively. The sample was heated in H_2 rich atmosphere for 10 min to remove the oxide impurities on the Cu surfaces before the growth of graphene. The sample surface became flat during this cleaning process as shown in the optical microscopic images in Fig. II. 1. 6. The W ribbon was sometimes distorted by Joule-heating as mentioned before. In this case, the sample drifted slightly and was stabilized during the H_2 annealing for 10 min as also shown in Fig. II. 1. 6. The CH_4 of 5 sccm was introduced to grow graphene as shown in Fig. II. 1. 5. After the shut off of CH_4

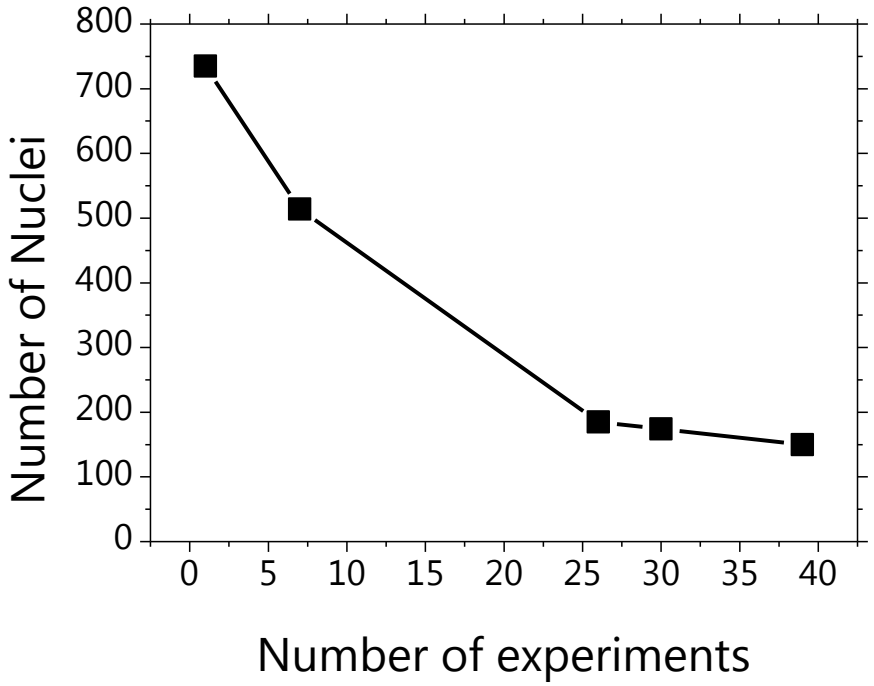

Figure II. 1. 7 Number of nuclei as a function of number of experiments. Graphene was grown at 950 °C with the CH_4 flow rate of 5 sccm at the O_2 partial pressure of 0.04 Pa. The data points with such the growth conditions are selected from the series of the experiments on the identical sample. The number of nuclei decreases with the number of experiments, suggesting the nucleation centers are removed during the growth and shrinkage of graphene. Finally, the nucleation density saturates to a certain value.

supply, the grown graphene started the shrinkage in the present experimental conditions. Finally, the graphene grains disappeared from the Cu surface completely. The shrinkage is not a common phenomenon, and thus its mechanism is discussed in section II. 2.4.2. Owing to these growth and shrinkage processes I could observe the growth and shrinkage dependence on the growth parameters for the identical samples in the series of the experiments.

The repeated experiments of the growth and shrinkage were considered to change the conditions of surfaces. Actually, the nucleation density of graphene decreased with the repeated growth as shown in Fig. II. 1. 7, suggesting that the nucleation centers were removed. As discussed later in section IV. 2.1.1, the quantitative evaluation of the nucleation density is one of the key issues in the discussion of the growth mechanism. However, the number of repeated growth saturated the change of nucleation density, and thus I conducted the series

of experiments for analysis after the nucleation density saturated.

2 Characterization Methods

The comparison of the RM observation to other method is indispensable to prove that the real-time RM is applicable for the observation of the CVD growth of graphene. I characterized grown graphene by SEM and Raman spectroscopy after the synthesis. Here, I explain these “post-synthesis” characterizations.

2.1 Scanning Electron Microscopy

Scanning electron microscopy was carried out with the equipment, JSM6510/JEOL Ltd. The high resolution micrographs whose magnification was typically ×20-2000 were observed to analyze the shape and the number of layers of the graphene grains. The SEM observation was conducted under 10 Pa with the acceleration energy of the electron of 5 kV. It should be noted that the C contamination was considered deposited on the sample during SEM observations. The SEM observations were thus conducted after other observations.

2.2 Raman Spectroscopy and Mapping

Raman spectroscopy is a powerful tool to characterize nano-carbon materials with respect to the quality and quantity of those. In particular, the graphene transferred onto the SiO_2/Si substrates provides richer information than that on the Cu substrates. Here, I explain the general information of Raman spectra of graphene and the mapping measurement. I also show the transfer method of graphene from the Cu substrates to the SiO_2/Si substrates for the detailed Raman measurements.

2.2.1 Equipment and Principle

The Raman measurements were carried out with the equipment (NRS-3000, JASCO). The laser light with the wavelength of 532 nm was used for the excitation. General principle of Raman scattering is shown in Fig. II. 2. 1. The electron excited by the incident light to a virtual state returns to a vibrational excited state to emit the scattered light. For the Raman scattering in solid materials a phonon can be generated by the energy difference between the

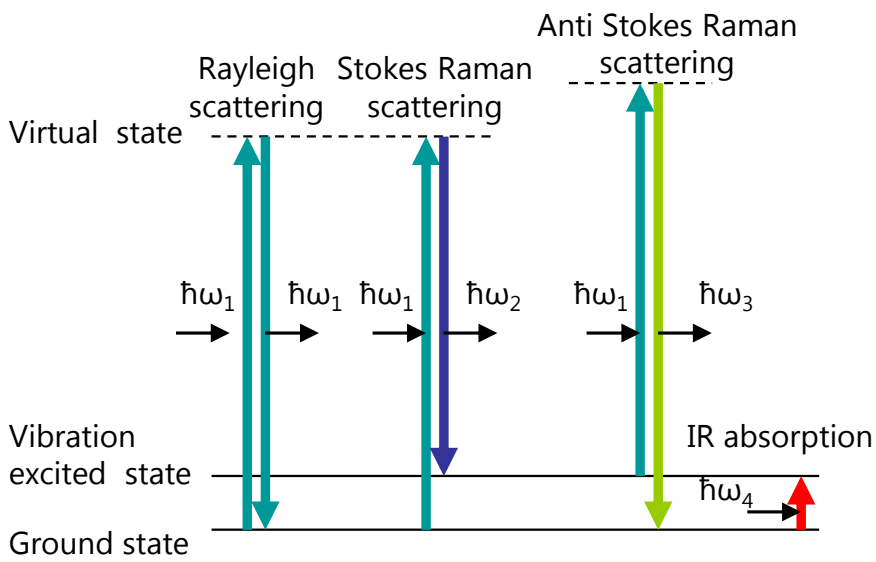

Figure II. 2. 1 Schematic illustration of Rayleigh, Stokes-Raman, and anti-Stokes-Raman scattering and IR adsorption. The vibrational excited states correspond to the phonon excited states in solids.

incident and scattered light. The tiny momenta of these lights result in the generation of the phonon with the crystal momentum of only zero as the selection rule due to the conservation of momentum.

2.2.2 Raman Spectroscopy in Graphene

Figure II. 2. 2 shows the typical Raman spectrum in the present study. I explain the features of the Raman spectra in graphene using this figure with the basis of the previous reports[36–38]. One of the main bands of the Raman spectrum of graphene is a G band appearing around 1580-1600 cm^{-1}. The generation of an E_{2g} phonon at the Brillouin zone center, which is the vibration of sp^2 C bonds in the analogy of the molecular vibration, corresponds to the G band. The origin of G band is so simple that the G band intensity reflects the quantity of sp^2 C rings in the observed area.

The D band at 1340-1360 cm^{-1} is probed as the characterization of the defects of films. This band originates the A_{1g} in-plane transverse optical (iTO) phonon at the K point of graphene in the reciprocal space (the reciprocal lattice is shown in section I. 1.1). Since the A_{1g} mode, which is the breathing mode of the sp^2 C rings, has a finite momentum, the gener-

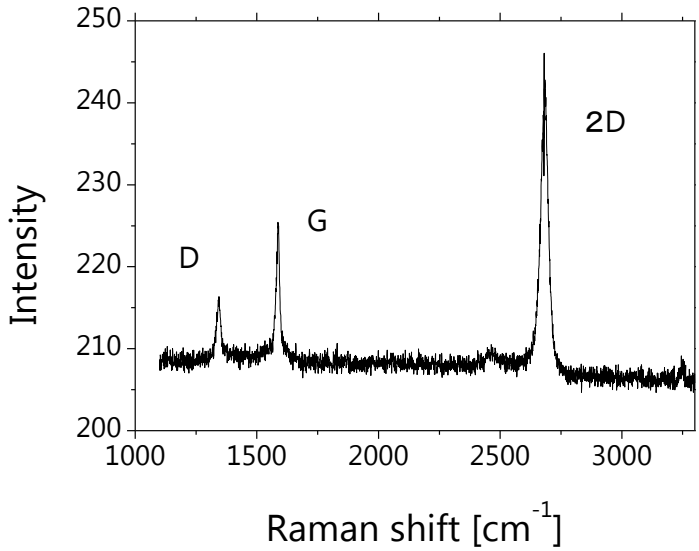

Figure II. 2. 2 Typical Raman spectrum measured in graphene on SiO_2 (300 nm)/Si. The D, G, and 2D peaks are observed at around 1350, 1580, 2700 cm^{-1}, respectively.

ation of this mode is forbidden in the case of the perfect lattices. In the defected graphene, on the other hand, the D band can be observed. The so called double resonant Raman scattering processes, as shown in Fig. II. 2. 3, realize the generation of the iTO phonon mode. One of the excited electrons or holes in a certain valley (an energy band at K points) is scattered by the iTO phonon and another is by the elastic scattering at the edge or defect in graphene to the neighbor valley. They recombine there as shown in Fig. II. 2. 3(d, e). There are little possibilities of two scattering processes; however, twice resonance in the scattering process with the real-states in graphene overcomes such low possibility. As a result, the D band intensity reflects the number of defects and the edge structure of graphene lattices in the observed area. Practically, the intensity ratio of the D band to G band (I_D/I_G) is inversely proportional to the grain sizes of polycrystalline graphene (L_a) as the following equation,

$$I_D/I_G = C(\lambda)/L_a \tag{II. 2. 1}$$

where λ and $C(\lambda)$ is a wavelength of excitation light and a constant, respectively[124]. They are calculated as the relation

$$C(\lambda) = 2.4 \times 10^{-10} \times \lambda^4. \tag{II. 2. 2}$$

In the present study, the D band is not observed in as-grown graphene on the Cu substrates.

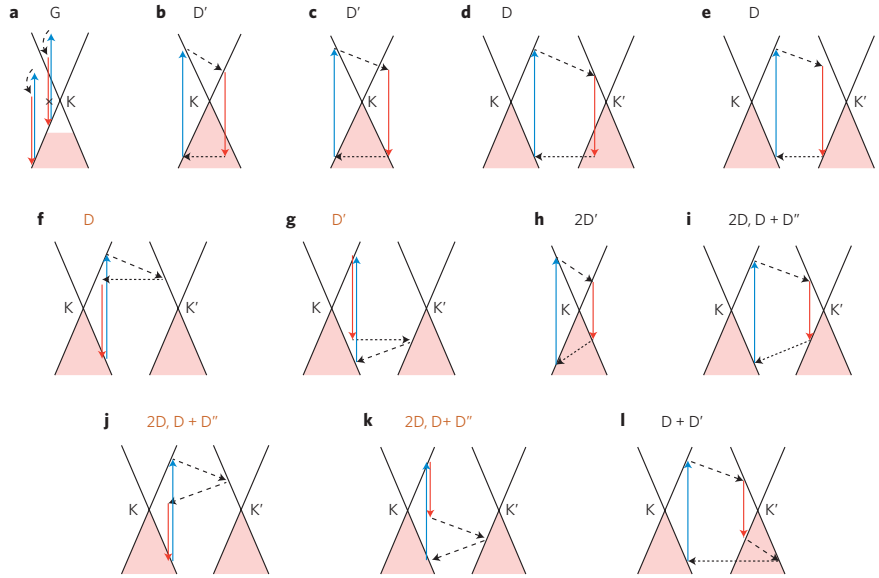

Figure II. 2. 3 Scattering and resonance mechanism of double resonance Raman scattering in graphene. The D' and D" bands originated from other scattering and resonance process than D. The difference in (b, c, g), (d-f), and (i-k) reflects the different resonance points such as for example electron-electron, electron-hole, and electron-hole (in another valley) in (b, c, g), respectively[38]. Reprinted by permission from Macmillan Publishers Ltd: Nat. Nanotechnol., Ferrari, A. C. & Basko, D. M., Raman spectroscopy as a versatile tool for studying the properties of graphene. **8**, 235-46 (2013)., copyright (2013).

After the transfer onto SiO_2/Si substrates the D band appears in the Raman spectra presumably due to the defect formation during the transfer processes.

The strong 2D band compared to the G band (I_{2D}/I_G ratio more than 1.5 typically), which is the second overtone of D band at 2680-2720 cm^{-1}, is observed in the perfect monolayer graphenes such as the exfoliated graphene although the generation of D band phonon is forbidden. The double-resonant Raman scattering also plays an important role in this phenomenon. The pair of the excited electron and hole is scattered by the pair of iTO phonons whose crystal momenta possess the reverse direction. The pair of the electron and hole scattered to the neighbor valley recombine there as shown in Fig. II. 2. 3 (i). As the electron and hole bands at K and K' points degenerate in the monolayer graphene, the single 2D peak is observed in spite of the many possible processes for example in II. 2. 3 (j, k). In this, case the intensity ration of I_{2D}/I_G becomes more than 1. However, the I_{2D}/I_G in the bilayer graphene

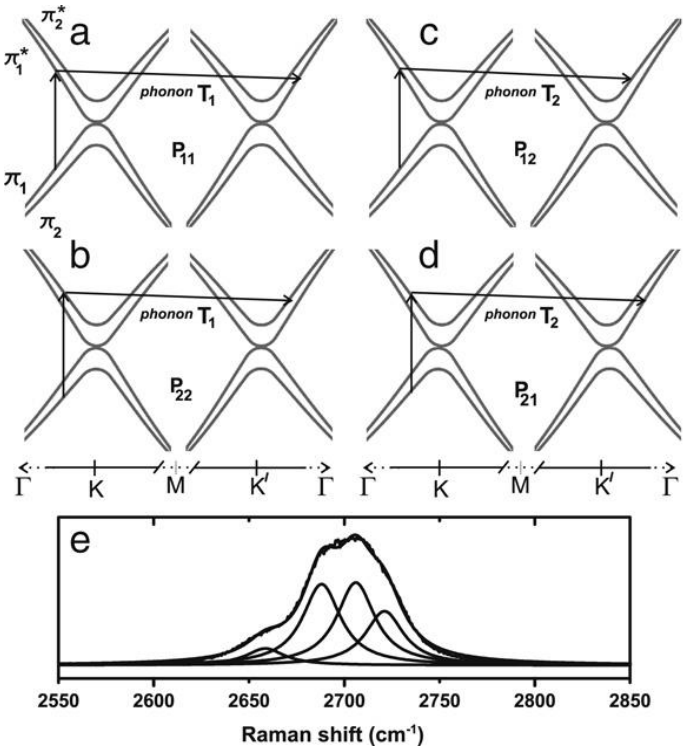

Figure II. 2. 4 Schematic illustration and experimental result of Raman 2D band in AB stacked graphene[37]. The different scattering and resonance process in (a-d) generates the different energy phonon, resulting in the broad 2D peak in (e). Reprinted from. Physics Reports, **473**, Malard, L., Pimenta, M., Dresselhaus, G. & Dresselhaus, M., Raman spectroscopy in graphene, 51-87, Copyright (2009), with permission from Elsevier.

decreases less than 1 from that in the monolayer graphene. This is because the conduction and valence bands in the AB-stacked bilayer graphene as shown in Fig. II. 2. 4 do not degenerate, which gives rise to the processes with the generation of various phonons. Therefore, the 2D band intensity becomes useful to characterize the monolayer and the stacked graphenes. Actually, the 2D band intensity is not directly related to the number of graphene layers but to the band structures of graphene. The effects of the electronic doping from the impurity, substrate, and gate dielectrics are reported to tune the 2D band feature of graphene[125, 126]. While the AB stacked bilayer or trilayer graphene decreases the 2D band intensity, the low interaction of turbostratic stacking preserves the strong 2D band[127, 128]. Therefore, the 2D band intensity in Raman spectra provides not only the atomic but also the electronic structure of graphene.

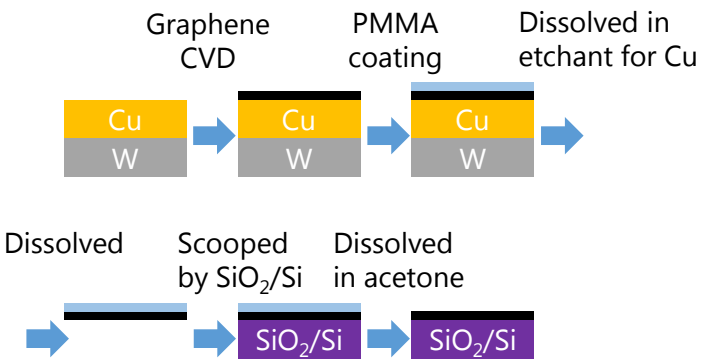

Figure II. 2. 5 Schematic illustration of transfer of graphene by common method with PMMA.

2.2.3 Mapping Observation

The numerical information can be deduced from Raman spectra, and thus the mapping of the intensities can illustrate the spatial distribution of the characteristics of graphene films. The peak position, intensity, width, and the intensity ratios of peaks are usually described in the research fields of nano-carbons. For example, the Raman G band intensity mapping depicts the amounts of sp^2 C rings of the substrates. The I_D/I_G ratio mapping is often used to describe the distribution of defect density. The I_{2D}/I_G ratio mapping can also provide the information about the distribution of the structure of graphene such as the number and the staking orientation of graphene layers. I described such a mapping to explain the structure of grown graphene in the present study.

2.2.4 Transfer

The grown graphene was transferred from Cu substrate to SiO_2/Si substrate by Au deposition method in the present study. In the common transfer process, the graphene is coated by PMMA (Polymethyl methacrylate) or other polymer, and the Cu (or other metal substrate) is etched in the etching solution as shown in Fig. II. 2. 5. The sample with polymer floating on the solution surface is then scooped by the substrate such as SiO_2 (300 nm)/Si. Finally, acetone or other organic solvent etched PMMA on graphene/substrate structure. In this process, however, the residual PMMA on graphene and defect formation on graphene during transfer are considered detrimental to the properties of graphene[13, 129]. Therefore,

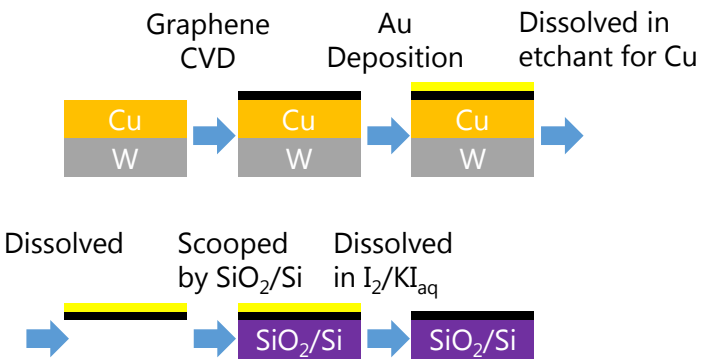

Figure II. 2. 6 Schematic illustration of transfer of graphene using Au deposition. Ammonium persulfate was used as the etchant for Cu in the present study.

the transfer technique has been developed recently. In the present study, I used Au coating on graphene[103] as shown in Fig. II. 2. 6. First, I evaporated 50 nm thick Au film onto graphene on the Cu substrates in a vacuum chamber. The Cu substrate was etched by ammonium persulfate. After the scoop of Au/graphene film on the solution surface and the cleaning by water, the Au film was etched by KI/I_2 solution. Finally, I obtained graphene on the SiO_2 (300 nm)/Si substrate without using PMMA for the detailed Raman mapping measurement to analyze the structure of graphene precisely.

Part III
Development of Radiation Microscopy

In this part, I describe the development of RM. I show the principle of the radiation from the material and the experimental methods to detect the radiation by the optical microscope for RM at first. Before discussing the growth mechanism of graphene during CVD, I confirmed whether the RM can distinguish graphene from Cu or not by the comparison of the RM images to the images obtained by "post-synthesis" characterizations.

1 Concept of Radiation Microscopy

Here, I explain the concept of the present method to observe the thermal radiation to distinguish graphene from Cu. I also introduce the experimental methods focusing on the observed wavelength, the temperature dependence, and the spatial resolutions.

1.1 Principle of Radiation

As Max Planck reported in 1901, the radiation intensity of a material depends on the wavelength of radiation light and the temperature[130]. I show the principle of the RM observation based on the Planck's law and the gray body model as follows. The radiation intensity $I(\nu, T)$ per unit area, per unit solid angle, and per unit frequency is written by the equation

$$I(\nu, T) = \frac{2h\nu^3}{c^2} \frac{1}{\exp(h\nu/k_B T) - 1} \tag{III. 1. 1}$$

where ν, T, c, and k_B is the frequency of the radiation light, temperature, the speed of light, and the Boltzmann constant, respectively. The equation

$$I(\lambda, T) = \frac{2hc^2}{\lambda^5} \frac{1}{\exp(hc/\lambda k_B T) - 1} \tag{III. 1. 2}$$

was used for the discussion of the wavelength λ of the radiation light.

Although the Planck's law is applicable for the black-body, the radiation intensity of the actual materials decreases from that of the black-body. Practically, the radiation intensity is

written by

$$I(\lambda, T) = \epsilon \frac{2hc^2}{\lambda^5} \frac{1}{\exp(hc/\lambda k_B T) - 1} \tag{III. 1. 3}$$

where ϵ is the emissivity of the material. The radiation intensity is also dominated by the emissivities of materials in the "gray-body" model. Kirchhoff's law of thermal radiation reveals

$$\epsilon = \alpha \tag{III. 1. 4}$$

where α is the absorptivity of the materials. The absorptivity α and the emissivity ϵ of the black body are thus unity. Simply saying about this law, a couple of surfaces composed of the same material, at the same temperature, and facing each other should be in thermal equilibrium. In this case, the intensity of the thermal radiation and absorption of the surfaces, namely ϵ and α, should be equivalent each other. The emissivities of the materials, which relate to the various absorption mechanism, thus depend on many factors: the wavelength, temperature, surface orientation, surface oxide layers (for metal) and so on. The radiation intensities of Cu and graphene remain unchanged dramatically during the experiment, even under the condition with the increased O_2 partial pressure. Therefore, I treat the emissivities as constants depending only on the materials.

In this dissertation, I observed the radiation light from graphene and Cu substrates. I discuss the emissivities of these materials in the followings. The absorptivity of monolayer graphene (α_{gra}) is written as

$$\alpha_{\mathrm{gra}} = 0.023 \tag{III. 1. 5}$$

in the previous reports[15, 16]. The emissivity of monolayer graphene is thus determined to be 0.023 which is theoretically following the equation III. 1. 4 and was experimentally confirmed [131]. Unfortunately, I cannot compare this emissivity value to the emissivity of monolayer Cu film. On the other hand, the emissivities of bulk graphite and Cu were experimentally reported to be 0.8[132, 133] and 0.03[134], respectively, for flat and un-oxidized surfaces. The Cu surface is annealed to be flattened and chemically reduced by the presence of H_2 and CH_4 during the CVD growth of graphene. Therefore, I presume that the emissivity of the monolayer graphene is seemingly larger than that of the monolayer Cu judging from those of the bulk Cu and graphite.

In our laboratory, the growth of graphene from graphene oxide on Pd substrates was also observed by RM in real-time[135], while the contrast of graphene on Pd was weaker than that of graphene on Cu owing to the higher emissivity of Pd than that of Cu[136, 137]. Raman spectroscopy revealed that the observed graphene was multilayered, which is consistent with the fact that graphene segregates on Pd[96]. This result suggests that the RM can be applicable for other film substrate systems with the sufficient difference in emissivities.

1.2 Experimental Methods of Radiation Microscopy

Here, I introduce the experimental methods of RM while the set-up is described in section II. 1. I show the detection wavelength, the temperature dependence, and the spatial resolutions which are important information of RM as one of the microscopies.

1.2.1 Wavelength for Radiation Microscopy

The main concept of the present method is to observe the thermal emission of the near-infrared and visible light from the high temperature materials. On the isothermal surface, the radiation intensity depends on the emissivities of materials, which gives rise to the mapping of materials. Figure III. 1. 1 shows the calculated radiation intensity from the Planck's law as a function of the wavelength from 400 to 1000 nm at the temperature of 1000 °C which is the typical value for the growth of graphene. The peak top of wavelength (λ_{max}) is calculated by the Wien's displacement law as

$$\lambda_{max}(T) = \frac{b}{T} \tag{III. 1. 6}$$

where b is the Wien's displacement constant equal to 2.8977721×10^{-3}[K· m]. The radiation intensity further increases from 1000 to 2200 nm. On the other hand, the sensitivity of the CMOS camera (ORCA-Flash4.0 V2) which I used to detect the radiation light has the peak top amounting 70 % with the wavelength of 600 nm and sharply decreases to 60 and 20 % with that of 700 and 900 nm, respectively[138]. The effective radiation intensity, which is the products of the radiation intensity and the camera sensitivity, has the peak top at ~ 800 nm as shown in Fig. III. 1. 2. The absorptivities of the viewport and lenses do not depend on the wavelength in this region. The wavelength of the observed radiation is thus in visible to near-infrared region. The experimental observation of the radiation from graphene in visible

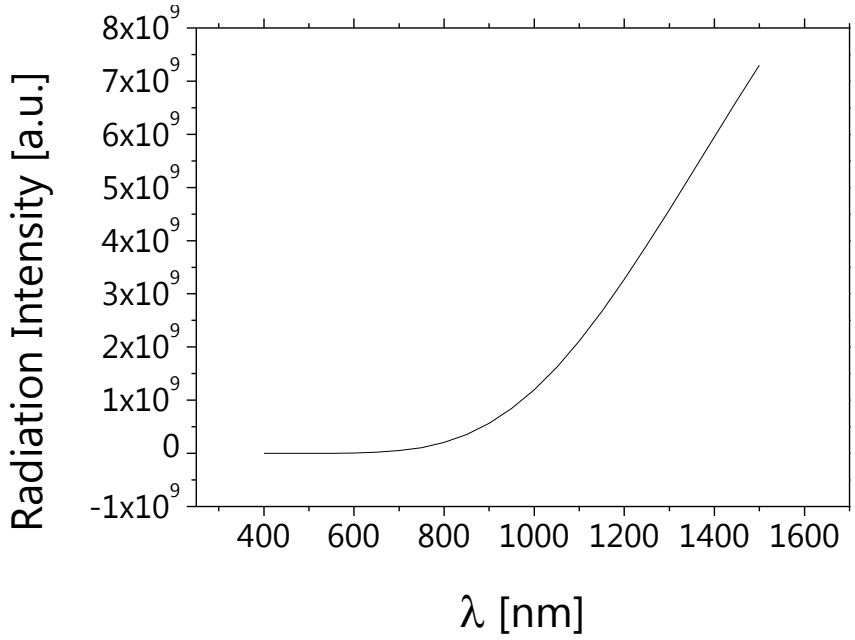

Figure III. 1. 1 Radiation intensity calculated as a function of wavelength (λ) according to Planck's law.

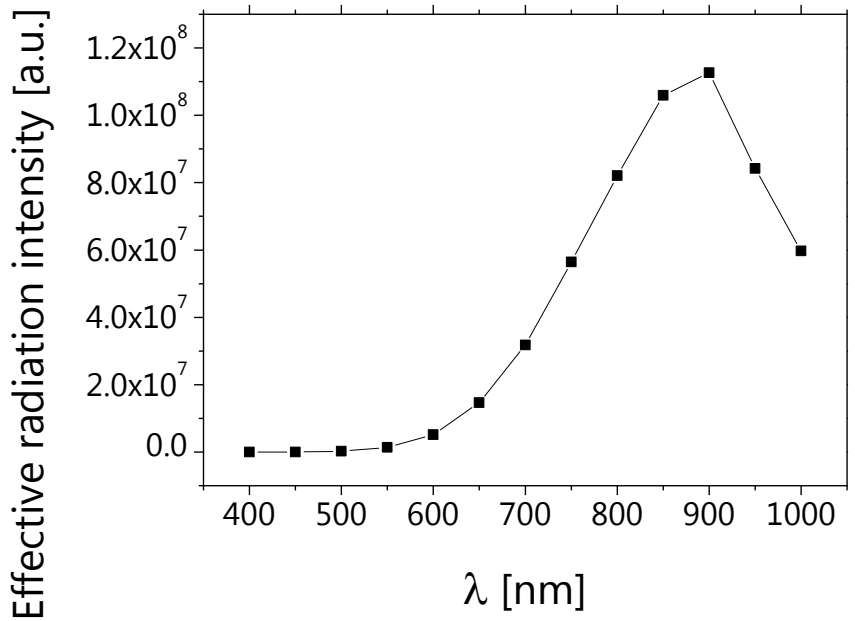

Figure III. 1. 2 Effective radiation intensity as a function of wavelength (λ). The effective radiation is a product of the intrinsic radiation intensity and the sensitivity of the camera.

light region was reported[139].

1.2.2 Spatial Resolution

Here, I discuss the spatial resolution of RM images. The in-plane spatial resolution of the optical microscope depends on the wavelength of the observed light. The idea to observe the radiation light from the materials with shorter wavelength in higher temperature was previously discussed to improve the resolution of infrared microscopy[140]. The present method is also similar to micro-thermography to map the radiation light from the sample[141, 142]. However, the mapping of emissivity has not been discussed, and the present method produces the emissivity mapping while the thermography aims at the temperature mapping. It is the novelty of the present method compared to the previous reports to distinguish materials based on the emissivities together with the improved resolution.

Figure III. 1. 3 shows the typical RM image observed at 1000 °C for the same grain as in Fig. III. 2. 1 (seen later). The surrounding area (dark, I) in the RM image emits weaker

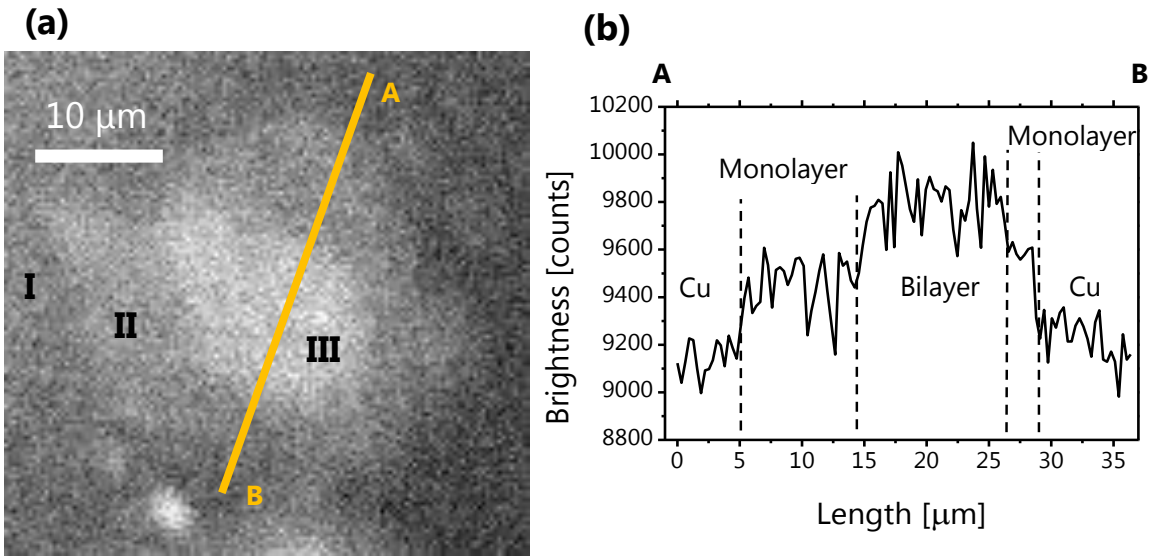

Figure III. 1. 3 (a) Radiation Microscopic image at T_s of 900 °C. The surrounding area (region I) corresponds to the Cu substrate. The single grain contains monolayer (region II) and bilayer (region III) graphene. The absolute brightness value is related to the amount of C atoms. (b) Line profile of absolute brightness value along with the orange line in (a). The dashed lines are eye guides to distinguish the monolayer and bilayer graphene from the Cu substrate.

radiation than other regions due to the low emissivity of Cu. The radiation intensity increases linearly to the number of stacked layers if the upper layer negligibly adsorbs the radiation light from the lower layer. The outer (gray, II) region looks darker than the center region (white, III), suggesting thinner graphene than the center region. Since the same grain was determined to be a graphene as discussed later for Fig. III. 2. 1, monolayer and bilayer graphenes were distinguished from each other. The structure of radiation map is clearly described by the line profile of the radiation intensity in Fig. III. 1. 3(b). The almost same heights of the two steps indicate that the surrounding area, the outer region, and the inner region corresponds to the Cu substrate, monolayer graphene, and bilayer graphene, respectively.

The in-plane spatial resolution of the system was calculated by the equation

$$d = 0.61\lambda/\text{N.A.} \tag{III. 1. 7}$$

where d, λ, and N.A. is the spatial resolution, the wavelength of observed light, and the numerical aperture of the system, respectively. The N.A. value of the system is calculated as N.A.=0.27, and thus the spatial resolution d is 1800 nm at $\lambda = 800$ nm. The width of the slope between the graphene layers in Fig. III. 1. 3 is related to the spatial resolution. It is evaluated between the positions with the step height of 10 and 90 %. The resulting resolution is less than 1 μm which is in agreement with a value of 1800 nm, while the size of pixels is 316 nm. Unfortunately, the spatial resolution is limited by the detection wavelength and not enough to observe the initial nucleation stage. However, the lateral growth of μm sized graphene grains can be clearly observed by the present method. These results indicate that the horizontal and vertical resolutions are sufficient to discuss the growth of large-area and monolayer graphene grains.

1.2.3 Temperature Dependence

The feature of the RM observation depends on the substrate temperature T_s since the radiation intensity depends on T_s. The RM images are shown to depend on T_s in Fig. III. 1. 4. The bright spots were confirmed to correspond to the grains of graphene as shown in section III. 2. The strong contrast between the graphene and Cu is observed at 750 °C in Fig. III. 1. 4(a). Figures III. 1. 4 (a-c) show that the contrast between the two materials decreases with temperature. At 670 °C in Fig. III. 1. 4(c), the surface morphology of Cu was observed simi-

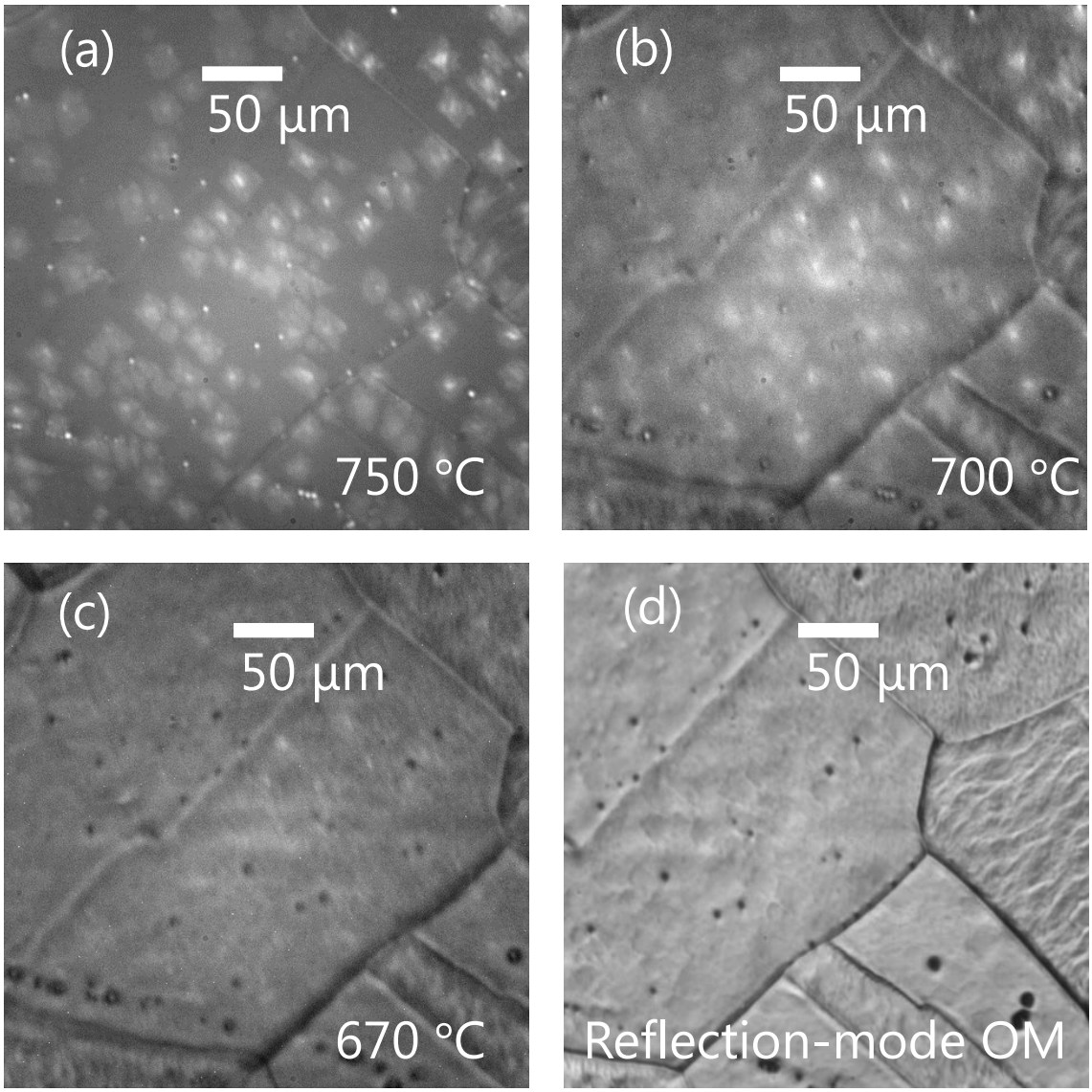

Figure III. 1. 4 (a)-(c) RM images observed at T_s of 750, 700, and 670 °C, respectively, with the exposure time of 10 s. Bright patches correspond to graphene grains. (d) Reflection-mode optical microscopic image of the same area as (a)-(c) with illumination light. While radiation of graphene is not observed, the reflection light from the surface illustrates the morphology of the Cu substrate.

lar to the refection-mode optical micrograph at 900 °C in Fig. III. 1. 4(d). Hence, I attributed the surface morphology observed at 670 °C to the stray light in the chamber. Both radiation and stray lights are comparable at 700 °C in Fig. III. 1. 4(b), indicating that the low limit of the temperature for the observation is approximately 700 °C. The stray light probably results from the reflection of the radiation light of the W ribbon in the chamber. It is speculated that the lower limit of the temperature for observation depends on the reflectance of the chamber wall. The growth at higher temperature can improve the radiation intensity suitably for the observation.

The radiation intensity increases with the temperature in Planck's law followed by the equation III. 1. 3. Therefore, the temperature was evaluated from the radiation intensity. The intensity of light was counted by the CMOS camera as the brightness value of the images. Figure III. 1. 5 shows the relation between the brightness values of RM images and the temperature observed by a pyrometer. Considering the equation III. 1. 3, the natural logarithm of the absolute brightness value is approximately linear to the reciprocal temperature. Figure III.

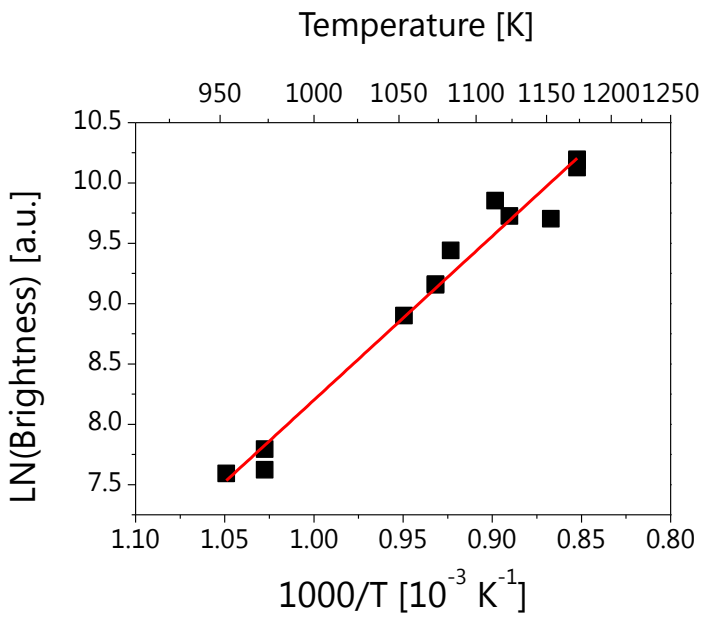

Figure III. 1. 5 Evolution of the brightness to temperature. X and Y axes stand for the reciprocal temperature and the natural logarithm of the absolute brightness value. The red line is the linear fitting of the natural logarithm of the absolute brightness values and reciprocal temperatures

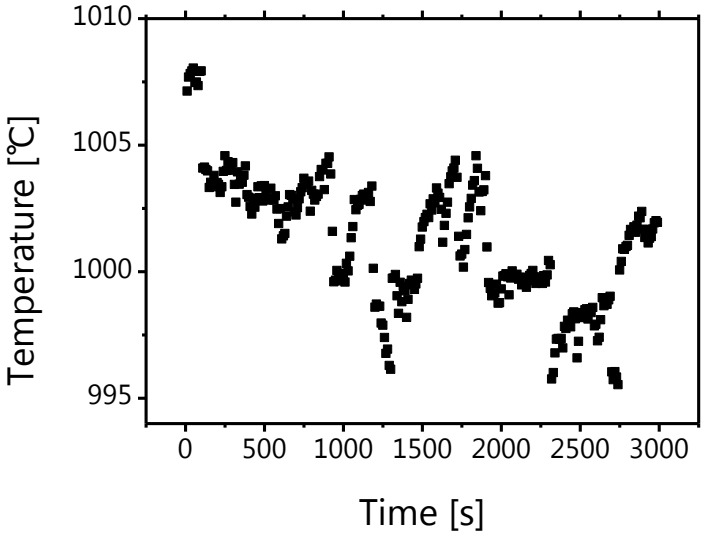

Figure III. 1. 6 Time evolution of T_s during growth of graphene calculated by Planck's law. The change of T_s is kept approximately 10 °C.

1. 6 shows the typical time evolution of the T_s which is evaluated from the average brightness during the real-time RM observation. Although the brightness value increases as graphene appeared on Cu substrate, the brightness values decreased. Taking account of the brightness value of graphene corresponding to the increase in the Cu temperature of 5 °, therefore, I estimated the decrease in temperature during the experiment to be 15 °C or so. The values suggested that the accuracy of the temperature in the experiment to be approximately 10 °C. These results indicate the strong relation between the RM and the temperature by Planck's law.

2 Comparison to "Post-Synthesis" Methods

Here, I discuss whether the RM can recognize graphene as well as other method on the basis of the comparison of the RM images, Raman mapping, and SEM images in Fig. III. 2. 1.

2.1 Growth Without Shrinkage

For “post-synthesis” characterizations, graphene was prepared on a Cu substrate without a shrinkage process. The real-time RM images were observed during the growth, and a typical one is shown in Fig. III. 2. 1(a) for the same grain as in Fig. III. 1. 3. Immediately after the shut-off of CH_4 supply, the T_s was subsequently decreased by reducing the direct current on a W ribbon. The temperature decreased below 600 °C within 1 s, judging from the reduced radiation from the sample observed by eye. After the sample was brought out from the chamber, Raman mapping and SEM observation were conducted on the same region as the RM images. Another sample was prepared in a similar way for the detailed Raman measurement after the transfer onto an SiO_2/Si substrate in Fig. III. 2. 2.

2.2 Scanning Electron Microscopy

The SEM image of the sample is shown in Fig. III. 2. 1(b). The size of pixel and the magnification was 50 nm and ×1000, respectively. Comparing the SEM images to the previous reports[78], the graphene grains in SEM images consist of thinner outer region and thicker inner region of graphene.

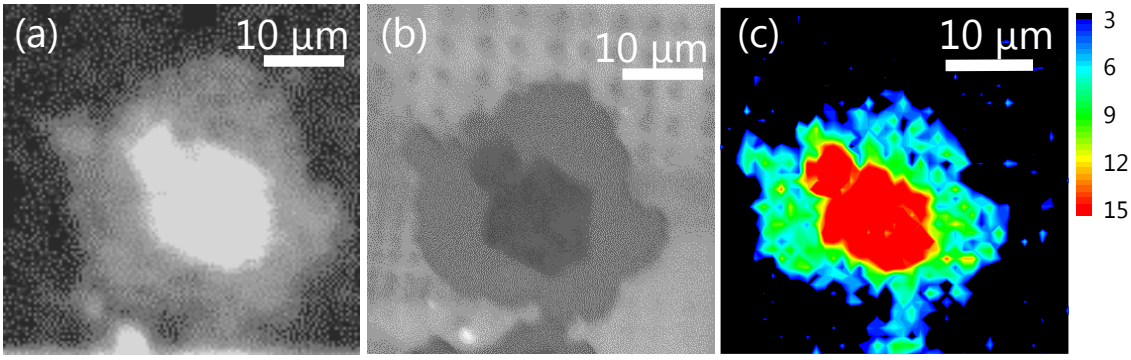

Figure III. 2. 1 Comparison of (a) RM image, (b) SEM image, and (c) Raman G band intensity map for the same area of graphene grown on Cu substrate. The CH_4 flow rate, T_s, and growth time was 2 sccm, 1000 °C, and 2200 s, respectively

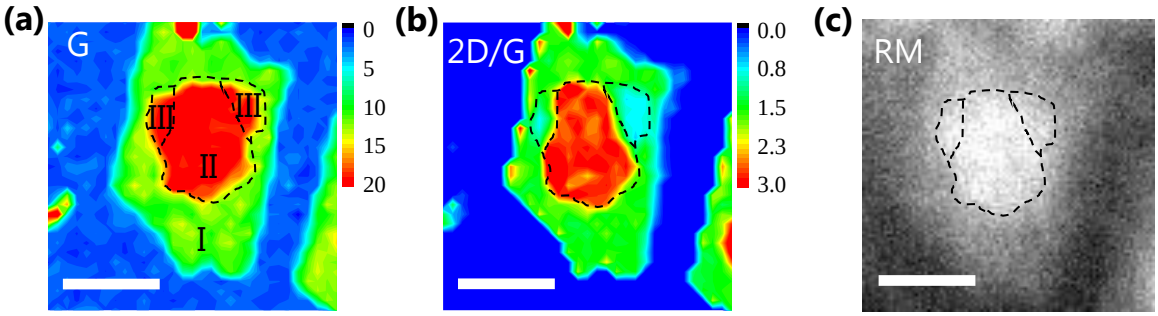

Figure III. 2. 2 Raman map of transferred graphene compared to RM image. (a) Raman G band intensity map. Dashed line is eye guide. The intensity shows the region I corresponds to monolayer graphene while the region II and III correspond to bilayer graphene. (b) Raman intensity ratio map of I_{2D}/I_G. Dashed line is same as that in (a). I_{2D}/I_G ratio shows the number of graphene layers and its stacking structure as written in the main text. (c) Radiation Microscopic image of same grain as (a, b). Dashed line is same as that in (a). The brightness of RM shows the thinner and thicker graphene in the region I and II-III, respectively. The scale bar is 10 μm.

2.3 Raman Mapping

2.3.1 On Cu Substrate

Raman mapping measurement was conducted on the region in Fig. III. 2. 1(c) with the horizontal step of 1 μm. The shape of observed graphene grain looks similar to that in the SEM image although the spatial resolution is low. The G band intensity mapping, reflecting the amount of sp^2 C rings, indicates that the inner and outer region is thicker and thinner graphene, respectively. The observed grain shape and thickness distribution are consistent with that in the SEM observation.

2.3.2 On SiO_2/Si substrate

The G band mapping in Fig. III. 2. 2(a) shows the same tendency as the inner and outer region corresponding to thicker and thinner graphene, respectively. In addition, the intensity ratio map of I_{2D}/I_G showed the outer region has the I_{2D}/I_G ratio of 1.5, indicating that the region I corresponds to monolayer graphene[36–38]. The region II and III are thus recognized as bilayer graphene judging from the G band intensity mapping. The intensity ratio of region II is 0.8, suggesting the AB stacked bilayer graphene. The region III suggests the turbostratic bilayer graphene judging from the intensity ration of 3.0[127, 128]. The clarification of the

reason for different stacking orientation should be required in the future.

2.4 Radiation Microscopy

Comparing with the “post-synthesis” characteristics, the present method can observe graphene clearly. The shape of graphene grains in the RM images are similar to that of Raman mapping and SEM image in Fig. III. 2. 1. The bright and gray regions in the RM images correspond to the thicker and thinner regions of graphene confirmed by the Raman mapping and SEM observations. Comparing with the detailed Raman mapping, the monolayer and bilayer graphene can be distinguished in the RM images. The stacking orientation, on the other hand, cannot be distinguishable in RM as shown in Fig. III. 2. 2. The RM was probed to observe the real-time growth of graphene on Cu substrates with the horizontal and vertical resolution of 1800 nm and monolayer, respectively.

Part IV
Discussion of Growth Mechanism of Graphene in Chemical Vapor Deposition

In this part, I explain the real-time RM observation and analysis of the CVD growth of graphene. First, the real-time RM images observed during the growth and shrinkage of graphene were processed to subtract the background. I explain the qualitative analysis of graphene growth based on the processed RM images. Subsequently, I show the extraction of quantitative data from the RM images and the analysis of those depending on the growth parameters. Finally, I discuss the mechanism and the parameter optimization of the CVD growth of graphene.

1 Qualitative Analysis

Here, I show the ways to subtract the backgrounds from the images to prepare for the discussion. First, the effects of the fixed parameters of the growth and shrinkage of graphene are explained. Subsequently. the general features and the effects of the surface orientation of the Cu substrates are discussed in a qualitative manner based on the resulting RM images.

1.1 Image Processing

Since the background intensity included in the RM images prevents the quantitative analysis, the background is subtracted at the first step of the analysis. The subtraction and quantitative analysis of the RM images were conducted with “Image J”, a free software for the image manipulation[143]. Since more than 1,000 RM images were often observed in one experiment, the home-made “Macro” function of “Image J” was applied to subtract backgrounds and to deduce the quantitative information.

The observed RM images include the background lights due to a stray light and the radiation from the Cu substrates. To eliminate the background, I subtracted the image at 0 s of the observation from all the images and added a constant at each pixels to avoid the negative

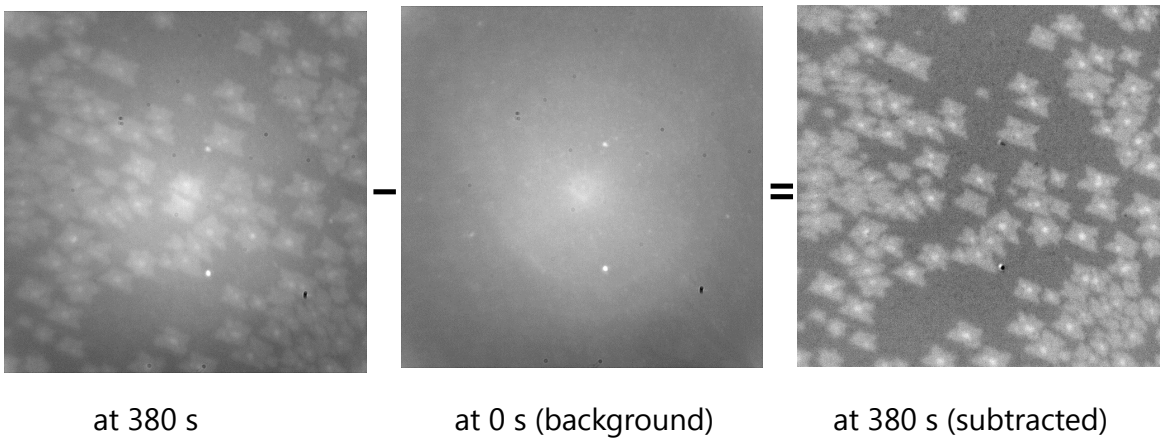

Figure IV. 1. 1 Subtraction of background at 0 s from RM image at 380 s. Note: the thermal drift of the sample does not affect the background subtraction. The size of images is 326 μm^2.

value. The Gauss blur (σ=2 pixels) was then applied to the images to enable "Image J" to detect the shape of graphene grains. Finally, the contrast and brightness of the images were adjusted by "auto contrast" in "Photoshop CS6 Extended" from Adobe Systems.

1.2 Fixed Parameters

Among a lot of parameters of the CVD growth of graphene, the T_s, CH_4 flow rate, and O_2 partial pressure are chosen to be changed. The total pressure strongly depends on the larger Ar flow rate than the other gases in the system while the T_s was affected by the total pressure. The Ar flow rate and the total pressure were kept at 1000 sccm and 2700 Pa, respectively, to maintain the T_s during the experiments. The value of the total pressure was considered enough to suppress the Cu sublimation which affect the growth of graphene[77, 144, 145].

The flow rate ratio of H_2 and CH_4 has been considered to be important as the growth parameter[74]. However, purified H_2 was reported not to affect the growth due to the negligible dissociative adsorption probability of H_2 on Cu[44]. The H_2 flow rate and the purity of gases affect the growth features in the previous reports[45, 74] and during the optimization of the parameters for the present study, suggesting the effect of the impurities on the CVD growth of graphene. For simplicity, I kept the H_2 flow rate kept at 100 sccm according to these reports.

1.3 Qualitative Information

As an example, I show the RM images observed during the growth of graphene at 985 °C with the CH_4 flow rate and O_2 partial pressure of 5 sccm and 0.09 Pa, respectively, in Fig. IV. 1. 2. The images were observed with the exposure time and colour depth of 500 ms and 16 bits, respectively. The observed area was 326×326 μm^2 corresponding to 1024×1024 pixels, so that the size of pixels is 316 ×316 nm^2. Generally, the nucleation of graphene grains starts at first as shown in Fig. IV. 1. 2(a, b). The soot like particles [146] often appear on the substrates for example as two particles in the center of images, as shown in Fig. IV. 1. 2(c). The nucleation of graphene sometimes occurs near such the apparent nucleation centers. The grain boundaries and the polishing scratches of Cu foils are also candidates for the nucleation centers. The nucleation of graphene can also occur on the basal plane of the Cu grains randomly. The area of graphene grains increases under a constant CH_4 flow as shown in Fig. IV. 1. 2(a-f). The growth is not dominated by the diffusion of the growth precursors judging from the compact shapes of graphene grains, which is discussed in section IV. 2.4. Instead, the growth precursors can diffuse on the surface with repeated attachment and detachment to reach the energetically stable edges during the growth of graphene.

After the shut-off of CH_4 supply at 380 s, the growth of graphene stopped and the shrinkage begun as shown in Fig. IV. 1. 2(f-i). Unlike the growth, the shape of graphene was not maintained during the shrinkage. The grains were etched randomly as shown also in Fig. IV. 2. 10 in section IV. 2.3. The etching feature suggests that the reverse reactions of growth and shrinkage of graphene do not occur because of the depletion of the precursors after the shut-off of CH_4. Finally, the graphene disappeared on the substrate completely as shown in Fig. IV. 1. 2(i).

The morphology of grown graphene on a polycrystalline Cu foil depends on the surface orientation of Cu substrate[75, 145]. The tetragonal, rectangular, and hexagonal graphene grains are reported to grow on Cu (100), (110), and (111) substrates, respectively, as shown in Fig. IV. 1. 3. In the present study, I found that some of the graphene grains form 2-fold rotational symmetry, and the long axes of the graphene grains in Fig. IV. 1. 3 align with a

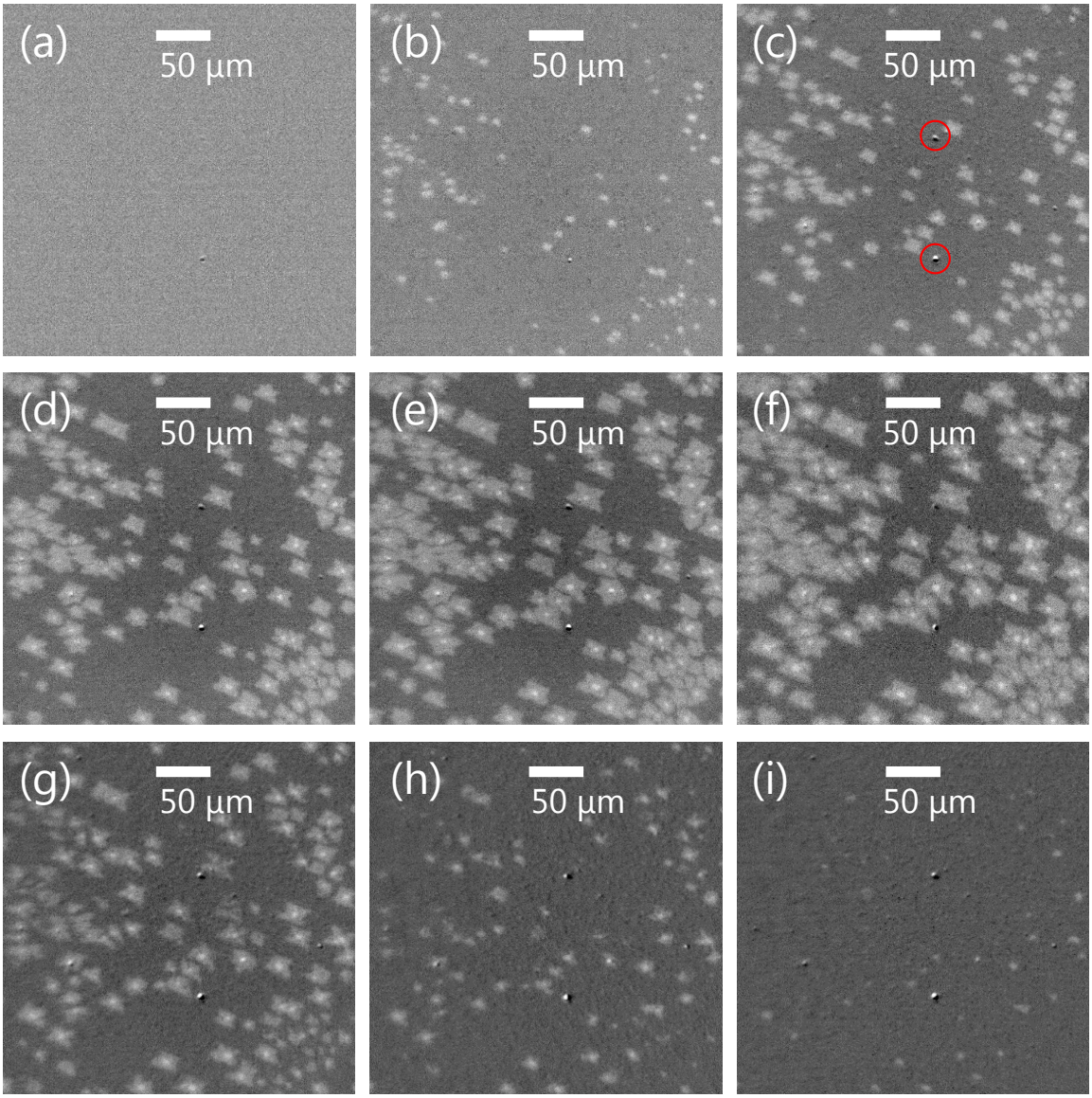

Figure IV. 1. 2 Observed RM images at 0, 80, 160, 240, 320, 380, 500, 600, and 700 s during experiment at 985 °C. (a-f) Graphene was grown on Cu substrate with CH_4 flow rate and O_2 partial pressure of 5 sccm and 0.09 Pa, respectively. (f-i) Graphene disappeared after the shut off of CH_4. In the center of the images, two soot like particles are observed as shown with red circles in (c). The shape of particles is highlighted due to the slight thermal drift of the sample.

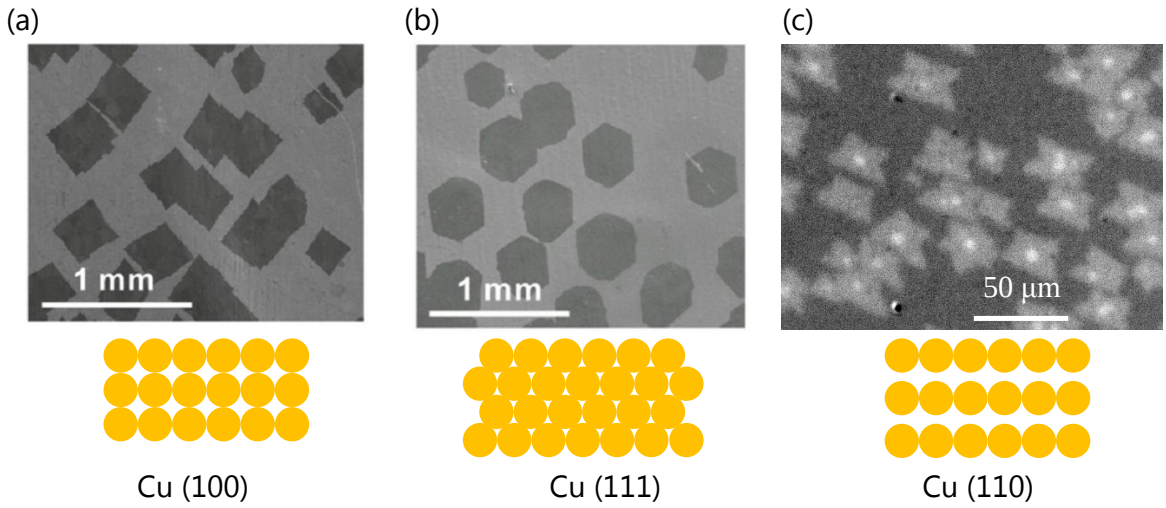

Figure IV. 1. 3 (a, b) Reported SEM images of graphene on polycrystalline Cu foil. (c) Typical RM image of graphene on Cu substrate in the present study. The tetragonal, hexagonal, and rectangular shapes of graphene grains reflect the surface orientation of Cu (100), (111), and (110) surfaces, respectively[75]. The surface orientations of Cu in (a, b) were determined by electron back scattering diffraction measurement. Reprinted (in part and adapted) with permission from Yan, Z. *et al*. Toward the Synthesis of Wafer-Scale Single-Crystal Graphene on Copper Foils. *ACS Nano* **6**, 9110-9117 (2012). Copyright 2012 American Chemical Society.

certain direction in the same grain of the polycrystalline Cu foil. This result suggested the growth of graphene on the Cu substrate was affected by the (110) surface orientation of the Cu foils. The surface orientation of Cu prefers chemically stable (111) at high temperature close to the melting point while other orientations appear at lower temperature[147, 148]. The surface orientation of Cu of (110) in the present study is thus consistent with the relatively low temperatures of 900-1000 °C.

The inner regions of the graphene grains in Fig. IV. 1. 3 are hexagonal with sharp edges, which is more clearly observed in Fig. III. 2. 1. The 2nd layer of bilayer graphene was reported to grow between the Cu substrate and the 1st layer of graphene[149, 150] from CH_4 while the 2nd layer grew on the graphene/gas phase interface from ethanol[151]. As shown in Fig. IV. 1. 4, the 2nd layer of graphene in the present study grew between the 1st layer and the Cu substrate from CH_4. Considering the structure of bilayer graphene, these hexagonal shapes and sharp edges were attributed to the 2nd layer of graphene. The 2nd

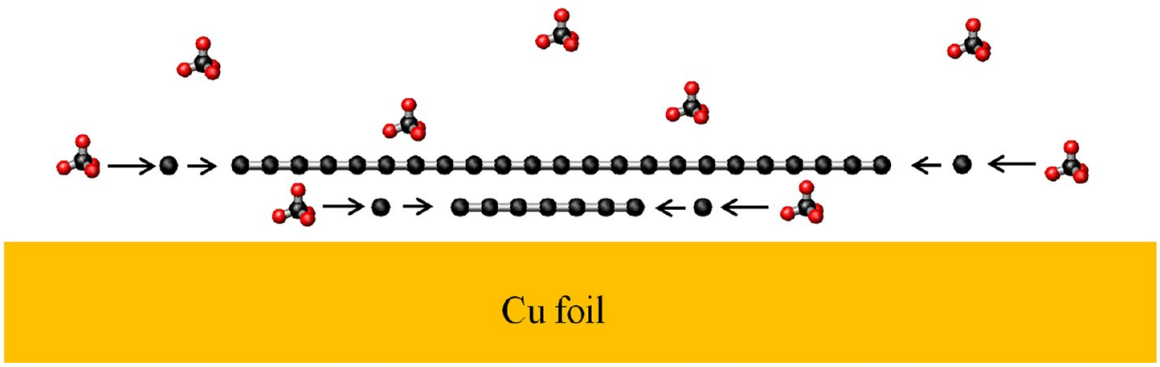

Figure IV. 1. 4 Growth mechanism of 1st and 2nd layer graphene from CH_4[149]. After the growth of 1st layer graphene, the 2nd layer graphene grows between the 1st layer and Cu substrate. Reprinted (in part and adapted) with permission from Li, Q. *et al*. Growth of adlayer graphene on Cu studied by carbon isotope labeling. *Nano Lett*. **13**, 486-90 (2013). Copyright 2015 American Chemical Society.

layer of graphene form 6-fold symmetry while the 1st layer of graphene was grown 2-fold, and both of layers were grown on the Cu substrate. Therefore, the 2nd layer of graphene is considered to grow ignoring the 2-fold Cu substrate and interacting with the 6-fold lattice of the 1st layer of graphene. It should be noted that the stacking orientation of the 2nd layer of graphene to the 1st layer is not uniform in graphene grains as discussed in the Raman analysis in section IV. 2.3. If further investigation reveals the growth mechanism of bernal or turbostratic stacking of bilayer graphene, they result in the control of the properties of graphene *via* stacking orientations.[5, 9, 33, 34].

2 Quantitative Analysis

Here, I analyze the nucleation, growth and shrinkage of graphene depending on the growth parameters according to the extracted values. The speed of the nucleation of graphene is discussed based on the saturation nucleation density (n_{sat}). The analyses of the growth and shrinkage rely on the rates of the increasing and decreasing of the graphene area. I discuss the mechanism of the CVD growth of graphene based on the dependence of the growth feature on the temperature, CH_4 flow rate, and the O_2 partial pressure.

2.1 Data Extraction

I counted the numbers of nuclei in the images by hand and eye to discuss the nucleation density. I did not use "Image J" for counting because it is difficult for "image J" to distinguish graphene islands from the background noises in the initial nucleation stage of graphene. The area of single graphene grain was estimated by "image J". The "Threshold" was applied on the images with auto "Moments" threshold algorithm to binarize the images. After picking the selected region up from the whole image to focus on a certain grain, applying the "analyze particle" function of "Image J" to the selected region of the binarized RM images provided the area of singe graphene grain. The quantitative analyses of these data are explained in the following section.

2.1.1 Nucleation Density

From the RM images, I extracted the saturation nucleation density (n_{sat}) which provides the information of the nucleation of graphene. Figure IV. 2. 1 shows the typical time evolution of the number of nuclei of graphene, indicating that the nucleation density saturates to n_{sat}.

Before the nucleation occurs, the density of the growth precursors increases with the decomposition of the source gas. Subsequently, the density of the growth precursors reaches the critical value for nucleation, and the nucleation starts. The growth precursors are consumed by the nucleation and decrease until the precursor density becomes less than the critical value for nucleation. In this stage, the nucleation rate decreases and the nucleation density finally saturates to n_{sat}.

The n_{sat} is not related only to a nucleation rate itself but also to the growth rate of graphene. The production of the growth precursors occurs only on the bare Cu surface since the dissociative adsorption probability of CH_4 is low at this temperature[152]. The area in which graphene can nucleate (*i.e.* the area not covered by graphene) decreases with graphene coverage increasing. The n_{sat} thus decreases as the growth rate increases and/or the nucleation rate decrease. Since it is difficult to evaluate the nucleation rate directly, I discuss the nucleation by n_{sat} in the present study.

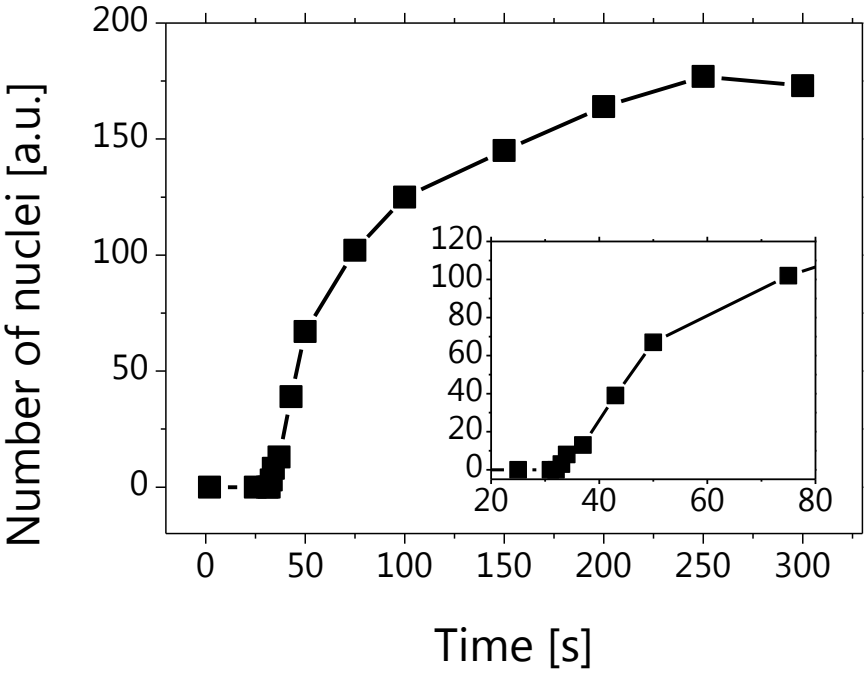

Figure IV. 2. 1 Time evolution of number of graphene nuclei for images in Fig. IV. 1. 2. The number of nuclei looks saturating to a certain value. (inset) Closed-up figure to focus on the initial nucleation stage.

2.1.2 Growth and Shrinkage Rates

I analyzed the growth and shrinkage rates from the slope of the square root of grain area with respect to the elapsed time. Figure IV. 2. 2 shows the typical time evolution of the area of a single graphene grain. The area increases after the introduction of CH_4 gas, and the shrinkage starts immediately after the shut off of CH_4 at 380 s. As the images were observed in every second with the exposure time of 500 ms, the time resolution of the plot was 1 s. Furthermore, the real-time observation can provide the series of the images from one trial of the growth. In the previous reports, on the other hand, the growth of graphene was discussed by “post-synthesis” characterization similarly to section III. 2. Therefore, the time resolution was limited to 1 min or so, as shown in Fig. IV. 2. 3. Moreover, analysis of the growth depending on the various growth parameters requires a number of experiments. Recently, the real-time observation of the growth of graphene was reported with environmental SEM technique as shown in Fig. IV. 2. 4[112, 122]. While the environmental SEM can work

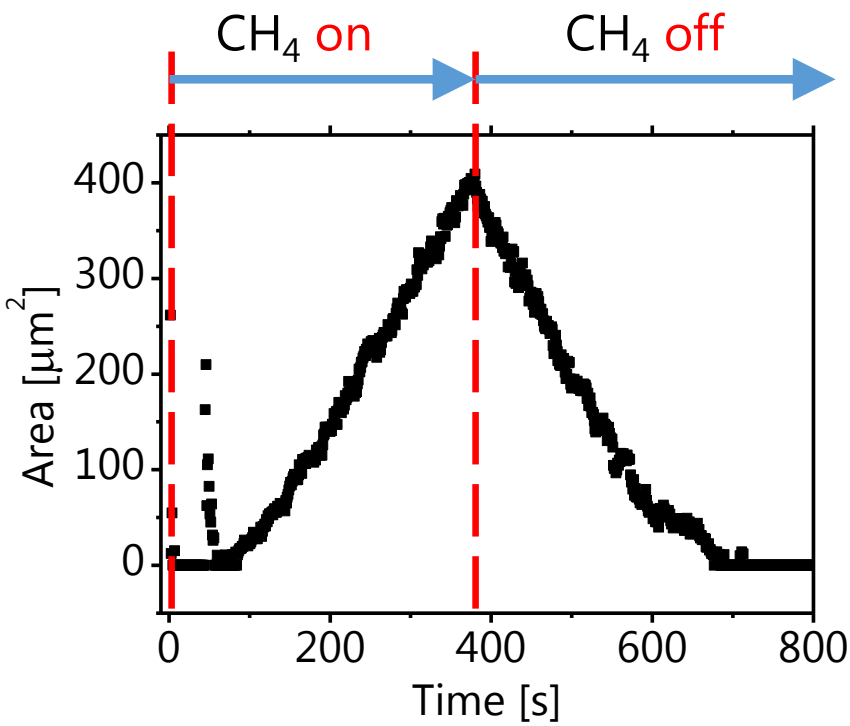

Figure IV. 2. 2 Typical time evolution of area of single graphene grain for images in Fig. IV. 1. 2. The observations are performed in every second, and thus the time resolution is 1 s. After the shut-off of CH_4 supply at 380 s, the graphene starts the shrinkage. The noises in the early stage suggested that "Image J" failed to measure the area.

under the total pressure of several thousands Pa, the time resolution of the observation is still limited to be several tens of seconds. The improved time resolution resulting in few number of experiments is one of the most important achievements of the present technique.

The time evolution of the grain area is parabolic in the initial stage of growth as shown in Fig. IV. 2. 2. To confirm this, the square root of area was plotted in Fig. IV. 2. 5. From 0 to 200 s, the square root of area looks linear to the elapsed time. I explain the mechanism in the following. For simplicity, I consider the graphene grain as a disk and the growth occurs only at the edges under the constant concentration of the C precursors. In this case, the growth rate dA/dt is proportional to the circumference $2\pi r$, where A, r, and t is the area and the radius of the graphene grain, and the elapsed time, respectively. The equation

$$\frac{dA}{dt} = k(T) \times 2\pi r \times C, \tag{IV. 2. 1}$$

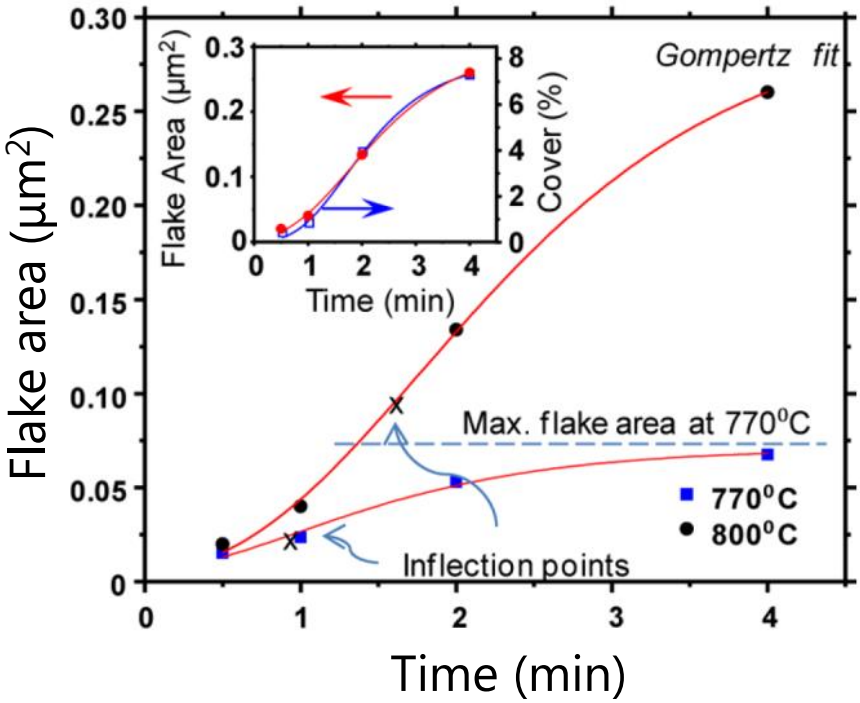

Figure IV. 2. 3 Typical time evolution of grain area of graphene in the previous report[78]. The time resolution is 1 min in the order of magnitude. Reprinted (in part and adapted) with permission from Celebi, K. *et al*. Evolutionary kinetics of graphene formation on copper. *Nano lett*. **13**, 96774 (2013). Copyright 2013 American Chemical Society.

was thus deduced where $k(T)$, T, and C is the rate constant, the temperature, and the precursor density, respectively. Solving the differential equation, the relation

$$A(t) = at^2 \tag{IV. 2. 2}$$

was deduced since $A(0)$ is zero where a is a constant. Therefore, the square root of graphene area is linear to the elapsed time under such mechanism.

Figure IV. 2. 5 shows, on the other hand, the growth rate of graphene is suppressed from the parabolic dependence. I discuss the reason as follows. The area producing the precursors decreases as graphene covers the surfaces. In this hypothesis, I ignored the catalytic activity of graphene to produce the precursors [83] due to the low dissociative adsorption probability of CH_4 on graphite at high temperature (>700 K)[152]. The increase rate of the coverage of

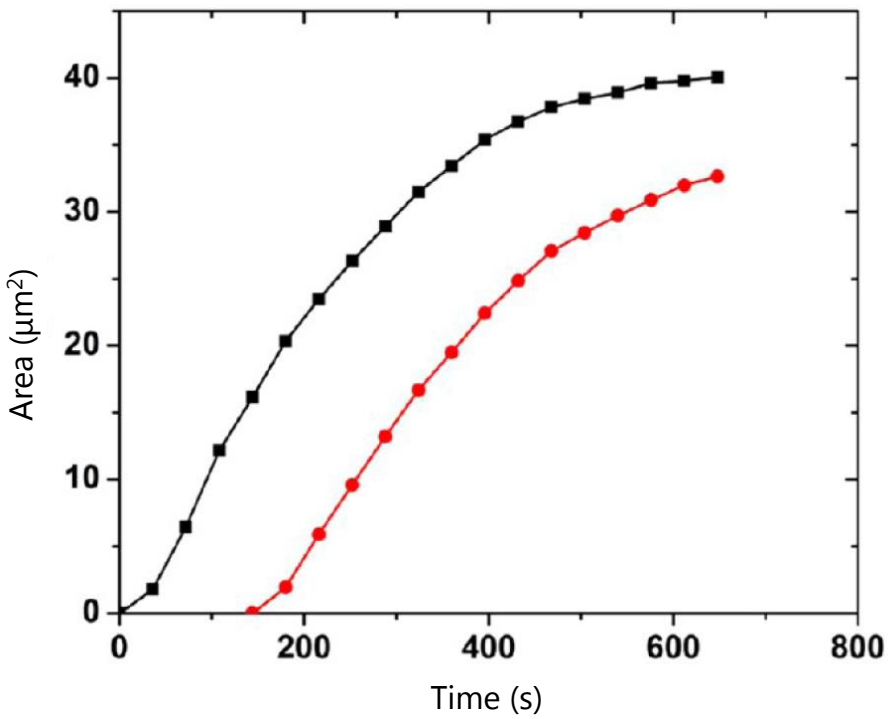

Figure IV. 2. 4 Time evolution of grain area of graphene in by environmental SEM[122]. The time resolution is in the order of the several tens of seconds. The increase in the grain area looks parabolic in the initial stage and suppressed similarly to the present study. Reprinted (in part and adapted) with permission from Wang, Z.-J. *et al*. Direct Observation of Graphene Growth and Associated Copper Substrate Dynamics by in Situ Scanning Electron Microscopy. *ACS nano*. *Article ASAP* (2015). Copyright 2015 American Chemical Society.

graphene (θ_{gra}) is proportional to $1 - \theta_{\mathrm{gra}}$ (corresponding to bare Cu surface) as written here

$$\frac{d\theta_{\mathrm{gra}}}{dt} = k(T) \times (1 - \theta_{\mathrm{gra}}). \tag{IV. 2. 3}$$

Considering the relation

$$\frac{d(1 - \theta_{\mathrm{gra}})}{dt} = -k(T) \times (1 - \theta_{\mathrm{gra}}) \tag{IV. 2. 4}$$

and the facts that θ_{gra} is 0 and 1 at t=0 s and $t \to \infty$, respectively,

$$\theta_{gra} = 1 - \exp(-\lambda t) \tag{IV. 2. 5}$$

is deduced where λ is a constant of the integration, and the area decreases from the parabolic curve.

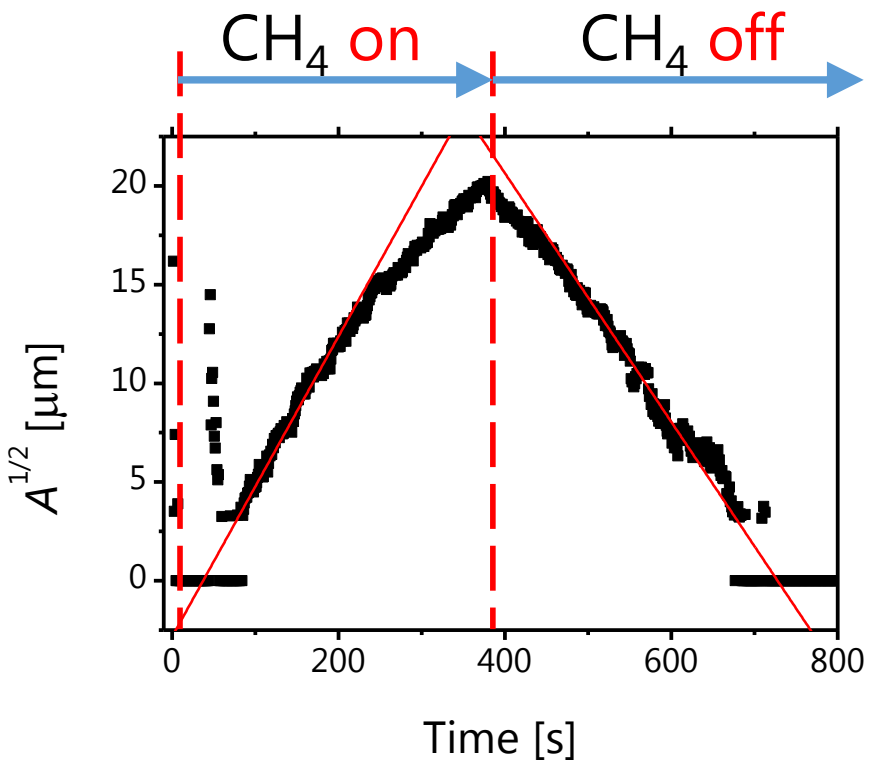

Figure IV. 2. 5 Typical time evolution of square root of graphene area for images in Fig. IV. 1. 2. The area is measured for the selected region in the RM images to show the time evolution for a single graphene grain. Red lines correspond to the linear fitting.

As discussed above, the constant density of the growth precursors causes the parabolic dependence of the grain areas on *t*. If the precursor production is suppressed as graphene covered the surface, on the other hand, the grain areas decrease from the parabolic curve. In the case of the initial stage of graphene growth, the low graphene coverage results in the growth dominated by the attachment of the precursors and the parabolic dependence of graphene area to the growth time. As graphene covers the surface and the graphene grains get closer, the suppressed precursor production starts to decrease the growth rate from the parabolic dependence. Under these situations, I extracted the growth rate for the initial stage of graphene growth to discuss the intrinsic growth rate in the present study as shown in the red lines in Fig. IV. 2. 5.

2.2 Temperature Dependence

Temperature analysis provides the information of the mechanism of chemical reactions. I analyzed the series of experiments performed on the same substrate as shown in Fig. IV. 1. 2 for various T_s. The nucleation, growth, and shrinkage of graphene were enhanced at higher temperature, suggesting their elementary steps have high activation energies.

2.2.1 Nucleation Density

The temperature dependence of the nucleation density is plotted as a function of the growth time in Fig. IV. 2. 6. The saturation nucleation density n_{sat} generally increases with the T_s from 905 to 985 °C as shown in Fig. IV. 2. 7. This tendency is opposite to the previous reports[76, 78]. I explain the reason in the following.

In physical vapor deposition, it is usual for the nucleation densities to decrease as the T_s increases. This is because the re-evaporation of the growth precursors is enhanced at higher temperatures. If the precursors are produced in the vapor phase, for example in plasma en-

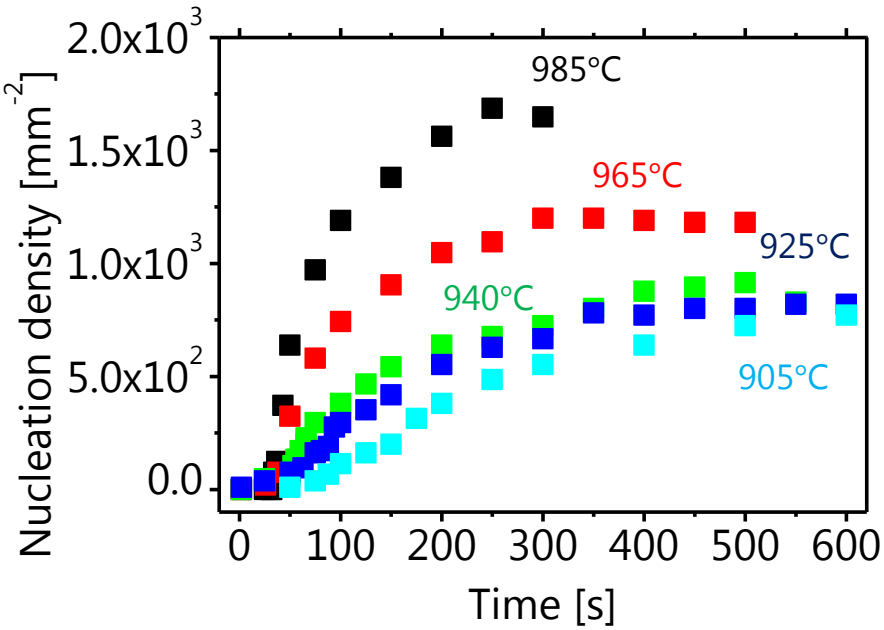

Figure IV. 2. 6 Nucleation density of graphene as functions of time depending on T_s for the same substrate as shown in Fig. IV. 1. 2.

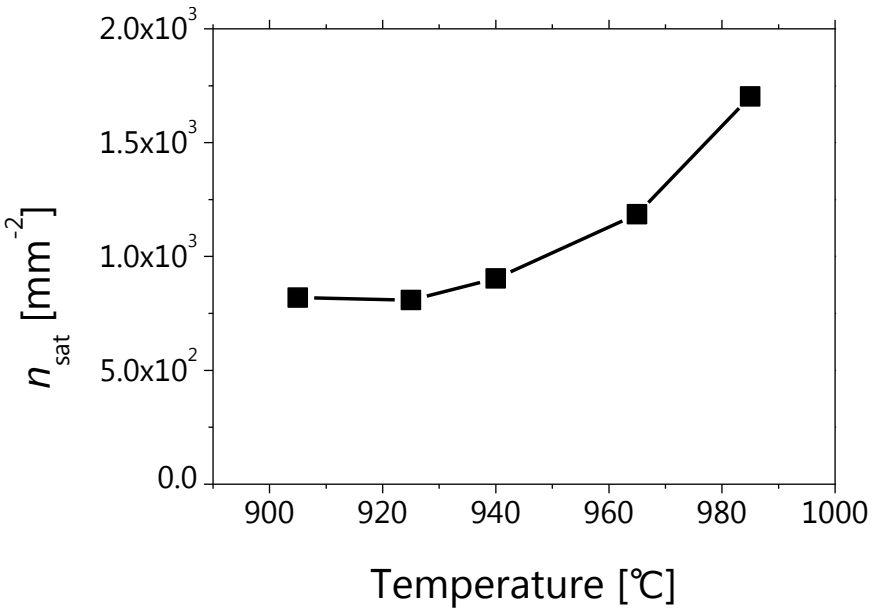

Figure IV. 2. 7 Saturation nucleation density (n_{sat}) as a function of T_s for the same substrate as shown in Fig. IV. 1. 2. The n_{sat} increases with T_s while saturates with low T_s.

hanced CVD, the enhanced re-evaporation of the precursors results in the reduced nucleation and growth[153]. In thermal CVD, however, the processes such as the decomposition of source gas and the nucleation of the precursors requires a finite activation energy such as 1 eV or so as discussed in the experiment and theory[76, 78, 115, 154], resulting in the high nucleation density in high temperatures[155]. The enhancement of the nucleation is superior to the re-evaporation of the growth precursors at higher temperature in the present study. Therefore, these chemical reactions are accelerated at higher temperature as previously pointed out for the graphene CVD[78].

The present study based on the real-time RM observation could not be compared directly to other studies. I suppose the reasons of the opposite tendency in the previous reports [76, 78] as follows: The T_s in the present study was set from 905 to 985 °C, and that of the previous reports was close to 1085 °C which is the melting point of Cu. Under such high temperature conditions, Cu sublimes revolving the growth precursors, in which the nucleation can be suppressed[77, 145]. As discussed in section IV. 2.1.1, the competition between the nucleation and the growth rates determines n_{sat}. It can be considered that the nucleation and

growth rate decrease with T_s resulting in the opposite tendency in the present results to the previous reports. The saturation of n_{sat} with T_s as shown in Fig. IV. 2. 7 can also be attributed to this competition.

2.2.2 Growth and Shrinkage Rate

Similarly to the nucleation, the growth and shrinkage rates increase at higher temperature as described in Figs. IV. 2. 8 and IV. 2. 9. The activation energies of the growth and shrinkage of graphene were evaluated from the Arrhenius plots in Fig. IV. 2. 9 to discuss the mechanism. The activation energy is determined to be 2.7 eV in this temperature region with the slight suppression at higher temperature. The elementary steps are described in Fig. I. 1. 5 to consider the growth mechanism. The activation energy for the incorporation of graphene precursors produced by CH_4 was reported to be 2.6 eV on Cu substrates[76]. On Ru substrate, the value of 2.0 eV was reported[86]. On the other hand, the activation energies such as the adsorption of CH_4 and the diffusion of the precursors (0.5-1.0 eV) are much lower than the value in the present study[78, 115, 156]. The decomposition of CH_4 becomes 1.7-

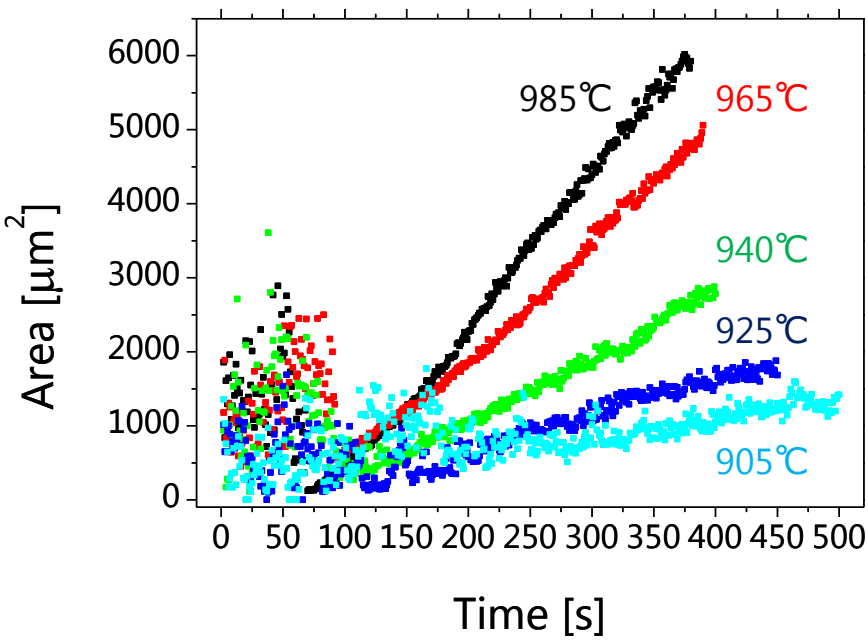

Figure IV. 2. 8 Typical time evolution of grain area of graphene depending on T_s for the same substrate as shown in Fig. IV. 1. 2.

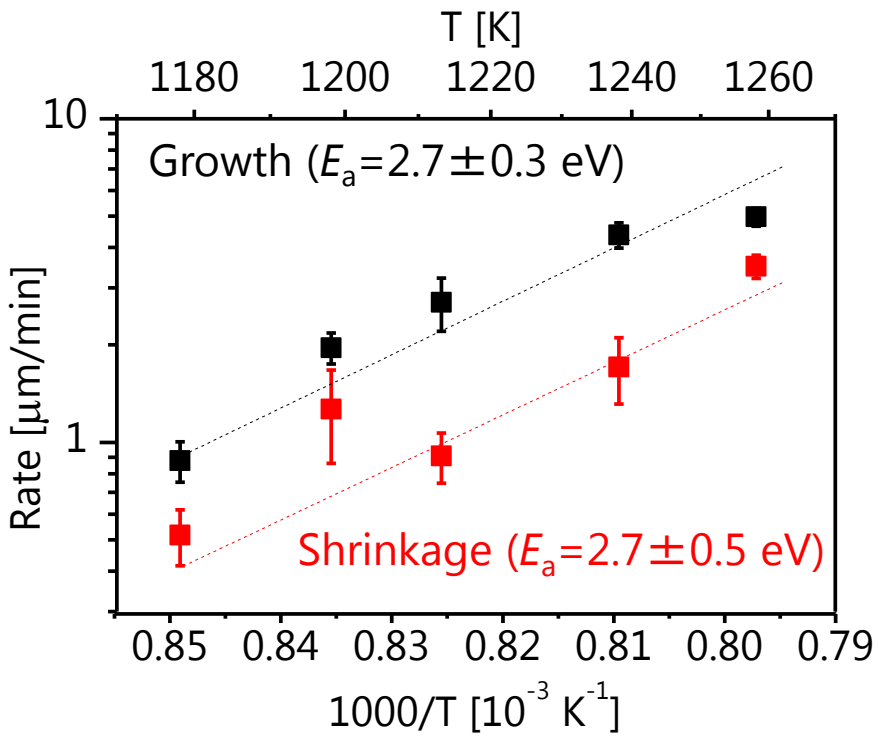

Figure IV. 2. 9 Temperature dependence of growth (black) and shrinkage (red) rates of graphene for the same substrate as shown in Fig. IV. 1. 2. The broken lines correspond to the fitting to the Arrhenius equation. Both activation energies for the growth and shrinkage of graphene are 2.7 eV judging from the slopes of the fittings.

1.9 eV[115, 154], however, the value is still less than that in the present study. Therefore, I conclude the rate-limiting step of the growth is the incorporation of the precursors to graphene lattice judging from the comparison between the values of each activation energy.

The shrinkage rate of graphene also increases at higher temperature, and its activation energy is 2.7 eV from the Arrhenius plots in Fig. IV. 2. 9. The value of the activation energy for the shrinkage of graphene is close to that of the growth. However, the activation energies of growth and shrinkage should be different by the enthalpy of the reaction if the growth and shrinkage are the simple reversible reactions each other. I supposed that the mechanisms of the growth and shrinkage are not same. Namely, the precursors decomposed from CH_4 and detached from the graphene lattice are possibly different. However, I do not have enough information to conclude whether the elementary steps of the growth and shrinkage obey the same reaction or not. Further real-time observation will reveal the mechanism of shrinkage

compared with the growth.

It is important for the growth of the large-area single-crystal graphene to suppress the n_{sat}. Unfortunately, the size of graphene is limited to several tens of μm presumably due to the high nucleation rate in the present set-up. Although the conditions should be optimized further, the saturation of n_{sat} of graphene grains at a certain T_s and the decrease in the growth rate with T_s are observed. The fast growth is suitable with the same grain size for the productivity. The T_s should be optimized taking the nucleation and growth rates into account.

2.3 Methane Flow Rate

I also analyzed the effect of CH_4 flow rate on the nucleation and the growths of graphene. Figure IV. 2. 10 shows the RM images during the experiment with the CH_4 flow rate of 2 sccm. The RM images for the same substrate as shown in Fig. IV. 2. 10 were used in the flow rate analysis. Both n_{sat} and the growth rate were extracted from the RM images in the similar way to the previous analysis. The enhanced production of the growth precursors increased the n_{sat} and the growth rate with the CH_4 flow rate.

2.3.1 Nucleation Density

Figures IV. 2. 11 and IV. 2. 12 shows the evolution of n_{sat} and the growth rate to the CH_4 flow rate at T_s of 1005, 975, and 945 °C. The n_{sat} increases with the CH_4 flow rate while the growth rate saturates at that of 10 sccm. Both of the nucleation rate and the growth rate affect the n_{sat} as discussed before in section IV. 2.1.1. The increased n_{sat} suggests the increased nucleation rate. It can be considered that the precursor density increases in the initial nucleation stage with the CH_4 flow rate.

2.3.2 Growth rate

The growth rate increases with the flow rate as shown in Fig. IV. 2. 12, which is attributed to the increase in the production of growth precursors. With the CH_4 flow rate of 10 sccm, on the other hand, the increase in the growth rate was only slight. The density of the growth precursors in the stage of growth was thus considered to saturate to a finite value. I explain the tendency of the growth rate different from that of the nucleation rate as follows. As the CH_4 gas is supplied, the precursor density increases from zero to the critical value for

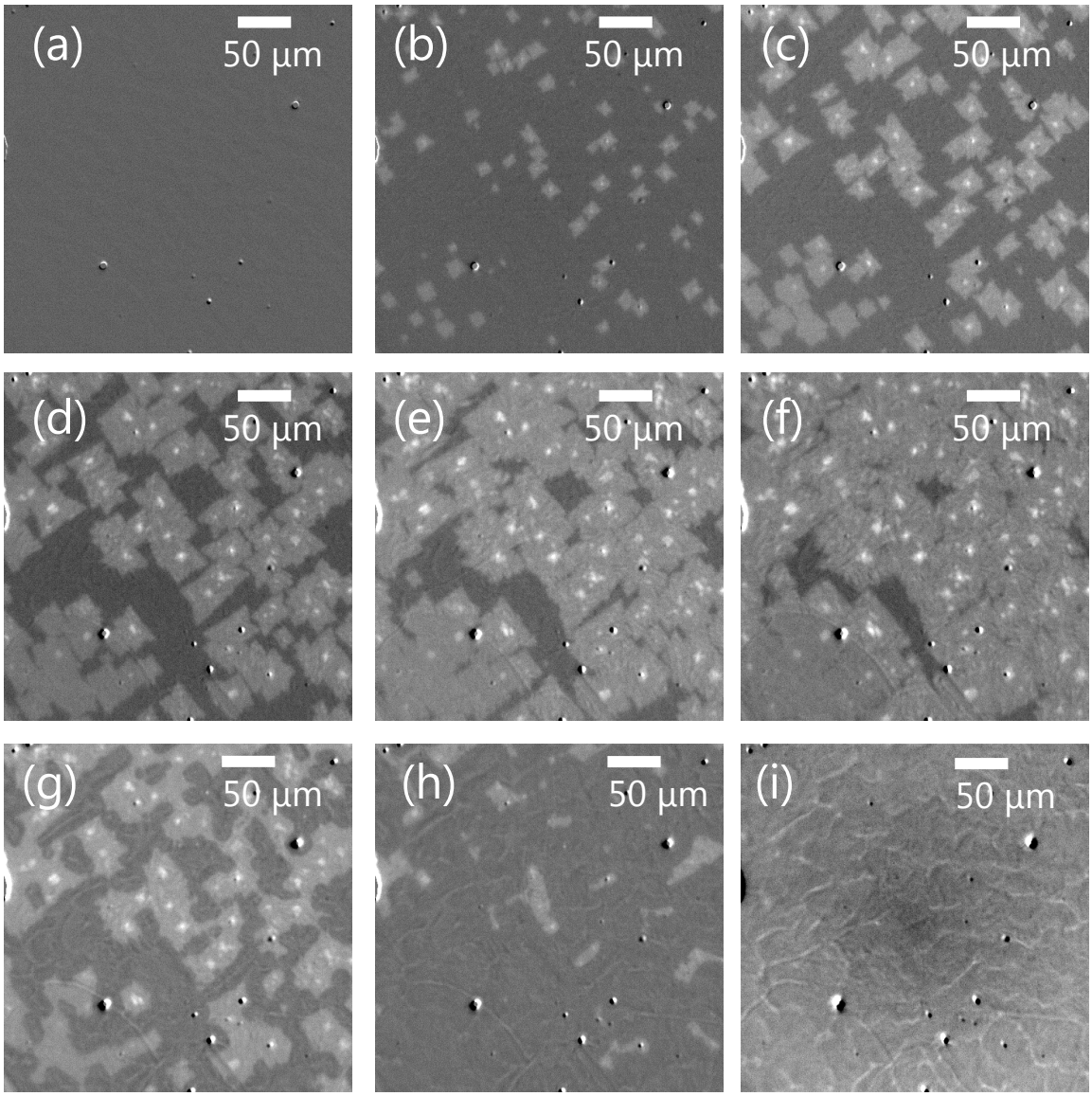

Figure IV. 2. 10 Snapshots at 0, 360, 720, 1080, 1440, 1800, 3000, 4000, and 5000 s from RM images during experiments at 1005 °C. The O_2 partial pressure was estimated to be 0.07 Pa. (a-f) Graphene was grown on Cu substrate with CH_4 flow rate of 2 sccm. (g-i) Graphene disappeared after the shut off of CH_4.

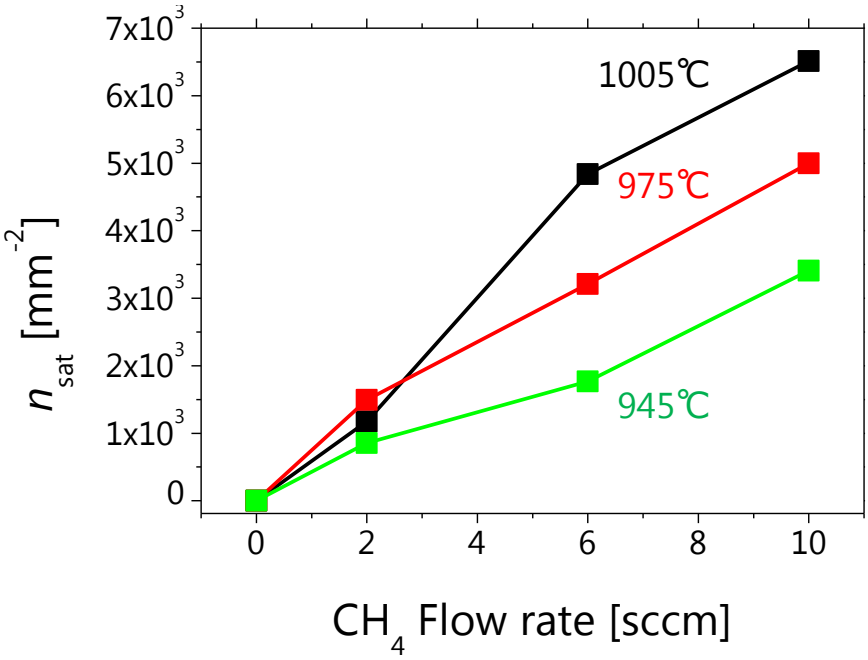

Figure IV. 2. 11 Saturation nucleation density of graphene as a function of CH_4 flow rate, depending on T_s. The n_{sat} increases with CH_4 flow rate.

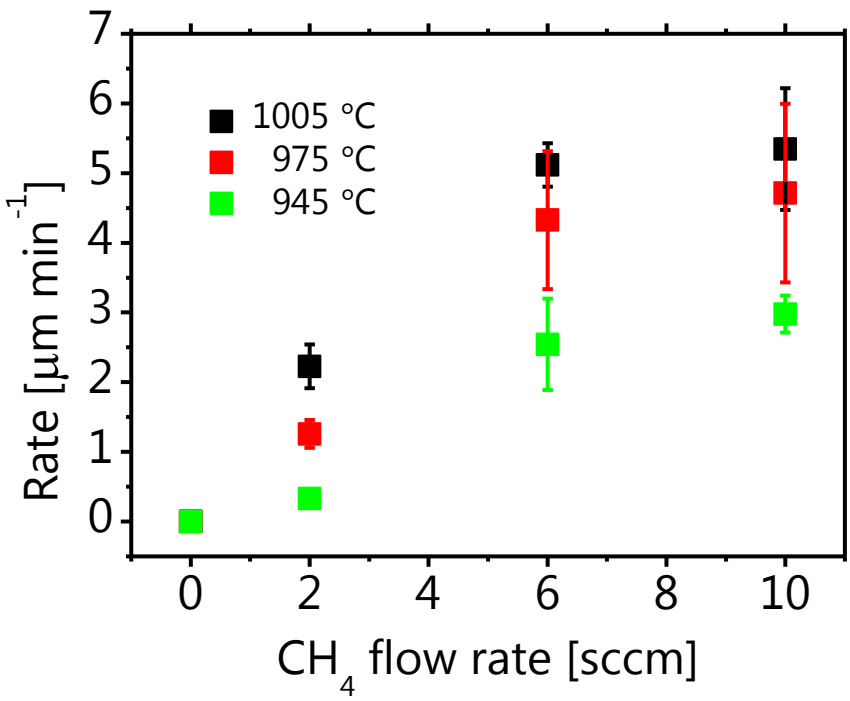

Figure IV. 2. 12 Growth rate of graphene as a function of CH_4 flow rates, depending on T_s. The rates increase with CH_4 flow rate while saturate with CH_4 flow rate of 10 sccm.

the nucleation. The nucleation consume the precursors to decrease the precursor density to the value for the steady growth of graphene[76]. The nucleation and growth rate can be dominated by the critical density for the nucleation and the constant density of the precursors for the steady growth of graphene, respectively. Therefore, it can be considered that the nucleation is enhanced by the increased density of the precursors while the constant density of the precursors for the steady growth of graphene is saturated with high CH_4 flow rate.

The large-area single-crystal graphene is grown under the condition to suppress the nucleation. The effect of the CH_4 flow rate suggests that nucleation rate and the growth rate increases monotonically and saturates to a certain value, respectively. If the precursor density becomes less than the critical value for the nucleation, on the other hand, the graphene grains will not appear. Therefore, the CH_4 flow rate should be lowered to the critical value for the nucleation.

2.3.3 Coalescence

Figure IV. 1. 2 shows the images observed to analyze the growth of single grain graphenes. The growth was thus canceled before the coalescence of graphene grains occurred. However, there is a demand to grow a continuous graphene film for the devices such as transparent conducting films, for example. I also discuss the coalescence of graphene grains on the basis of the RM images on the same substrate as Fig. IV. 2. 10. Figure IV. 2. 13 focuses on the coalescence of graphene grains. As the graphene grows, the edges of graphene grains are getting closer to each other with keeping its shape as shown in Fig. IV. 2. 13(a-c). After they touches, the channels between grains are smoothly connected and disappear to complete the coalescence.

2.4 Oxygen Partial Pressure

Recently, the O atoms on the Cu surfaces were found to play important roles in the CVD growth of graphene[81, 112, 116, 117]. I conducted the growth and shrinkage of graphene under the condition for the CVD growth of graphene and observed their features depending on the O_2 partial pressure. I show the real-time response of the growth features to the decrease in O_2 partial pressure and the growth features in the unchanged O_2 partial pressure.

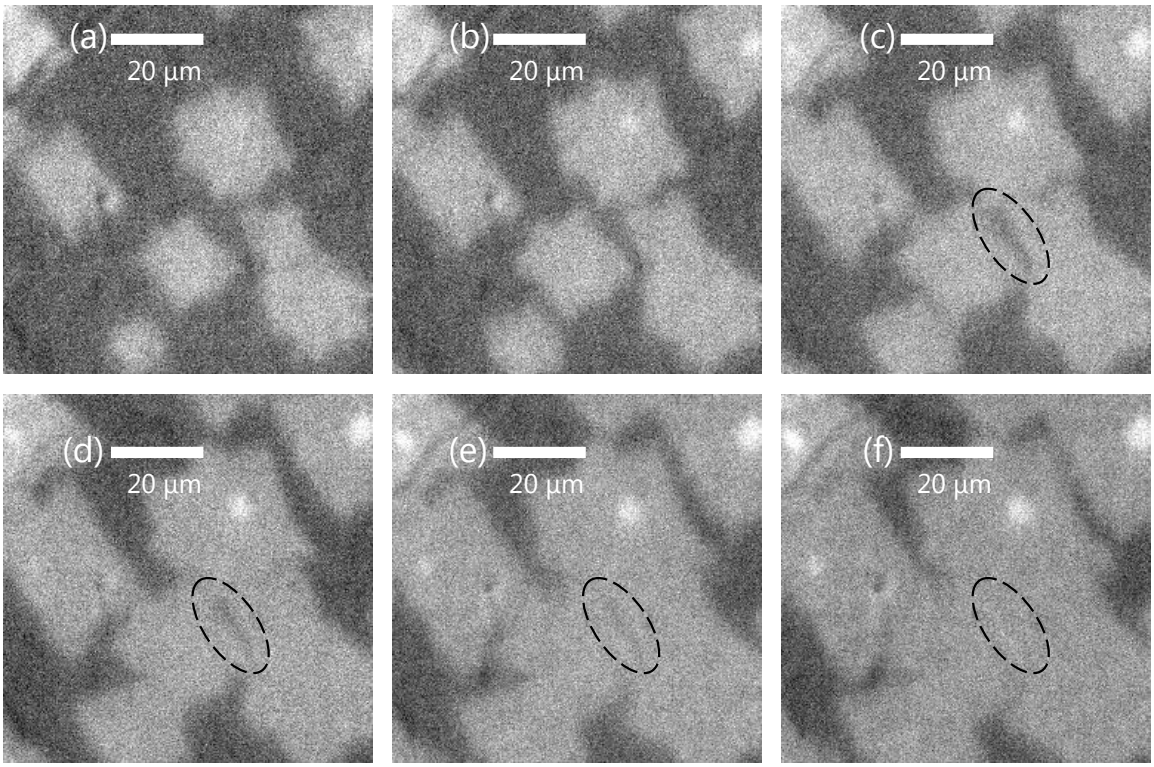

Figure IV. 2. 13 Observed RM images at 500, 600, 700, 800, 900, and 1000 s showing coalescence of graphene grains. The CH_4 flow rate and T_s was 2 sccm and 1005 °C, respectively. Before the coalescence, the shape of graphene was kept. As the graphene grains coalesced, the channel between grains (dashed lines for eye guides in the images) disappeared.

2.4.1 Real-time Response

In order to observe the real-time response of the growth to the change of the conditions, the O_2 partial pressure was changed from 0.09 to 0.04 Pa during the growth of graphene, as shown in Fig. IV. 2. 14. The T_s was kept at 950 °C. The O_2 partial pressure was decreased at 15 min [Fig. IV. 2. 15 (d)], and the CH_4 flow rate was shut-off at 25 min [Fig. IV. 2. 15 (f)]. The real-time RM images were shown in Fig. IV. 2. 15. I extracted the nucleation density and the area of grains in the same way as other images. Figure IV. 2. 16 shows the time evolution of the nucleation density during the experiment. As discussed in the section IV. 2.1.1, the nucleation density saturates to a certain value within 15 min. Immediately after the decrease in the O_2 partial pressure, the nucleation density increased and started the re-saturation to the

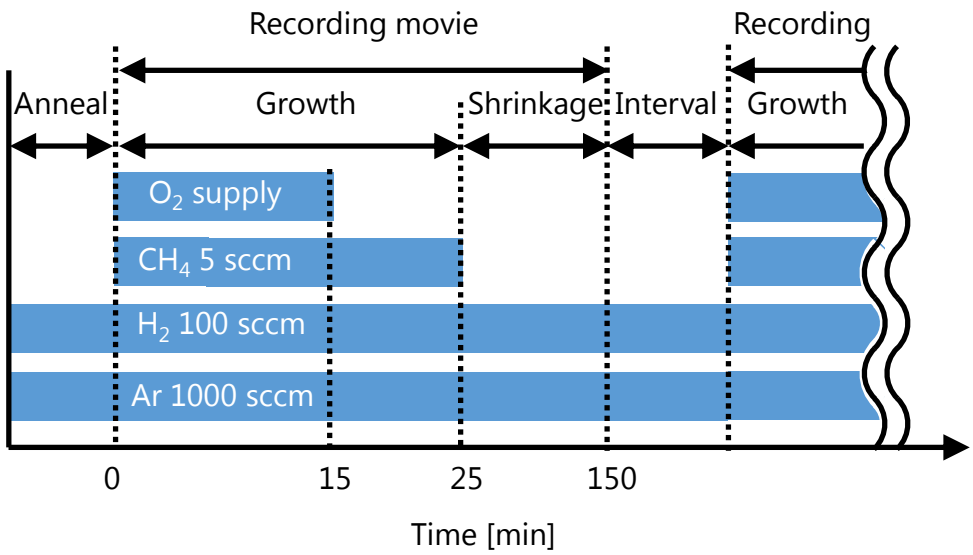

Figure IV. 2. 14 Schematic illustration of sequence with changing O_2 partial pressure. The supply of O_2 was shut-off at the time of 15 min while that of CH_4 at 25 min. The supply of other gases were kept during the whole experiment. The T_s was kept at 950 °C.

increased value. The O atoms are thus considered to adsorb on the Cu surfaces to suppress the nucleation of graphene presumably due to the formation of volatile CO and CO_2 molecules with the precursors. The chemical reactions in the vapor phase is considered negligible since the temperature of gases is low due to the cold-wall set-up in the present study.

Figure IV. 2. 17 shows the area of a single grain of graphene as a function of the growth time. The rates are evaluated from the square root of area as discussed in section IV. 2.1.2. The decrease in the O_2 partial pressure accelerated the growth rate from 2.03 to 2.81 μm/min, indicating that the O atoms suppress the lateral growth of graphene. Therefore, the growth precursors are considered to be consumed by the adsorbed O_2. It should be noted that the quick responses of the nucleation and growth of graphene are observed in real-time by RM for the first time.

2.4.2 Effect of O_2 Partial Pressure

In addition to the real-time response to the change of the O_2 partial pressure, graphene was grown under various O_2 partial pressure:0.04, 0.07, 0.09, and 0.12 Pa. The O_2 partial pressure was kept at the desired value during the growth and shrinkage. Figure IV. 2. 18(a) shows the

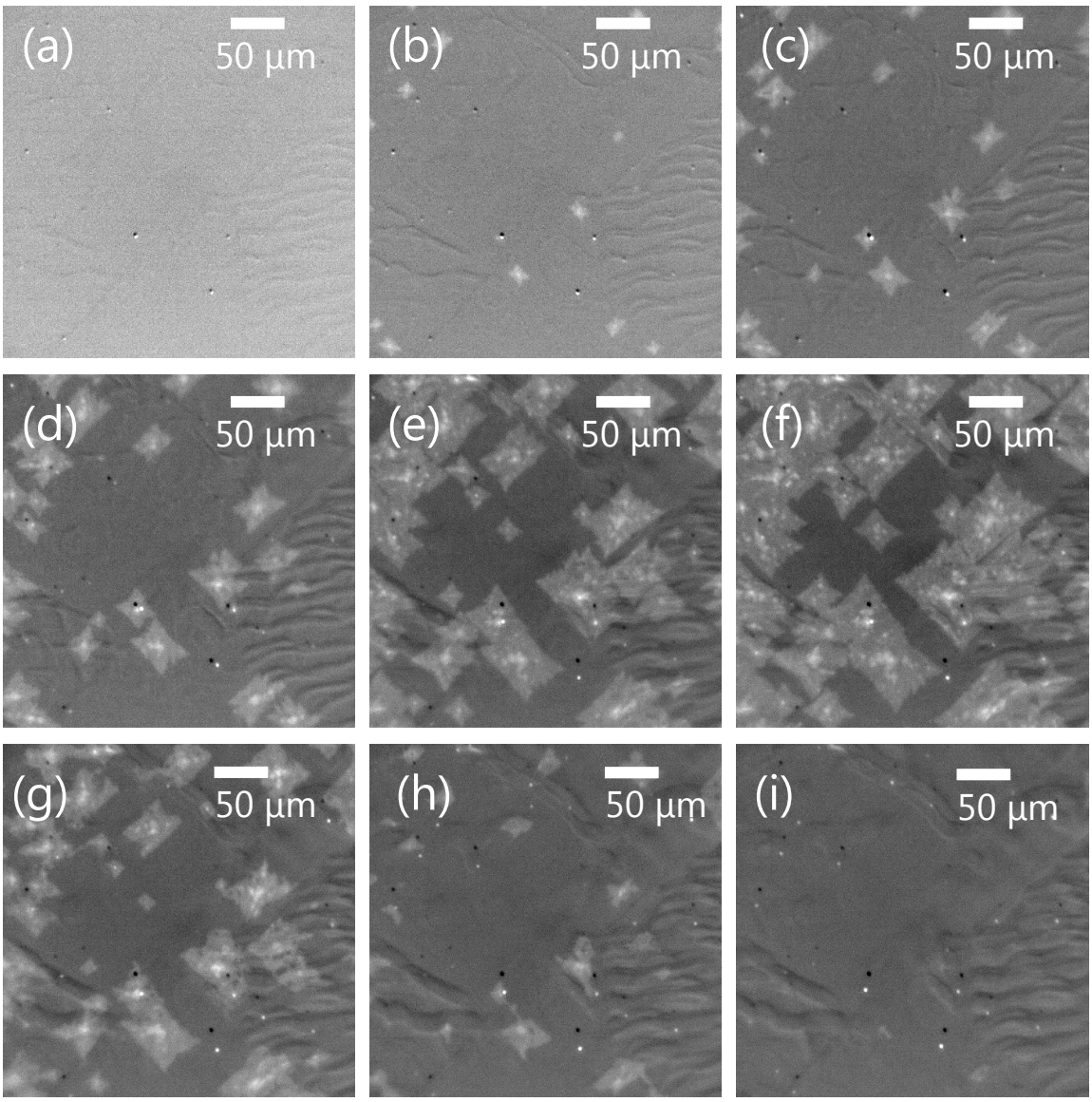

Figure IV. 2. 15 Observed RM images at 0, 5, 10, 15, 20, 25, 60, 90, and 120 min with changing O_2 partial pressure[157]. The supply of O_2 was shut-off at 15 min (d) while that of CH_4 at 25 min (f).

typical RM image of graphene taken at the growth time of 7 min. The O_2 partial pressure and the CH_4 flow rate was 0.09 Pa and 5 sccm, respectively. Graphene did not nucleate at the partial pressure of 0.12 Pa at least within 10 min presumably due to the depletion of growth precursors by O_2 as discussed before. The CH_4 flow rate increased to 10 sccm compensated for the depletion of the growth precursors, and graphene started the nucleation and growth as

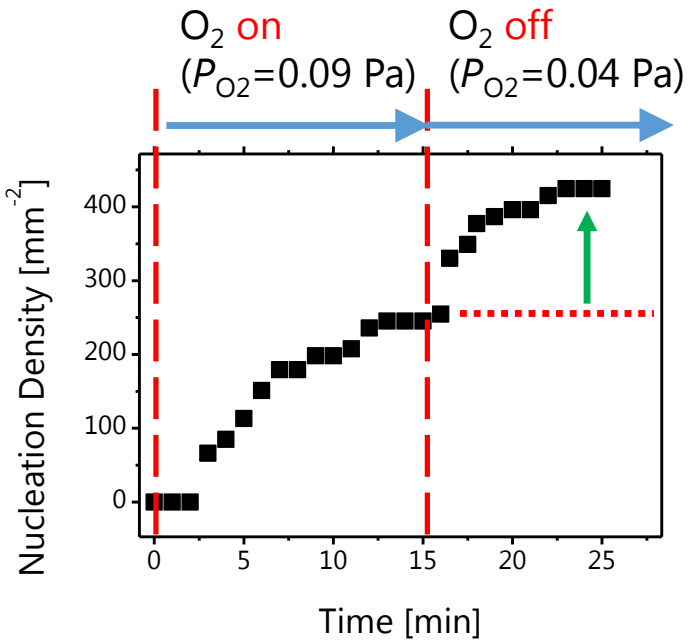

Figure IV. 2. 16 Time evolution of number of graphene nuclei[157]. The number increased just after the shut-off of O_2. The T_s and CH_4 flow rate was kept at 950 °C and 5 sccm, respectively. Copyright: 2015, The Japan Society of Applied Physics.

shown in Fig. IV. 2. 18. The shapes of graphene grains, on the other hand, are dendritic in Fig. IV. 2. 18, suggesting that the diffusion of the growth precursors is the rate-limiting step of the growth of graphene. It has been reported that the surface O_2 atoms enhance the detachment of H atoms from graphene edges to reduce the activation energy of the incorporation of the precursors[81]. In this case, the diffusion limited growth gives rise to the dendritic shape of grown graphene grains, consistent with the present result. Further investigation is required to reveal the activation energies of the present studies to confirm the reproducibility of the change of the rate-limiting steps.

Although the effect of the surface O_2 was discussed in the previous report[81], the quantitative analysis of the effect of O_2 on the CVD growth of graphene has not been studied intensively. The n_{sat}, growth rate, and shrinkage rate are plotted in Fig. IV. 2. 19 as a function of the O_2 partial pressure extracted from the RM images on the same Cu substrate as shown in Fig. IV. 2. 16. The n_{sat} monotonically decreases as the O_2 partial pressure increases, indicating the depletion of the growth precursors of graphene by O_2. The growth

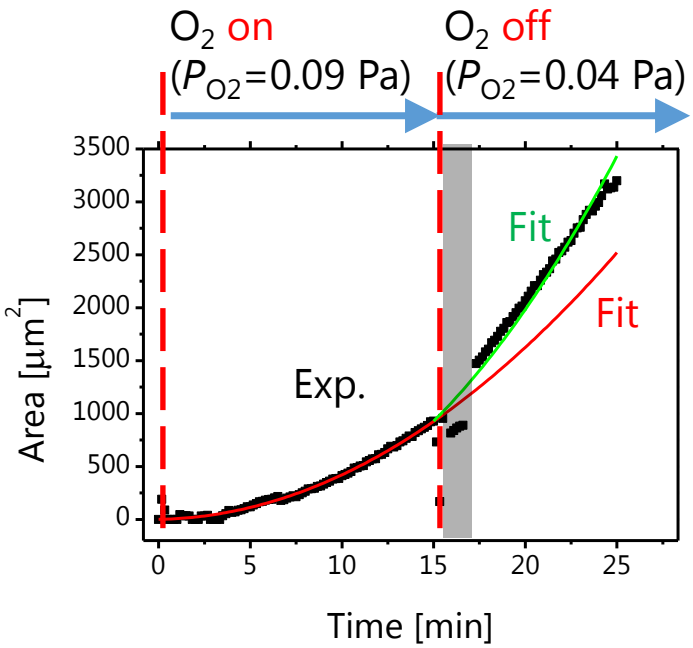

Figure IV. 2. 17 Time evolution of area of graphene nuclei[157]. The area increased just after the shut-off of O_2 at 15 min. The T_s and CH_4 flow rate was kept at 950 °C and 5 sccm, respectively. The red and green lines correspond to the fitting curve for the growth rate of 2.03 and 2.81 μm/min, respectively. Data in the gray region (period between 15 and 17 min) were affected by mechanical vibration from the valve operation to shut off O_2. Copyright: 2015, The Japan Society of Applied Physics.

rate of graphene, on the other hand, reaches a maximum value at the O_2 partial pressure of 0.07 Pa. The decrease in the growth rate in higher O_2 partial pressure region can be explained by the depletion of the precursors due to the reaction with O_2. The increase in the growth rate with the O_2 partial pressure from 0.04 to 0.07 Pa is consistent with the previous report in which the surface O_2 enhanced the detachment of H atom from graphene edge to fascinate the lateral growth of graphene[81]. The growth rate at the O_2 partial pressure of 0.07 Pa thus reaches a maximum owing to the competition of the enhanced lateral growth and the depletion of the growth precursors.

The shrinkage rate increases from 0.26 to 0.55 μm/min with the O_2 partial pressure as shown in Fig. IV. 2. 19. It was reported that the shift of the precursor density on the surface gave rise to the shrinkage of graphene. As an example of this mechanism, the shrinkage rate of 0.02-0.2 μm/min was reported on Ru at 700-800 °C for O_2 partial pressure below

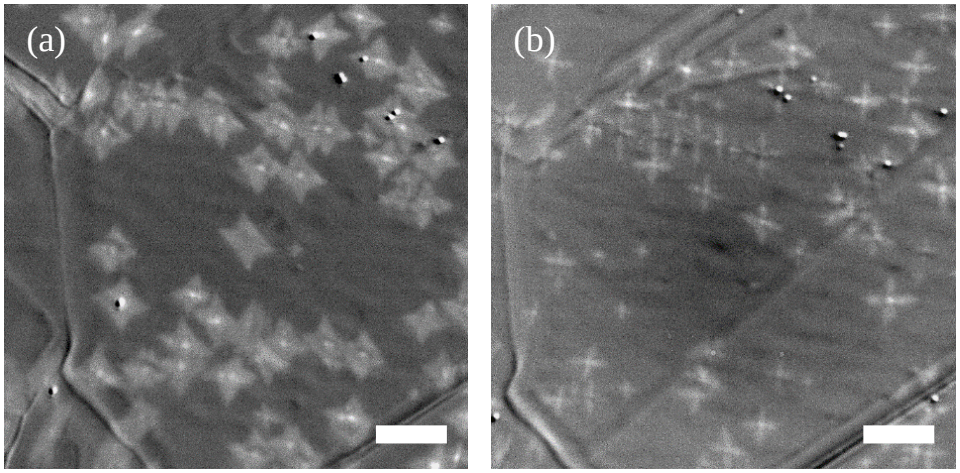

Figure IV. 2. 18 Growth of graphene with O_2 partial pressure of (a) 0.09 and (b) 0.12 Pa[157]. (a) The compact shapes of graphene grains are observed under CH_4 flow rate of 5 sccm. (b) The dendritic shapes of graphene grains are grown under CH_4 flow rate of 10 sccm. The T_s was kept at 950 °C. Scale bar 50 μm. Copyright: 2015, The Japan Society of Applied Physics.

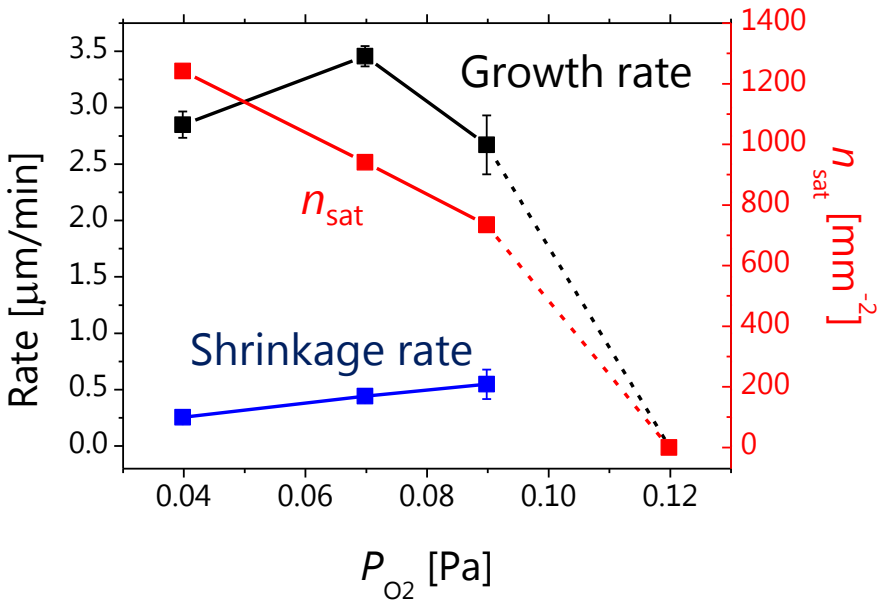

Figure IV. 2. 19 Saturation nucleation density, growth rate, and shrinkage rate as a function of O_2 partial pressure[157]. The T_s and CH_4 flow rate was kept at 950 °C and 5 sccm, respectively. The shrinkage rate (left axis) and n_{sat} (right axis) increase and decrease with O_2 partial pressure, respectively, while growth rate (left axis) reaches a maximum with O_2 partial pressure of 0.07 Pa. Copyright: 2015, The Japan Society of Applied Physics.

1×10^{-5} Pa[118]. The higher dissociative adsorption probability of O_2 on Ru than Cu[158] is consistent with the values of the shrinkage rates. For the direct reaction of O_2 and graphene, on the other hand, the values of approximately 20 μm/min were reported even under the inert condition such as substrate temperature and O_2 partial pressure of 550 °C and 1 $\times10^{-4}$ Pa, respectively[88, 118, 119]. Judging from the values, I conclude that the shrinkage of graphene is ascribed to the depletion of the precursors from the surface by O_2.

The O_2 partial pressure should be optimized to grow the high quality graphene for the device application. The dendritic shape of graphene is not feasible for that purpose. The surface O atoms deplete the growth precursors to suppress the nucleation of graphene, while the precursor density is also affected by the CH_4 flow rate. Therefore, the O_2 partial pressure should be optimized as high as possible before the optimization of the CH_4 flow rate, in which the dendritic growth does not occur.

3 Discussion of Growth Mechanism

In this section, I discuss the mechanism of the nucleation, growth, and shrinkage of graphene during CVD based on the analysis and discussion in the previous section. I propose a possible way to optimize the growth parameters of graphene by CVD according to the discussion of the mechanism.

3.1 Model of Chemical Vapor Deposition of Graphene

Figure IV. 3. 1 shows the schematic illustration of the growth and shrinkage mechanism of graphene during CVD. The growth of graphene requires the production of growth precursors from the adsorption and decomposition of the C source gas. The precursors start to nucleate and is incorporated into graphene lattice on the Cu substrates. During the shrinkage of graphene, on the other hand, the precursors disappear from the Cu substrates. I discuss the elementary steps of these chemical reactions, in the following focusing on the production of precursors, lateral growth of graphene, and shrinkage of graphene.

First, the CH_4 gas in the vapor phase adsorbs onto the Cu substrates to produce the growth precursors of graphene. Owing to the negligible dissociative adsorption probability of CH_4 on

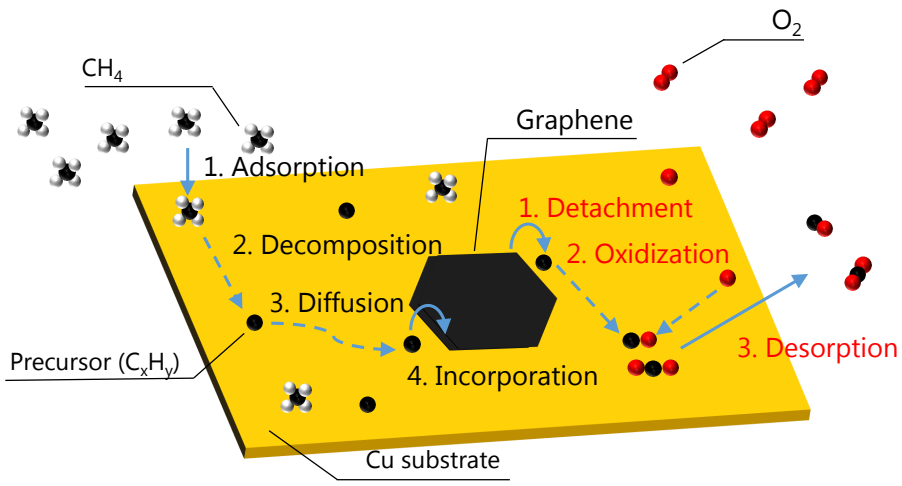

Figure IV. 3. 1 Schematic illustration for CVD growth and shrinkage of graphene by CH_4 and O_2. The adsorption, decomposition, diffusion, and the incorporation mechanism are known to relate to CH_4, as shown in Fig. I. 1. 5. Oxygen adsorbs onto Cu, reacts with the precursors detached from graphene lattice, and desorbs from the surface presumably due to the formation of volatile CO and CO_2 molecules. Moreover, O atoms enhances the detachment of H from graphene edge to decrease the incorporation energy of the precursors into the graphene lattice.

the bare Cu surface[152], the pre-adsorbed O_2 atoms play a important role in the precursor production[114]. Analysis of the flow rate dependence in section IV. 2.3 suggests that the growth rate of graphene increases as the production of growth precursors is enhanced. On the other hand, adsorbed O_2 atoms consume the growth precursors. It is considered that the C and O atoms react to produce volatile CO and CO_2 atoms, resulting in the decrease in the precursor density. Therefore, the competition of the production from CH_4 and the consumption by O_2 determines the density of the growth precursors.

The produced precursors diffuse on the Cu surfaces and is incorporated into graphene lattice. The analysis of the lateral growth of graphene shows that the rate-limiting step of the graphene growth is the incorporation of the growth precursors to the graphene lattice. The activation energy of the incorporation, however, can be reduced by the increase in the surface O atoms on the Cu substrates. The O atoms enhance the detachment of H atoms from graphene edges to reduce the incorporation energy less than the diffusion energy of the precursors as shown in section IV. 2.4, which is consistent with the previous report[81]. In this case, the dendritic growth of graphene is observed due to the diffusion limited growth.

When the supply of CH_4 is shut-off, the graphene starts the shrinkage in the present study. Actually, the detachment of the precursors can occur during the growth of graphene as suggested in section IV. 2.3. The shrinkage rate increases with the O_2 partial pressure. The surface O_2 atoms do not react with graphene lattice directly but with the growth precursors to be eliminated from the surfaces presumably due to the formation of volatile CO and CO_2 molecules. The consumption of the precursors thus reduces the attachment of the growth precursors resulting in the shrinkage of graphene.

3.2 Possible Way to Optimize Growth Parameters

I also suggest a possible way to optimize the growth parameters such as T_s, CH_4 flow rate, and O_2 partial pressure. The growth of the large area single crystal graphene requires the decrease in the n_{sat}. As discussed in section IV. 2.2, T_s should be optimized taking the competition of the growth rate and nucleation rate into account. The dendritic graphene grains are unsuitable for the device application, and thus the O_2 partial pressure should be optimized to avoid such the growth. The precursor density, dominated by both CH_4 flow rate and O_2 partial pressure, should be reduced as possible to suppress the nucleation, as discussed in section IV. 2.3. After that, the CH_4 flow rate should be optimized to suppress as possible to cause the nucleation of graphene. The real-time RM can contribute to the efficient optimization of such the growth parameters owing to the fast and non-destructive observations,

Part V
Concluding Remarks

In this dissertation, I develop radiation microscopy (RM) and discuss the growth mechanism of graphene in CVD by the analysis of the real-time observation.

Radiation microscopy enables us to observe the difference in thermal radiation depending on the emissivity of the materials. Planck's law and the gray body model explain the radiation of the wavelength in visible and near-infrared region. The low temperature limit of the observation in the present study is 700 °C, which is determined by the intensities of the radiation and a stray light. The comparison with the previous method clarifies the layer-by-layer observation and the in-plane resolution of 1800 nm in RM. While the spatial resolution is not enough to discuss the initial stage of nucleation, the real-time observation of μm sized graphene grains is presumably useful for the industrial fabrication of graphene. The growth of the 2nd layer of graphene starts below the 1st layer of graphene and on the Cu substrate, which is affected by the lattice symmetry of 1st layer of graphene.

I extracted the absolute values of several important physical parameters from the RM images developed in this dissertation. The saturation nucleation density, growth rate, and shrinkage rate are discussed based on their dependence on the growth parameters. These chemical reactions are accelerated at high temperatures. The rate-limiting steps of the growth and shrinkage of graphene are determined to the attachment and detachment of growth precursors at the graphene edges. Judging from the analysis of supply of CH_4 and O_2 gases, these gases produces and consumes the growth precursors, respectively. While the precursors attach and detach on the graphene edges during the growth, the shift of the density of the growth precursors determines whether graphene grows or shrinks. Surface O atoms also determine the shape of graphene from compact to dendritic with the O_2 partial pressure increasing. I also discuss the optimized conditions such as the substrate temperature, CH_4 flow rate, and O_2 partial pressure to decrease the nucleation density and to avoid the dendritic growth.

There is still a room to be investigated by the real-time observation of RM in future. Although the method is considered applicable to other film-substrate combination, it has not

been proved in the present study. The orientation of the 2nd layer of graphene on the 1st layer can be understood and controlled further by using the real-time RM observation. The relatively close activation energies of the growth and shrinkage are related to the elementary steps including the structure of the growth precursors. Whether the activation energy depends on the O_2 partial pressure is not clarified. Moreover, the optimization of the growth parameters is insufficient toward the wafer-scale single-crystal graphene. The mechanism of the CVD growth of graphene can be revealed by the present method. Furthermore, the real-time RM observation is expected to reveal the crystal growth under the high temperature and pressure conditions.

References

[1] Novoselov, K. S. *et al.* Electric field effect in atomically thin carbon films. *Science* **306**, 666–9 (2004).

[2] Geim, A. K. & Grigorieva, I. V. Van der Waals heterostructures. *Nature* **499**, 419–25 (2013).

[3] Chhowalla, M. *et al.* The chemistry of two-dimensional layered transition metal dichalcogenide nanosheets. *Nature chemistry* **5**, 263–75 (2013).

[4] Butler, S. Z. *et al.* Progress, challenges, and opportunities in two-dimensional materials beyond graphene. *ACS nano* **7**, 2898–926 (2013).

[5] Castro Neto, A. H., Guinea, F., Peres, N. M. R., Novoselov, K. S. & Geim, A. K. The electronic properties of graphene. *Reviews of Modern Physics* **81**, 109–162 (2009).

[6] Polini, M., Guinea, F., Lewenstein, M., Manoharan, H. C. & Pellegrini, V. Artificial honeycomb lattices for electrons, atoms and photons. *Nature nanotechnology* **8**, 625–33 (2013).

[7] Zeng, H., Dai, J., Yao, W., Xiao, D. & Cui, X. Valley polarization in MoS2 monolayers by optical pumping. *Nature nanotechnology* **7**, 490–3 (2012).

[8] Gorbachev, R. V. *et al.* Detecting topological currents in graphene superlattices. *Science* **346**, 1–16 (2014).

[9] Geim, A. K. & Novoselov, K. S. The rise of graphene. *Nature materials* **6**, 183–91 (2007).

[10] Chen, J.-H., Jang, C., Xiao, S., Ishigami, M. & Fuhrer, M. S. Intrinsic and extrinsic performance limits of graphene devices on SiO2. *Nature nanotechnology* **3**, 206–9 (2008).

[11] Guimarães, M. H. D. *et al.* Spin transport in high-quality suspended graphene devices. *Nano letters* **12**, 3512–7 (2012).

[12] Petrone, N. *et al.* Chemical vapor deposition-derived graphene with electrical performance of exfoliated graphene. *Nano letters* **12**, 2751–6 (2012).

[13] Wang, L., Meric, I., Huang, P., Gao, Q. & Gao, Y. One-dimensional electrical contact

to a two-dimensional material. *Science* **342**, 614–618 (2013).

[14] Balandin, A. A. *et al.* Superior thermal conductivity of single-layer graphene. *Nano letters* **8**, 902–7 (2008).

[15] Mak, K. F. *et al.* Measurement of the Optical Conductivity of Graphene. *Physical Review Letters* **101**, 196405 (2008).

[16] Nair, R. R. *et al.* Fine structure constant defines visual transparency of graphene. *Science* **320**, 1308 (2008).

[17] Novoselov, K. S. *et al.* Two-dimensional gas of massless Dirac fermions in graphene. *Nature* **438**, 197–200 (2005).

[18] Zhang, Y., Tan, Y.-W., Stormer, H. L. & Kim, P. Experimental observation of the quantum Hall effect and Berry's phase in graphene. *Nature* **438**, 201–4 (2005).

[19] Novoselov, K. S. *et al.* Room-temperature quantum Hall effect in graphene. *Science* **315**, 1379 (2007).

[20] Lee, C., Wei, X., Kysar, J. W. J. J. W. & Hone, J. Measurement of the elastic properties and intrinsic strength of monolayer graphene. *Science (New York, N.Y.)* **321**, 385–8 (2008).

[21] Barone, V., Hod, O. & Scuseria, G. E. Electronic structure and stability of semiconducting graphene nanoribbons. *Nano Letters* **6**, 2748–2754 (2006).

[22] Han, M. Y., Özyilmaz, B., Zhang, Y. & Kim, P. Energy band-gap engineering of graphene nanoribbons. *Physical Review Letters* **98**, 1–4 (2007).

[23] Li, X., Wang, X., Zhang, L., Lee, S. & Dai, H. Chemically derived, ultrasmooth graphene nanoribbon semiconductors. *Science (New York, N.Y.)* **319**, 1229–32 (2008).

[24] Kosynkin, D. V. *et al.* Longitudinal unzipping of carbon nanotubes to form graphene nanoribbons. *Nature* **458**, 872–876 (2009).

[25] Jiao, L., Zhang, L., Wang, X., Diankov, G. & Dai, H. Narrow graphene nanoribbons from carbon nanotubes. *Nature* **458**, 877–80 (2009).

[26] Jiao, L., Wang, X., Diankov, G., Wang, H. & Dai, H. Facile synthesis of high-quality graphene nanoribbons. *Nature nanotechnology* **5**, 321–5 (2010).

[27] Schwierz, F. Graphene transistors. *Nature nanotechnology* **5**, 487–96 (2010).

[28] Yoo, E. *et al.* Large reversible Li storage of graphene nanosheet families for use in rechargeable lithium ion batteries. *Nano letters* **8**, 2277–82 (2008).

[29] Xu, C. *et al.* Graphene-based electrodes for electrochemical energy storage. *Energy & Environmental Science* **6**, 1388 (2013).

[30] Schedin, F. *et al.* Detection of individual gas molecules adsorbed on graphene. *Nature materials* **6**, 652–5 (2007).

[31] Wu, S., He, Q., Tan, C., Wang, Y. & Zhang, H. Graphene-based electrochemical sensors. *Small* **9**, 1160–72 (2013).

[32] Chen, D., Zhang, H., Liu, Y. & Li, J. Graphene and its derivatives for the development of solar cells, photoelectrochemical, and photocatalytic applications. *Energy & Environmental Science* **6**, 1362 (2013).

[33] Novoselov, K. S. *et al.* Unconventional quantum Hall effect and Berry's phase of 2π in bilayer graphene. *Nature Physics* **2**, 177–180 (2006).

[34] Zomer, P. J., Dash, S. P., Tombros, N. & van Wees, B. J. A transfer technique for high mobility graphene devices on commercially available hexagonal boron nitride. *Applied Physics Letters* **99**, 232104 (2011).

[35] Wallace, P. The Band Theory of Graphite. *Physical Review* **71**, 622–634 (1947).

[36] Ferrari, A. C. Raman spectroscopy of graphene and graphite: Disorder, electron-phonon coupling, doping and nonadiabatic effects. *Solid State Communications* **143**, 47–57 (2007).

[37] Malard, L., Pimenta, M., Dresselhaus, G. & Dresselhaus, M. Raman spectroscopy in graphene. *Physics Reports* **473**, 51–87 (2009).

[38] Ferrari, A. C. & Basko, D. M. Raman spectroscopy as a versatile tool for studying the properties of graphene. *Nature nanotechnology* **8**, 235–46 (2013).

[39] Fujii, S. & Enoki, T. Cutting of oxidized graphene into nanosized pieces. *Journal of the American Chemical Society* **132**, 10034–41 (2010).

[40] Wang, X. & Dai, H. Etching and narrowing of graphene from the edges. *Nature chemistry* **2**, 661–5 (2010).

[41] Xie, L., Jiao, L. & Dai, H. Selective etching of graphene edges by hydrogen plasma.

Journal of the American Chemical Society **132**, 14751–3 (2010).

[42] Zhang, Y., Li, Z., Kim, P., Zhang, L. & Zhou, C. Anisotropic hydrogen etching of chemical vapor deposited graphene. *ACS nano* **6**, 126–32 (2012).

[43] Geng, D. *et al.* Fractal etching of graphene. *Journal of the American Chemical Society* **135**, 6431–4 (2013).

[44] Balooch, M., Cardillo, M., Miller, D. & Stickney, R. Molecular beam study of the apparent activation barrier associated with adsorption and desorption of hydrogen on copper. *Surface Science* **46**, 358–392 (1974).

[45] Choubak, S., Biron, M., Levesque, P. L., Martel, R. & Desjardins, P. No Graphene Etching in Purified Hydrogen. *The Journal of Physical Chemistry Letters* **4**, 1100–1103 (2013).

[46] Jr, W. H. & Offeman, R. Preparation of graphitic oxide. *Journal of the American Chemical Society* **208**, 1937–1937 (1958).

[47] Stankovich, S. *et al.* Stable aqueous dispersions of graphitic nanoplatelets via the reduction of exfoliated graphite oxide in the presence of poly(sodium 4-styrenesulfonate). *Journal of Materials Chemistry* **16**, 155 (2006).

[48] Stankovich, S. *et al.* Synthesis of graphene-based nanosheets via chemical reduction of exfoliated graphite oxide. *Carbon* **45**, 1558–1565 (2007).

[49] Obata, S., Tanaka, H. & Saiki, K. Reduction of a Single Layer Graphene Oxide Film on Pt(111). *Applied Physics Express* **4**, 025102 (2011).

[50] Tanaka, H., Obata, S. & Saiki, K. Reduction of graphene oxide at the interface between a Ni layer and a SiO2 substrate. *Carbon* **59**, 472–478 (2013).

[51] Berger, C. *et al.* Ultrathin Epitaxial Graphite: 2D Electron Gas Properties and a Route toward Graphene-based Nanoelectronics. *The Journal of Physical Chemistry B* **108**, 19912–19916 (2004).

[52] Berger, C. *et al.* Electronic confinement and coherence in patterned epitaxial graphene. *Science* **312**, 1191–6 (2006).

[53] Wu, Y. Q. *et al.* Top-gated graphene field-effect-transistors formed by decomposition of SiC. *Applied Physics Letters* **92**, 092102 (2008).

[54] Hibino, H. *et al.* Microscopic thickness determination of thin graphite films formed on SiC from quantized oscillation in reflectivity of low-energy electrons. *Physical Review B* **77**, 075413 (2008).

[55] Emtsev, K. V. *et al.* Towards wafer-size graphene layers by atmospheric pressure graphitization of silicon carbide. *Nature materials* **8**, 203–7 (2009).

[56] Hwang, J., Kim, M., Campbell, D. & Alsalman, H. van der Waals Epitaxial growth of graphene on sapphire by chemical vapor deposition without a metal catalyst. *ACS nano* **7**, 385–395 (2012).

[57] Sun, J. *et al.* Direct growth of high-quality graphene on high-κ dielectric SrTiO3 substrates. *Journal of the American Chemical Society* **136**, 6574–7 (2014).

[58] Li, X. *et al.* Large-area synthesis of high-quality and uniform graphene films on copper foils. *Science* **324**, 1312–4 (2009).

[59] Li, X., Cai, W., Colombo, L. & Ruoff, R. S. Evolution of graphene growth on Ni and Cu by carbon isotope labeling. *Nano letters* **9**, 4268–72 (2009).

[60] Bae, S. *et al.* Roll-to-roll production of 30-inch graphene films for transparent electrodes. *Nature Nanotechnology* **5**, 574–578 (2010).

[61] Li, X. *et al.* Transfer of large-area graphene films for high-performance transparent conductive electrodes. *Nano letters* **9**, 4359–63 (2009).

[62] Kim, K. S. *et al.* Large-scale pattern growth of graphene films for stretchable transparent electrodes. *Nature* **457**, 706–10 (2009).

[63] Reina, A. *et al.* Large area, few-layer graphene films on arbitrary substrates by chemical vapor deposition. *Nano letters* **9**, 30–5 (2009).

[64] Cai, J. *et al.* Atomically precise bottom-up fabrication of graphene nanoribbons. *Nature* **466**, 470–3 (2010).

[65] Treier, M. *et al.* Surface-assisted cyclodehydrogenation provides a synthetic route towards easily processable and chemically tailored nanographenes. *Nature chemistry* **3**, 61–7 (2011).

[66] Han, P. *et al.* Bottom-Up Graphene-Nanoribbon Fabrication Reveals Chiral Edges and Enantioselectivity. *ACS nano* **8**, 9181–9187 (2014).

[67] Chen, Y.-C. *et al.* Molecular bandgap engineering of bottom-up synthesized graphene nanoribbon heterojunctions. *Nature nanotechnology* 1–5 (2015).

[68] Sun, Z. *et al.* Growth of graphene from solid carbon sources. *Nature* **468**, 549–52 (2010).

[69] Ruan, G., Sun, Z., Peng, Z. & Tour, J. M. Growth of graphene from food, insects, and waste. *ACS nano* **5**, 7601–7 (2011).

[70] Liu, Z., Pandey, D., Wei, D., Chung, T. F. & Peng, P. Control and characterization of individual grains and grain boundaries in graphene grown by chemical vapour deposition. *Nature Materials* **10**, 443–449 (2011).

[71] Orofeo, C. M. *et al.* Influence of Cu metal on the domain structure and carrier mobility in single-layer graphene. *Carbon* **50**, 2189–2196 (2012).

[72] Clark, K. W. *et al.* Spatially Resolved Mapping of Electrical Conductivity across Individual Domain (Grain) Boundaries in Graphene. *ACS nano* **7**, 7956–7966 (2013).

[73] Li, X. *et al.* Large-area graphene single crystals grown by low-pressure chemical vapor deposition of methane on copper. *Journal of the American Chemical Society* **133**, 2816–9 (2011).

[74] Vlassiouk, I. *et al.* Role of hydrogen in chemical vapor deposition growth of large single-crystal graphene. *ACS nano* **5**, 6069–76 (2011).

[75] Yan, Z. *et al.* Toward the Synthesis of Wafer-Scale Single-Crystal Graphene on Copper Foils. *ACS Nano* **6**, 9110–9117 (2012).

[76] Kim, H. *et al.* Activation energy paths for graphene nucleation and growth on Cu. *ACS nano* **6**, 3614–23 (2012).

[77] Vlassiouk, I. *et al.* Graphene Nucleation Density on Copper: Fundamental Role of Background Pressure. *The Journal of Physical Chemistry C* **117**, 18919–18926 (2013).

[78] Celebi, K. *et al.* Evolutionary kinetics of graphene formation on copper. *Nano letters* **13**, 967–74 (2013).

[79] Gan, L. & Luo, Z. Turning off hydrogen to realize seeded growth of subcentimeter single-crystal graphene grains on copper. *ACS nano* **7**, 9480–8 (2013).

[80] Mohsin, A. *et al.* Synthesis of millimeter-size hexagon-shaped graphene single crystals

on resolidified copper. *ACS nano* **7**, 8924–31 (2013).

[81] Hao, Y. *et al.* The role of surface oxygen in the growth of large single-crystal graphene on copper. *Science* **342**, 720–3 (2013).

[82] Wu, B. *et al.* Self-organized graphene crystal patterns. *NPG Asia Materials* **5**, e36 (2013).

[83] Eres, G. *et al.* Cooperative island growth of large-area single-crystal graphene on copper using chemical vapor deposition. *ACS nano* **8**, 5657–69 (2014).

[84] Ma, T. *et al.* Repeated Growth-Etching-Regrowth for Large-Area Defect-Free Single-Crystal Graphene by Chemical Vapor Deposition. *ACS nano* **8**, 12806–12813 (2014).

[85] Shelton, J., Patil, H. & Blakely, J. Equilibrium segregation of carbon to a nickel (111) surface: A surface phase transition. *Surface Science* **43**, 493–520 (1974).

[86] Loginova, E., Bartelt, N. C., Feibelman, P. J. & McCarty, K. F. Evidence for graphene growth by C cluster attachment. *New Journal of Physics* **10**, 093026 (2008).

[87] Sutter, P. W., Flege, J.-I. & Sutter, E. A. Epitaxial graphene on ruthenium. *Nature materials* **7**, 406–11 (2008).

[88] Cui, Y., Fu, Q., Zhang, H., Tan, D. & Bao, X. Dynamic Characterization of Graphene Growth and Etching by Oxygen on Ru(0001) by Photoemission Electron Microscopy. *The Journal of Physical Chemistry C* **113**, 20365–20370 (2009).

[89] Puretzky, A. A. *et al.* Real-time optical diagnostics of graphene growth induced by pulsed chemical vapor deposition. *Nanoscale* **5**, 6507–17 (2013).

[90] Dong, G. & Frenken, J. W. M. Kinetics of graphene formation on Rh(111) investigated by in situ scanning tunneling microscopy. *ACS nano* **7**, 7028–33 (2013).

[91] Patera, L. L. *et al.* In Situ Observations of the Atomistic Mechanisms of Ni Catalyzed Low Temperature Graphene Growth. *ACS nano* **7**, 7901–12 (2013).

[92] Liu, Z. *et al.* In situ observation of step-edge in-plane growth of graphene in a STEM. *Nature communications* **5**, 4055 (2014).

[93] Yu, Q. *et al.* Graphene segregated on Ni surfaces and transferred to insulators. *Applied Physics Letters* **93**, 113103 (2008).

[94] Rosei, R. *et al.* Structure of graphitic carbon on Ni(111): A surface extended-energy-

loss fine-structure study. *Physical Review B* **28**, 1161–1164 (1983).

[95] Vázquez de Parga, A. *et al.* Periodically Rippled Graphene: Growth and Spatially Resolved Electronic Structure. *Physical Review Letters* **100**, 056807 (2008).

[96] Kwon, S.-Y. *et al.* Growth of semiconducting graphene on palladium. *Nano letters* **9**, 3985–90 (2009).

[97] Eom, D. *et al.* Structure and electronic properties of graphene nanoislands on Co(0001). *Nano letters* **9**, 2844–8 (2009).

[98] Ago, H. *et al.* Epitaxial chemical vapor deposition growth of single-layer graphene over cobalt film crystallized on sapphire. *ACS nano* **4**, 7407–14 (2010).

[99] Sicot, M. *et al.* Nucleation and growth of nickel nanoclusters on graphene Moire on Rh(111). *Applied Physics Letters* **96**, 093115 (2010).

[100] Kondo, D. *et al.* Low-Temperature Synthesis of Graphene and Fabrication of Top-Gated Field Effect Transistors without Using Transfer Processes. *Applied Physics Express* **3**, 025102 (2010).

[101] McLellan, R. B. The solubility of carbon in solid gold, copper, and silver. *Scripta Metallurgica* **3**, 389–391 (1969).

[102] López, G. & Mittemeijer, E. The solubility of C in solid Cu. *Scripta Materialia* **51**, 1–5 (2004).

[103] Lee, J.-H. *et al.* Wafer-scale growth of single-crystal monolayer graphene on reusable hydrogen-terminated germanium. *Science* **344**, 286–9 (2014).

[104] Oznuluer, T. *et al.* Synthesis of graphene on gold. *Applied Physics Letters* **98**, 183101 (2011).

[105] Land, T., Michely, T., Behm, R., Hemminger, J. & Comsa, G. STM investigation of single layer graphite structures produced on Pt(111) by hydrocarbon decomposition. *Surface Science* **264**, 261–270 (1992).

[106] N'Diaye, A. T., Coraux, J., Plasa, T. N., Busse, C. & Michely, T. Structure of epitaxial graphene on Ir(111). *New Journal of Physics* **10**, 043033 (2008).

[107] Coraux, J., N'Diaye, A. T., Busse, C. & Michely, T. Structural coherency of graphene on Ir(111). *Nano letters* **8**, 565–70 (2008).

[108] Vo-Van, C. *et al.* Epitaxial graphene prepared by chemical vapor deposition on single crystal thin iridium films on sapphire. *Applied Physics Letters* **98**, 181903 (2011).

[109] Yu, H. K. *et al.* Chemical Vapor Deposition of Graphene on a ”Peeled-Off” Epitaxial Cu(111) Foil: A Simple Approach to Improved Properties. *ACS nano* **8**, 8636–8643 (2014).

[110] Qi, M. *et al.* Hydrogen Kinetics on Scalable Graphene Growth by Atmospheric Pressure Chemical Vapor Deposition with Acetylene. *The Journal of Physical Chemistry C* **117**, 14348–14353 (2013).

[111] Zhao, P. *et al.* Self-Limiting Chemical Vapor Deposition Growth of Monolayer Graphene from Ethanol. *The Journal of Physical Chemistry C* **117**, 10755–10763 (2013).

[112] Kidambi, P. R. *et al.* Observing graphene grow: catalyst-graphene interactions during scalable graphene growth on polycrystalline copper. *Nano letters* **13**, 4769–78 (2013).

[113] Chen, H., Zhu, W. & Zhang, Z. Contrasting Behavior of Carbon Nucleation in the Initial Stages of Graphene Epitaxial Growth on Stepped Metal Surfaces. *Physical Review Letters* **104**, 186101 (2010).

[114] Alstrup, I., Chorkendorff, I. & Ullmann, S. The interaction of CH4 at high temperatures with clean and oxygen precovered Cu(100). *Surface Science* **264**, 95–102 (1992).

[115] Zhang, W., Wu, P., Li, Z. & Yang, J. First-Principles Thermodynamics of Graphene Growth on Cu Surfaces. *The Journal of Physical Chemistry C* **115**, 17782–17787 (2011).

[116] Choubak, S. *et al.* Graphene CVD: Interplay Between Growth and Etching on Morphology and Stacking by Hydrogen and Oxidizing Impurities. *The Journal of Physical Chemistry C* **118**, 21532–21540 (2014).

[117] Gottardi, S. *et al.* Comparing graphene growth on Cu(111) vs. oxidized Cu(111). *Nano letters* (2015).

[118] Starodub, E., Bartelt, N. C. & McCarty, K. F. Oxidation of Graphene on Metals. *The Journal of Physical Chemistry C* **114**, 5134–5140 (2010).

[119] Sutter, P., Sadowski, J. & Sutter, E. Chemistry under cover: tuning metal-graphene

interaction by reactive intercalation. *Journal of the American Chemical Society* **11973**, 8175–8179 (2010). arXiv:arXiv:1001.4837v2.

[120] Nie, S., Wofford, J. M., Bartelt, N. C., Dubon, O. D. & McCarty, K. F. Origin of the mosaicity in graphene grown on Cu(111). *Physical Review B* **84**, 155425 (2011).

[121] Wofford, J. M., Nie, S., McCarty, K. F., Bartelt, N. C. & Dubon, O. D. Graphene Islands on Cu foils: the interplay between shape, orientation, and defects. *Nano letters* **10**, 4890–6 (2010).

[122] Wang, Z.-J. *et al.* Direct Observation of Graphene Growth and Associated Copper Substrate Dynamics by in Situ Scanning Electron Microscopy. *ACS nano* (2015).

[123] Losurdo, M., Giangregorio, M. M. M., Capezzuto, P. & Bruno, G. Graphene CVD growth on copper and nickel: role of hydrogen in kinetics and structure. *Physical chemistry chemical physics* **13**, 20836–43 (2011).

[124] Cançado, L., Pimenta, M., Neves, B., Dantas, M. & Jorio, A. Influence of the Atomic Structure on the Raman Spectra of Graphite Edges. *Physical Review Letters* **93**, 247401 (2004).

[125] Pisana, S. *et al.* Breakdown of the adiabatic Born-Oppenheimer approximation in graphene. *Nature materials* **6**, 198–201 (2007).

[126] Das, a. *et al.* Monitoring dopants by Raman scattering in an electrochemically top-gated graphene transistor. *Nature nanotechnology* **3**, 210–5 (2008).

[127] Lu, C. *et al.* Twisting bilayer graphene superlattices. *ACS nano* **7**, 2587–2594 (2013).

[128] Zhao, H., Lin, Y., Yeh, C.-h., Tian, H. & Chen, Y. Growth and Raman Spectra of Single-Crystal Trilayer Graphene with Different Stacking Orientations. *ACS nano* **8**, 10766–10773 (2014).

[129] Kretinin, A. V. *et al.* Electronic properties of graphene encapsulated with different two-dimensional atomic crystals. *Nano letters* **14**, 3270–6 (2014).

[130] Planck, M. On the Law of Distribution of Energy in the Normal Spectrum On the Law of Distribution of Energy in the Normal Spectrum. *Annalen der Physik* **4**, 553 (1901).

[131] Freitag, M., Chiu, H.-Y., Steiner, M., Perebeinos, V. & Avouris, P. Thermal infrared emission from biased graphene. *Nature nanotechnology* **5**, 497–501 (2010).

[132] Taft, E. & Philipp, H. Optical properties of graphite. *Physical Review* **138**, A197–A202 (1965).

[133] Mizuno, K. *et al.* A black body absorber from vertically aligned single-walled carbon nanotubes. *Proceedings of the National Academy of Sciences of the United States of America* **106**, 6044–7 (2009).

[134] Ramanathan, K. G. & Yen, S. H. High-temperature emissivities of copper, aluminum, and silver. *Journal of the Optical Society of America* **67**, 32 (1977).

[135] Kato, S. *In-situ observation of growth of graphene using optical microscopy*. Master's thesis, The University of Tokyo (2014).

[136] McClure, J. L. J. L., Cezairliyan, A. & Kaschnitz, E. Radiance Temperatures (in the Wavelength Range 527 to 1500 nm) of Palladium and Platinum at Their Melting Points by a Pulse-Heating Technique. *International Journal of Thermophysics* **20**, 1149–1161 (1999).

[137] Cagran, C. & Pottlacher, G. Thermophysical Properties of Palladium. *Platinum Metals Review* **50**, 144–149 (2006).

[138] Hamamatsu Photonics. Web Page for Digital camera ORCA-Flash4.0 V2 C11440-22CU. URL: http://www.hamamatsu.com/jp/en/product/category/5000/5005/C11440-22CU/index.html. Accessed: 2015/02/09 13:42+0900 (JST).

[139] Chae, D.-H., Krauss, B., von Klitzing, K. & Smet, J. H. Hot phonons in an electrically biased graphene constriction. *Nano letters* **10**, 466–71 (2010).

[140] Teyssieux, D., Thiery, L. & Cretin, B. Near-infrared thermography using a charge-coupled device camera: application to microsystems. *The Review of Scientific Instruments* **78**, 034902 (2007).

[141] Vellvehi, M., Perpiñà, X., Lauro, G. L., Perillo, F. & Jordà, X. Irradiance-based emissivity correction in infrared thermography for electronic applications. *The Review of Scientific Instruments* **82**, 114901 (2011).

[142] Le Rouzic, J. & Reddyhoff, T. Development of Infrared Microscopy for Measuring Asperity Contact Temperatures. *Journal of Tribology* **135**, 021504 (2013).

[143] Schneider, C. A., Rasband, W. S. & Eliceiri, K. W. NIH Image to ImageJ: 25 years of

image analysis. *Nature Methods* **9**, 671–675 (2012).

[144] Ismach, A. *et al.* Direct Chemical Vapor Deposition of Graphene on Dielectric Surfaces. *Nano letters* **10**, 1542–1548 (2010).

[145] Jacobberger, R. M. & Arnold, M. S. Graphene Growth Dynamics on Epitaxial Copper Thin Films. *Chemistry of Materials* **25**, 871–877 (2013).

[146] Lewis, A. M., Derby, B. & Kinloch, I. A. Influence of gas phase equilibria on the chemical vapor deposition of graphene. *ACS nano* **7**, 3104–17 (2013).

[147] Hakkinen, H. & Manninen, M. Computer simulation of disordering and premelting of low-index faces of copper. *Physical Review B* **46**, 1725–1743 (1992).

[148] Daff, T. D., Saadoune, I., Lisiecki, I. & de Leeuw, N. H. Computer simulations of the effect of atomic structure and coordination on the stabilities and melting behaviour of copper surfaces and nano-particles. *Surface Science* **603**, 445–454 (2009).

[149] Li, Q. *et al.* Growth of adlayer graphene on Cu studied by carbon isotope labeling. *Nano letters* **13**, 486–90 (2013).

[150] Fang, W. *et al.* Asymmetric growth of bilayer graphene on copper enclosures using low-pressure chemical vapor deposition. *ACS nano* **8**, 6491–9 (2014).

[151] Zhao, P. *et al.* Equilibrium chemical vapor deposition growth of bernal-stacked bilayer graphene. *ACS nano* **8**, 11631–8 (2014).

[152] Balooch, M. & Olander, D. R. Reactions of modulated molecular beams with pyrolytic graphite. III. Hydrogen. *The Journal of Chemical Physics* **63**, 4772 (1975).

[153] Terasawa, T.-o. & Saiki, K. Growth of graphene on Cu by plasma enhanced chemical vapor deposition. *Carbon* **50**, 869–874 (2012).

[154] Gajewski, G. & Pao, C.-W. Ab initio calculations of the reaction pathways for methane decomposition over the Cu (111) surface. *The Journal of Chemical Physics* **135**, 064707 (2011).

[155] Hayashi, Y., Drawl, W. & Messier, R. Temperature Dependence of Nucleation Density of Chemical Vapor Deposition Diamond. *Japanese Journal of Applied Physics* **31**, L193–L196 (1992).

[156] Hayashi, K., Sato, S., Ikeda, M., Kaneta, C. & Yokoyama, N. Selective graphene

formation on copper twin crystals. *Journal of the American Chemical Society* **134**, 12492–8 (2012).

[157] Terasawa, T.-o. & Saiki, K. Effect of vapor-phase oxygen on chemical vapor deposition growth of graphene. *Applied Physics Express* **8**, 035101 (2015).

[158] Wheeler, M. C., Seets, D. C. & Mullins, C. B. Kinetics and dynamics of the initial dissociative chemisorption of oxygen on Ru(001). *The Journal of Chemical Physics* **105**, 1572 (1996).

Acknowledgment

I would like to thank to all those who supported me for this dissertation in any respect.

I am really grateful to Professor Koichiro Saiki, my supervisor. From the entrance to his laboratory to now, he has always given me a tremendous support to publish articles and finish the dissertation even at 31st December! Without his warm support the present dissertation could not be completed.

I sincerely appreciate Professor Takehiko Sasaki. I was always encouraged in weekly seminars by his insightful comment based on the vast knowledge of the surface science.

I heartily thank Ms. Miho Orihara who is a secretary of the laboratory. Her kind supports help me in many situations of the laboratory life.

I want to express my special gratitude to Dr. Seiji Obata and Dr. Gaku Imamura for their sense of wonder and humor in the laboratory and daily life. Their attitudes to deal with problems have been the special examples as young and promising scientists during our collaboration of five years.

I am delighted to all the members and ex-members in Saiki laboratory who worked with me. Particularly I want to show acknowledge to Mr. Kodai Hayashi and Mr. Sho Kato for our subterranean lives to develop the optical microscopy from the outside of chamber.

I should be thankful to Japan Society for the Promising of Science for financial support, JSPS DC2, to survive my last 2 years of the doctoral course. The present research was also supported by Grant-in-Aid for JSPS Fellows.

My deepest appreciation goes to my family, father, mother, and brother, for their financial and moral supports.